

**PROPERTIES OF HIGHLY DISPERSED COBALT
ON ZEOLITES AND MANGANESE ON
MAGNESIUM OXIDE**

Supattra Khabuanchalad



**A Thesis Submitted in Partial Fulfillment of the Requirements for the
Degree of Doctor of Philosophy in Chemistry
Suranaree University of Technology
Academic Year 2011**

สมบัติของโพลีเมอร์ชนิดไฮโดรเจลและเมมเบรนเมกนีเซียมออกไซด์
ที่กระจายตัวสูง



นางสาวสุภัทรา ขบวนฉลาด

วิทยานิพนธ์นี้เป็นส่วนหนึ่งของการศึกษาตามหลักสูตรปริญญาวิทยาศาสตรดุษฎีบัณฑิต

สาขาวิชาเคมี

มหาวิทยาลัยเทคโนโลยีสุรนารี

ปีการศึกษา 2554

**PROPERTIES OF HIGHLY DISPERSED COBALT
ON ZEOLITES AND MANGANESE
ON MAGNESIUM OXIDE**

Suranaree University of Technology has approved this thesis submitted in partial fulfillment of the requirements for the Degree of Doctor of Philosophy.

Thesis Examining Committee

(Asst. Prof. Dr. Kunwadee Rangriwatananon)

Chairperson

(Assoc. Prof. Dr. Jatuporn Wittayakun)

Member (Thesis Advisor)

(Prof. Dr. Bruce C. Gates)

Member

(Asst. Prof. Dr. Sanchai Prayoonpokarach)

Member

(Dr. Saowapa Chotisuwan)

Member

(Prof. Dr. Sukit Limpijumnong)

Vice Rector for Academic Affairs

(Assoc. Prof. Dr. Prapun Manyum)

Dean of Institute of Science

สุภัทรา ขบวนการ : สมบัติของโคบอลต์บนซีโอไลต์และแมงกานีสบนแมกนีเซียมออกไซด์ ที่กระจายตัวสูง (PROPERTIES OF HIGHLY DISPERSED COBALT ON ZEOLITES AND MANGANESE ON MAGNESIUM OXIDE)

อาจารย์ที่ปรึกษา : รองศาสตราจารย์ ดร. จตุพร วิทยาคูณ, 191 หน้า.

ในการสังเคราะห์ซีโอไลต์วาย (NaY) โดยกระบวนการไฮโดรเทอร์มัล เพื่อใช้เป็นตัวรองรับสำหรับตัวเร่งปฏิกิริยา สภาวะที่เหมาะสมที่สุดในการสังเคราะห์คือการบ่มที่อุณหภูมิห้องเป็นเวลา 1 วัน และตกผลึกที่อุณหภูมิ 100 องศาเซลเซียสเป็นเวลา 1 วัน การเปลี่ยนสภาวะในการสังเคราะห์ทำให้ซีโอไลต์วายเกิดการแปรสภาพเป็นซีโอไลต์พี (NaP) โดยสามารถยืนยันการแปรสภาพด้วยเทคนิคการเลี้ยวเบนของรังสีเอ็กซ์ ระยะเวลาในการบ่มส่งผลต่อการแปรสภาพของ ซีโอไลต์วายเพียงเล็กน้อย ในขณะที่ระยะเวลาในการตกผลึกส่งผลกระทบต่อมากกว่า สำหรับซีโอไลต์ที่สังเคราะห์โดยการบ่ม 1 วันและใช้เวลาในการตกผลึก 4 วันนั้น ประกอบด้วยซีโอไลต์พีเป็นส่วนใหญ่ และซีโอไลต์ที่สังเคราะห์โดยการตกผลึกเป็นเวลา 5 วัน ไม่ปรากฏฟิสิกของซีโอไลต์วายเหลืออยู่

ในการนำซีโอไลต์วายมาเป็นตัวรองรับสำหรับตัวเร่งปฏิกิริยาที่มีโคบอลต์ (Co/NaY) และใช้เร่งปฏิกิริยาไฮโดรจิโนไลซิสของนอร์มัลบิวเทน โดยเปรียบเทียบประสิทธิภาพในการเร่งปฏิกิริยากับตัวเร่งปฏิกิริยาโคบอลต์บนตัวรองรับซีโอไลต์ ZSM-5 (Co/ZSM-5) พบว่า ค่าการแปลงผันเมื่อใช้ Co/ZSM-5 สูงกว่า ดังนั้นจึงศึกษาการเร่งปฏิกิริยาโดยใช้ Co/ZSM-5 เพียงตัวเดียวเนื่องจากโลหะโคบอลต์ คือรูปที่สามารถเร่งปฏิกิริยาไฮโดรจิโนไลซิสของนอร์มัลบิวเทน ดังนั้นจึงได้ศึกษาความสามารถในการดูดซับของโคบอลต์ ในตัวเร่งปฏิกิริยาที่อุณหภูมิ 400 องศาเซลเซียส โดยใช้เทคนิค X-ray absorption near edge structure พบว่า ปริมาณการดูดซับของโคบอลต์และค่าการแปลงผันของนอร์มัลบิวเทนมีค่าเพิ่มขึ้นเมื่อปริมาณของโคบอลต์ในตัวเร่งปฏิกิริยาเพิ่มขึ้น เมื่อเติมแพลลาเดียมปริมาณร้อยละ 1 โดยน้ำหนักลงในตัวเร่งปฏิกิริยาโลหะเดี่ยวโคบอลต์ พบว่าตัวเร่งปฏิกิริยาโลหะคู่ที่ได้นั้น ทำให้ความสามารถในการดูดซับและค่าการแปลงผันในปฏิกิริยาไฮโดรจิโนไลซิสไม่เปลี่ยนแปลงอย่างมีนัยสำคัญ ผลลัพธ์ที่ได้จากปฏิกิริยาไฮโดรจิโนไลซิสของนอร์มัลบิวเทน โดยมีตัวเร่งปฏิกิริยาเป็นโลหะเดี่ยวโคบอลต์บนตัวรองรับซีโอไลต์ ZSM-5 (Co/ZSM-5) มีเพียงมีเทน และผลิตภัณฑ์จากปฏิกิริยาดังกล่าวโดยใช้ตัวเร่งปฏิกิริยาเป็นโลหะคู่บนตัวรองรับซีโอไลต์ ZSM-5 (CoPd/ZSM-5) นั้นประกอบด้วยมีเทนเป็นองค์ประกอบหลัก และมีอีเทนและโพรเพนในปริมาณเล็กน้อย

อีกส่วนหนึ่งของงานนี้คือการปรับปรุงความมีแบบแผนและการกระจายตัวของแมงกานีสบนแมกนีเซียมออกไซด์ (MgO) โดยเตรียมจากสารตั้งต้นที่เป็นสารเชิงซ้อนโลหะอินทรีย์ โดยใช้เทคนิคการเคลือบไอเคมี (chemical vapor deposition) สารประกอบ $Mn_2(CO)_{10}$ $Mn(CO)_5H$

และ $\text{Mn}(\text{CO})_5\text{CH}_3$ เมื่อนำมาวางบนตัวรองรับ แล้ววิเคราะห์สเปกตรัมที่สเปกโตรมิเตอร์อินฟราเรด และอิเล็กตรอนพาราแมกเนติกเรโซแนนซ์ พบว่าสเปกตรัมบนพื้นผิวของตัวอย่างที่เตรียมจาก $\text{Mn}_2(\text{CO})_{10}$ และ $\text{Mn}(\text{CO})_5\text{H}$ ประกอบด้วยสารประกอบแมงกานีสคาร์บอนิลหลายชนิดผสมกัน การบำบัดตัวอย่างดังกล่าวในสภาวะออกซิเจนที่อุณหภูมิห้องพบว่า เหลือเพียงแมงกานีสไตรคาร์บอนิลตัวเดียวบนพื้นผิวของ MgO และเลขออกซิเดชันของแมงกานีสในตัวอย่างหลังจากบำบัดด้วยออกซิเจนนั้นมีค่ามากกว่าสอง ในขณะที่ตัวอย่างที่เตรียมจาก $\text{Mn}(\text{CO})_5\text{CH}_3$ และแมกนีเซียมออกไซด์นั้น มีเพียงแมงกานีสเตตระคาร์บอนิล บนพื้นผิวและการบำบัดตัวอย่างนี้ในออกซิเจนที่อุณหภูมิห้องไม่ทำให้เกิดการเปลี่ยนแปลงทั้งในด้านของเลขออกซิเดชัน และจำนวนลิแกนด์คาร์บอนิล



SUPATTRA KHABUANCHALAD : PROPERTIES OF HIGHLY
DISPERSED COBALT ON ZEOLITES AND MANGANESE ON
MAGNESIUM OXIDE. THESIS ADVISOR : ASSOC. PROF. JATUPORN
WITTAYAKUN, Ph.D. 191 PP.

ZEOLITE NaY/ZEOLITE ZSM-5/COBALT/PALLADIUM/*n*-BUTANE
HYDROGENOLYSIS/MANGANESE CARBONYL/MAGNESIUM OXIDE

Zeolite NaY was synthesized by a hydrothermal method and used as a catalyst support. The optimum synthesis condition was 1-day aging time at room temperature and 1-day crystallization time at 100°C. By variation of the synthesis conditions, zeolite NaY transformed to zeolite NaP. The change in the zeolite phase was confirmed by powder X-ray diffraction. The aging time showed a slight effect on the transformation but the crystallization time, with a fixed aging time at 1 day, caused a significant transformation. The NaY phase was not observed after a crystallization time of 4 days and zeolite with NaP as a major phase was obtained after crystallization of 5 days.

The zeolite NaY was used as a support for cobalt catalysts (Co/NaY) in *n*-butane hydrogenolysis and compared to that supported on zeolite ZSM-5 (Co/ZSM-5). The conversion of *n*-butane from Co/NaY was lower than that from Co/ZSM-5, consequently, further study was done only over Co/ZSM-5. Because metallic cobalt is an active form in *n*-butane hydrogenolysis, the reducibility of cobalt catalysts was determined by X-ray absorption near edge structure. In monometallic catalysts (1, 4, 7 and 10 wt% Co/ZSM-5), the reducibility and conversion of *n*-butane

hydrogenolysis increased with the cobalt content. Addition of 1 wt% Pd to the monometallic cobalt did not significantly enhance the reducibility and catalytic activity. Monometallic cobalt catalysts produced only methane whereas bimetallic ones produced trace amount of ethane and propane with methane as main product.

Another part of this work focused on improvement of uniformity and dispersion of manganese supported on magnesium oxide (MgO) prepared from organometallic complexes as metal precursor by chemical vapor deposition. $\text{Mn}_2(\text{CO})_{10}$, $\text{Mn}(\text{CO})_5\text{H}$ and $\text{Mn}(\text{CO})_5\text{CH}_3$ compounds were deposited on MgO and the resulting surface species were characterized by X-ray absorption, electron paramagnetic resonance, and infrared spectroscopies. Deposition of $\text{Mn}_2(\text{CO})_{10}$, $\text{Mn}(\text{CO})_5\text{H}$ on MgO resulted in mixed manganese carbonyl species. Treatment of sample prepared from $\text{Mn}_2(\text{CO})_{10}$ and $\text{Mn}(\text{CO})_5\text{H}$ on MgO in flowing O_2 at room temperature resulted in formation of manganese tricarbonyl species with the oxidation state of manganese higher than +2. In contrast, chemical vapor deposition of $\text{Mn}(\text{CO})_5\text{CH}_3$ on MgO led to the formation of only one surface species, manganese tetracarbonyl, in which the manganese was cationic. The oxidation state and number of carbonyl ligand of manganese remained unchanged after this sample was treated in O_2 .

School of Chemistry

Academic Year 2011

Student's Signature _____

Advisor's Signature _____

ACKNOWLEDGEMENT

I would like to acknowledge:

Assoc. Prof. Dr. Jatuporn Wittayakun, for his kind support, valuable advices and giving thoughtful guidance with knowledge towards the completion of this research; Prof. Bruce C. Gates, for giving me a chance to learn about X-ray absorption spectroscopy as well as experience the synthesis techniques. His guidance is extremely useful for my learning experience; my thesis committee, Asst. Prof. Dr. Kunwadee Rangsriwatananon, Asst. Prof. Dr. Sanchai Prayoonpokarach and Dr. Saowapa Chotisuwan for their helpful suggestions.

I would like to thank my colleagues at Suranaree University of Technology and my colleagues at University of California, Davis, who have shared my working experience and gave me tremendous useful suggestions and encouragements.

In addition, I would like to acknowledge the financial support from the Commission of Higher Education and Suranaree University of Technology.

Finally, I would like to thank my parents and brothers for their love, support, and continual encouragement during my education.

Supattra Khabuanchalad

CONTENTS

	Page
ABSTRACT IN THAI	I
ABSTRACT IN ENGLI	III
ACKNOWLEDGEMENT.....	V
CONTENTS	VI
LIST OF TABLES	XV
LIST OF FIGURES	XVI
LIST OF SCHEMES	XXII
CHAPTER	
I INTRODUCTION	1
1.1 Introduction	1
1.2 Heterogeneous catalysts	2
1.3 Research objectives	3
1.4 Scope and limitations of study.....	6
1.5 References	7
II LITERATURE REVIEW.....	10
2.1 Background of zeolite	10
2.1.1 Zeolite Y	11
2.1.2 Zeolite ZSM-5	12
2.1.3 Magnesium oxide	14

CONTENTS (Continued)

	Page
2.2 Supported metal catalysts.....	14
2.2.1 Preparation of supported metal catalysts.....	15
2.2.2 Characterization of supported metal catalysts.....	16
2.3 References	17
III TRANSFORMATION OF ZEOLITE SODIUM Y	
 SYNTHESIZED FROM RICE HUSK SILICA TO SODIUM P	
 DURING HYDROTHERMAL SYNTHESIS	22
Abstract	22
3.1 Introduction.....	23
3.2 Experimental	24
3.2.1 Materials.....	24
3.2.2 Synthesis of zeolites	25
3.2.3 Characterization of the synthesized zeolites	25
3.3 Results and discussion	26
3.3.1 Effect of aging time on transformation of NaY to NaP.....	26
3.3.2 Effect of crystallization time on the transformation of NaY to NaP.....	27
3.3.3 Characterization of product with 5- day crystallization	29
3.4 Conclusions	33
3.5 References	34

CONTENTS (Continued)

	Page
4.3.6 Catalytic testing of supported cobalt catalysts on ZSM-5.....	61
4.3.6.1 Conversion.....	61
4.3.6.2 Selectivity.....	65
4.4 Conclusion.....	70
4.5 References.....	71
V FORMATION OF MANGANESE TRICARBONYL ON THE MgO SURFACE FROM Mn₂(CO)₁₀ : CHARACTERIZATION BY INFRARED, ELECTRON PARAMAGNETIC RESONANCE, AND X-RAY ABSORPTION SPECTROSCOPIES.....	76
Abstract	76
5.1 Introduction	77
5.2 Experimental	78
5.2.1 Treatment of MgO.....	78
5.2.2 Synthesis of MgO-supported samples from Mn ₂ (CO) ₁₀	79
5.2.3 Sample treatment.....	79
5.2.3.1 Decarbonylation in the presence of H ₂	79
5.2.3.2 Treatment in O ₂	80

CONTENTS (Continued)

	Page
5.2.4 Sample Characterization.....	80
5.2.4.1 IR Spectroscopy.....	80
5.2.4.2 EPR Spectroscopy	81
5.2.4.3 EXAFS Spectroscopy.....	81
5.2.5 EXAFS Data Analysis.....	82
5.2.6 XANES Data Analysis.....	83
5.3 Results.....	84
5.3.1 Spectroscopic characterization of MgO	84
5.3.2 Reaction of $\text{Mn}_2(\text{CO})_{10}$ with partially dehydroxylated MgO.....	85
5.3.2.1 Observations during synthesis.....	85
5.3.2.2 IR evidence of reactions of $\text{Mn}_2(\text{CO})_{10}$ with surface OH groups of MgO.....	87
5.3.2.3 IR evidence of reactions of $\text{Mn}_2(\text{CO})_{10}$ with surface CO_3^{2-} groups of MgO	88
5.3.3 Characterization of sample containing 3.0 wt% Mn	89
5.3.3.1 IR spectra.....	89
5.3.4 Characterization of sample containing 0.10 wt% Mn	90
5.3.4.1 IR spectra.....	90
5.3.4.2 EPR spectra	92

CONTENTS (Continued)

	Page
5.3.5 Characterization of sample containing 1.0 wt% Mn	92
5.3.5.1 IR spectroscopy	92
5.3.5.2 EPR spectroscopy	93
5.3.6 Characterization of sample containing 1.0 wt% Mn following treatment in H ₂	102
5.3.6.1 IR spectra.....	102
6.3.6.2 EPR spectra	102
6.3.6.3 Mass spectra of effluent gas	102
5.3.7 Characterization of sample containing 1.0 wt% Mn following treatment in O ₂	103
5.3.7.1 IR spectra in the ν_{CO} region.....	103
5.3.7.2 Mass spectra of effluent gas	105
5.3.7.3 IR spectra in carbonate region.....	105
5.3.7.4 EPR spectra	107
5.3.7.5 XANES spectra	108
5.3.7.6 EXAFS spectra	108
5.4 Discussion	111
5.4.1 Reaction of Mn ₂ (CO) ₁₀ with MgO	111
4.4.2 Oxidation of initially prepared supported manganese carbonyls	114

CONTENTS (Continued)

	Page
5.5 Conclusions	118
5.6 References	118
VI ADSORPTION OF MANGANESE CARBONYLS $Mn(CO)_5H$ AND $Mn(CO)_5CH_3$ ON PARTIALLY DEHYDROXYLATED MgO	126
Abstract	126
6.1 Introduction	127
6.2 Experimental	130
6.2.1 Synthesis of $Mn(CO)_5H$	130
6.2.2 Synthesis of $Mn(CO)_5CH_3$	131
6.2.3 Synthesis of MgO -supported sample from $Mn(CO)_5H$	131
6.2.4 Synthesis of MgO -supported sample prepared from $Mn(CO)_5CH_3$	132
6.2.5 Treatments of supported samples	133
6.2.6 Spectroscopic characterization of samples	133
6.2.6.1 IR spectroscopy	133
6.2.6.2 EPR spectroscopy	134
6.2.6.3 X-ray absorption spectroscopy	134
6.2.7 Data analysis	135
6.2.7.1 EXAFS data analysis	135

CONTENTS (Continued)

	Page
6.3.7.2 XANES data analysis	137
6.3 Results	137
6.3.1 Adsorption of $\text{Mn}(\text{CO})_5\text{H}$ and of $\text{Mn}(\text{CO})_5\text{CH}_3$ on MgO ...	137
6.3.1.1 Observations during synthesis	137
6.3.2 Characterization of initially prepared samples	137
6.3.2.1 IR spectroscopy	137
6.3.2.2 XANES spectroscopy	143
6.3.2.3 EPR spectroscopy	143
6.3.2.4 EXAFS spectroscopy	145
6.3.3 Characterization of samples after O_2 treatment	147
6.3.3.1 IR spectroscopy	147
6.3.3.2 Mass spectra of effluent gas	148
6.3.3.3 XANES spectroscopy	149
6.3.3.4 EPR spectroscopy	150
6.3.3.5 EXAFS spectroscopy	150
6.4 Discussion	153
6.4.1 Adsorption of $\text{Mn}(\text{CO})_5\text{H}$ on MgO	153
6.4.2 Adsorption of $\text{Mn}(\text{CO})_5\text{CH}_3$ on MgO	157
6.4.3 Comparison of the chemistry of manganese carbonyls and rhenium carbonyls on the surface of MgO	159

CONTENTS (Continued)

	Page
6.5 Conclusions	161
6.6 References	161
VII CONCLUSIONS	170
APPENDICES	173
APPENDIX A EXAFS FITTING CHARACTERIZING Mn ₂ (CO) ₁₀ SUPPORTED ON MgO CONTAINING 1.0 wt% Mn AFTER O ₂ TREATMENT	174
APPENDIX B EXAFS FITTING CHARACTERIZING Mn(CO) ₅ H AND Mn(CO) ₅ CH ₃ ON PARTIALLY DEHYDROXYLATED MgO	179
APPENDIX C N ₂ ADSORPTION-DESORPTION ISOTHERMS OF MONO-AND BIMETALLIC COBALT SUPPORTED ON ZSM-5	186
CURRICULUM VITAE	191

LIST OF TABLES

Table	Page
4.1 Fraction of cobalt species in samples after reduction in H ₂ at 400 °C for 5 h.....	49
4.2 BET surface area of mono- and bimetallic cobalt supported on ZSM-5.....	53
4.3 The fraction of cobalt species in mono- and bimetallic cobalt catalysts after reduction at 400 °C for 5 h determined by linear combination fitting.....	61
5.1 ν_{CO} IR bands characterizing isolated and supported manganese carbonyl complexes.....	94
5.2 EXAFS parameters characterizing sample prepared from Mn ₂ (CO) ₁₀ supported on MgO (1.0 wt% Mn) after O ₂ treatment.....	113
6.1 The EXAFS parameters characterizing sample prepared from Mn(CO) ₅ CH ₃ on MgO.....	146
6.2 The EXAFS parameters characterizing sample prepared from Mn(CO) ₅ H on MgO after O ₂ treatment.....	151

LIST OF FIGURES

Figure	Page
2.1 Structure of FAU framework.....	11
2.2 Structure of MFI framework.....	12
2.3 Normalized XRD patterns of zeolite synthesized with different aging times compared with the patterns of standard zeolite Y and zeolite P.....	27
3.2 Normalized XRD patterns of zeolite synthesized with different crystallization times compared with the patterns of standard zeolite Y and zeolite P.....	28
3.3 FTIR spectrum of product obtained from 1-day aging and 5-day crystallization time.....	30
3.4 SEM image of product obtained from 1-day aging and 5-day crystallization time.....	31
3.5 Particle size distribution of product obtained from 1-day aging and 5-day crystallization time.....	32
3.6 TGA-DTA thermogram of product obtained from 1-day aging and 5-day crystallization time.....	33
4.1 XRD patterns of 7Co1Pd/ZSM-5 and 7Co1Pd/NaY.....	44
4.2 Normalized XANES spectra of 7Co1Pd/NaY and 7Co1Pd/ZSM-5 compared to the standard materials.....	45

LIST OF FIGURES (Continued)

Figure	Page
4.3 Linear combination fit of 7Co1Pd/NaY after reduction at 400°C for 5 h	47
4.4 Linear combination fit of 7Co1Pd/ZSM-5 after reduction at 400°C for 5 h	48
4.5 Conversion of <i>n</i> -butane hydrogenolysis over 7Co1Pd/NaY and 7Co1Pd/ZSM-5	50
4.6 XRD patterns of mono- and bimetallic cobalt catalysts	51
4.7 BET surface area of bimetallic and monometallic cobalt catalysts	54
4.8 Micropore volume of bimetallic and monometallic cobalt catalysts	54
4.9 Linear combination fitting of 1Co/ZSM-5 (A) and 1Co1Pd/ZSM-5 (B) after reduction at 400°C for 5 h	57
4.10 Linear combination fitting of 4Co/ZSM-5 (A) and 4Co1Pd/ZSM-5 (B) after reduction at 400°C for 5 h	58
4.11 Linear combination fitting of 7Co/ZSM-5 (A) and 7Co1Pd/ZSM-5 (B) after reduction at 400°C for 5 h	59
4.12 Linear combination fitting of 10Co/ZSM-5 (A) and 10Co1Pd/ZSM-5 (B) after reduction at 400°C for 5 h	60
4.13 Conversion of monometallic cobalt catalysts	62
4.14 Conversion of bimetallic cobalt catalysts	63
4.15 Conversion per mole cobalt of monometallic cobalt catalysts with different cobalt content	64

LIST OF FIGURES (Continued)

Figure	Page
4.16 <i>n</i> -butane conversion per mole cobalt of bimetallic cobalt catalysts.....	65
4.17 Selectivity of product from <i>n</i> -butane hydrogenolysis over 1Co/ZSM-5 (A) and 4Co/ZSM-5 (B).....	66
4.18 Selectivity of product from <i>n</i> -butane hydrogenolysis over 7Co/ZSM-5 (A) and 10Co/ZSM-5 (B).....	67
4.19 Selectivity of <i>n</i> -butane hydrogenolysis over 1Co1Pd/ZSM-5 (A) and 4Co1Pd/ZSM-5 (B).....	68
4.20 Selectivity of <i>n</i> -butane hydrogenolysis over 7Co1Pd/ZSM-5 (A) and 10Co/ZSM-5 (B).....	69
5.1 EPR spectra (A) of untreated MgO (a), MgO after treatment in O ₂ at 400°C followed by evacuation at the same temperature (b), sample prepared from Mn ₂ (CO) ₁₀ on MgO (0.10 wt% Mn) (c), and sample prepared from Mn ₂ (CO) ₁₀ on MgO (1.0 wt% Mn)(d), and (B) magnification of Figure 5.1A, spectrum b.....	86
5.2 Normalized IR spectra in the ν_{OH} region characterizing samples prepared from Mn ₂ (CO) ₁₀ on MgO: the respective Mn contents (wt%) of the samples were 3.0 (A), 1.0 (B), 0.10 (C), and 0.0 (D).....	87
5.3 Normalized IR spectra in the carbonate region characterizing MgO (A), sample prepared from Mn ₂ (CO) ₁₀ on MgO (1.0 wt% Mn) (B), and after treatment in O ₂ (C)	89

LIST OF FIGURES (Continued)

Figure	Page
5.4 Normalized IR spectra in the ν_{CO} region characterizing a sample prepared from $\text{Mn}_2(\text{CO})_{10}$ on MgO: the respective Mn contents (wt%) of the samples were 0.10 (A), 1.0 (B), and 3.0 (C). Spectrum D corresponds to $\text{Mn}_2(\text{CO})_{10}$ in CH_2Cl_2 solution.....	91
5.5 Normalized IR spectra in the ν_{CO} region of sample prepared from $\text{Mn}_2(\text{CO})_{10}$ and MgO (1.0 wt% Mn) (A), sample from spectrum A after treatment in flowing O_2 (B), and sample from spectrum A after decarbonylation (C).....	104
5.6 EPR spectra of sample prepared from $\text{Mn}_2(\text{CO})_{10}$ and MgO (1.0 wt% Mn) (A), sample from spectrum A after treatment in flowing O_2 (B), and sample from spectrum A after decarbonylation (C).....	105
5.7 Mass spectra of the effluent gases formed by treatment of the sample prepared from $\text{Mn}_2(\text{CO})_{10}$ on MgO (1.0 wt% Mn) in flowing H_2	106
5.8 Mass spectra: the CO^+ signal characterizing the effluent gas formed by treatment of the sample prepared from $\text{Mn}_2(\text{CO})_{10}$ on MgO (1.0 wt% Mn) in flowing O_2 at room temperature	107
5.9 XANES spectra characterizing the sample prepared from $\text{Mn}_2(\text{CO})_{10}$ on MgO (1.0 wt% Mn), after O_2 treatment and manganese foil	109
5.10 XANES calibration data and comparison with edge shift of supported manganese carbonyl species after treatment in O_2	110

LIST OF FIGURES (Continued)

Figure	Page
5.11 EXAFS data characterizing sample prepared from $\text{Mn}_2(\text{CO})_{10}$ on MgO (1.0 wt% Mn) after O_2 treatment.....	114
6.1 a) IR spectra in the ν_{OH} region characterizing MgO (A); the sample prepared by CVD of the precursor $\text{Mn}(\text{CO})_5\text{H}$ on MgO (B); sample prepared by treating the sample represented by spectrum (B) in O_2 at 25°C and $P_{\text{O}_2} = 0.1$ bar (C) (b) spectrum in the ν_{OD} region of characterizing the sample prepared from $\text{Mn}(\text{CO})_5\text{D}$ and MgO.....	138
6.2 IR spectra in OH region of characterizing MgO (A), the sample prepared by CVD of $\text{Mn}(\text{CO})_5\text{CH}_3$ on MgO (1.0 wt% Mn) (B), the sample prepared by treatment of the sample represented by spectrum (B) in O_2 at 25°C and $P_{\text{O}_2} = 0.1$ bar (C)	139
6.3 IR spectrum in the ν_{CO} region characterizing $\text{Mn}(\text{CO})_5\text{H}$ in gas phase (A); sample prepared by chemisorption of $\text{Mn}(\text{CO})_5\text{H}$ on MgO (B); and spectrum of sample represented by spectrum B after O_2 treatment at 25°C and $P_{\text{O}_2} = 0.1$ bar (C)	140
6.4 IR spectrum of $\text{Mn}(\text{CO})_5\text{CH}_3$ in solution with CH_2Cl_2 (A); sample prepared by deposition of $\text{Mn}(\text{CO})_5\text{CH}_3$ on MgO (1.0 wt% Mn) (B); and spectrum of sample represented by spectrum (B) after O_2 treatment at 25°C and $P_{\text{O}_2} = 0.1$ bar (C).....	142

LIST OF FIGURES (Continued)

Figure	Page
6.5	EPR spectra of pretreated MgO (A); samples prepared from chemisorption of $\text{Mn}(\text{CO})_5\text{H}$ into MgO (B), sample prepared from chemisorption of $\text{Mn}(\text{CO})_5\text{H}$ into MgO after treatment in O_2 (C) 144
6.6	EXAFS data characterizing sample prepared from $\text{Mn}(\text{CO})_5\text{CH}_3$ on MgO (1.0 wt% Mn) after O_2 treatment 147
6.7	Mass spectrum data: the CO^+ signal characterizing the effluent gas formed by treatment of the sample prepared from $\text{Mn}(\text{CO})_5\text{H}$ on MgO in flowing O_2 ($P_{\text{O}_2} = 0.1$ bar) at room temperature 149
6.8	EXAFS data characterizing sample prepared from $\text{Mn}(\text{CO})_5\text{H}$ on MgO (1.0 wt% Mn) after O_2 treatment 152
6.9	XANES calibration data and comparison with edge shift of sample prepared from $\text{Mn}(\text{CO})_5\text{H}$ and MgO after O_2 treatment 155

LIST OF SCHEMES

Scheme	Page
5.1 Proposed structure of surface manganese tricarbonyl species prepared from $\text{Mn}_2(\text{CO})_{10}$ on MgO (1.0 wt% Mn) after O_2 treatment.....	117
6.1 Proposed structure of surface manganese tricarbonyl species prepared from $\text{Mn}(\text{CO})_5\text{H}$ on MgO after O_2 treatment.....	157
6.2 Proposed structure of surface manganese tetracarbonyl species prepared from $\text{Mn}(\text{CO})_5\text{CH}_3$ on MgO (1.0 wt% Mn).....	159
6.3 Proposed chemistry of manganese carbonyls on the surface of MgO	160
6.4 Proposed chemistry of rhenium carbonyls on the surface of MgO	160

CHAPTER I

INTRODUCTION

1.1 Introduction

Many industrial reactions are operated under harsh conditions including high temperature and pressure in order to achieve the economic rates of production. These severe conditions are energy intensive, corrosive and could cause damage to equipment. Moreover, it could result in undesired side reactions and products (Farrauto and Batholomew, 1997).

The use of catalysts provides an opportunity to run chemical reactions under less severe conditions and more selectively than without catalysts. There are two types of catalysts that have been used in the chemical reactions, solid and soluble catalysts. The solid catalysts play an important role in industrial applications, since approximately 90% of all chemical processes, including chemical, food, pharmaceutical, automobile and petrochemical industries, uses heterogeneous catalysts (J. M., Thomas and W. J., Thomas, 1997; Chorkendorff and Niemantsverdriet, 2003; and van Santen et al., 1997).

1.2 Heterogeneous catalysis

In a catalytic process, the reactants and products undergo several steps on solid catalysts (Dumesic et al., 2008), including (1) diffusion of the reactants

through a boundary layer surrounding the catalyst particle, (2) diffusion of the reactants into the catalysts pores to the active site, (3) adsorption of reactant onto reactive sites, (4) surface reactions involving formation or conversion of various adsorbed intermediates, possibly including surface diffusion steps, (5) desorption of products from catalytic sites, (6) diffusion of the products through the catalyst pores, and (7) diffusion of the products across the boundary layer surrounding the catalysts particles.

The effective method to improve a performance of heterogeneous catalysts is to disperse an active metal over the surface of a support, which is typically a high surface area oxide such as Al_2O_3 , SiO_2 , or zeolites. The supported metal materials are effective as catalysts because the active metallic phase is presented as extremely small particles and they are firmly anchored to the support and are separated from each other. Thus the active metal particles may not readily coalesce, or sinter, during the catalytic process (Bond, 1993).

It has been reported that the use of active metal dispersed on support could enhance catalyst performance, and its catalytic activity also depends on the degree of metal dispersion. Zhang et al. (2008) prepared Ni-Co bimetallic catalysts supported on Al-Mg-oxide. They found that the catalyst with lower Ni-Co content has better metal dispersion and therefore, gave rise to better catalytic performance in CO_2 reforming of CH_4 to produce syn gas. The report from Göhlich et al. (2011) also revealed that the hydrodearomatization of toluene to light alkanes over Pt/H-ZSM-5 catalyst produced more CH_4 when catalyst had a high Pt dispersion. Furthermore, a low Pt dispersion led to a faster deactivation at higher time on stream.

Besides the metal dispersion, the performance of supported metal catalyst also depends on a variety of parameters including particle size and shape, catalyst surface structure, local composition and chemical bonding, interactions between the metal particle and support material and parameters during the catalyst synthesis and pretreatment (Zhou et al., 2011). For example, Lobo-Lapidus and Gates (2009) reported that the activity for *n*-butane hydrogenolysis of rhenium clusters supported on γ -Al₂O₃ varied with the sizes of rhenium cluster, namely, Re₁₀ > Re₃ > mononuclear Re. Likewise, activity and selectivity for *n*-butane hydrogenolysis on Rh supported on Al₂O₃ catalysts depended on the size of metal particles; on large particles the activity for this reaction was slightly increased and the central cleavage of *n*-butane became favored (Maroto-Valiente, 2004).

In this work, the hydrogenolysis of *n*-butane was used to probe the performance of catalysts. Hydrogenolysis can be defined as the breakage of carbon-carbon bonds with the uptake of hydrogen. The hydrogenolysis reaction of simple alkanes on supported metal catalysts has been known for many years and has been investigated by many researchers (Caeiro et al., 2006; Bond and Hooper, 2006; Cortright et al., 1999; Scirè et al., 2006). The direct use of *n*-butane provides less attractive alternative to the processes that are currently based on the economically industrial feedstock. Thus, transformation of *n*-butane into more interesting molecule is employed by hydrogenolysis. For example, *n*-butane can be converted to ethane, which is further transformed to ethylene, an important monomer in polymer industries. The *n*-butane can be transformed into *i*-butane (Guisnet and Gnep, 1996) which is widely used in alkylation units for the production of high octane C₈

branched alkanes. Moreover, *i*-butane is dehydrogenated into isobutylene for the production of methyl tertiary butyl ether (MTBE) (Caeiro et al., 2006).

Because catalyst performance is largely influenced by the structure of catalysts, chemical and structural characterization becomes an essential requirement to identify the structural-performance relationships. Uniformity of catalysts not only influences their selectivity but also allows precise characterization (Fierro-Gonzalez et al., 2006). A typical method to prepare highly uniform supported metal catalyst is to use an organometallic complex as a metal precursor. For example, the preparation of manganese oxide and cobalt oxide supported on zirconia by using metal-EDTA complexes as precursors resulted in a highly uniform active phase (Boot et al., 1996). In another example, the nearly uniform supported carbonyl cluster approximated as decaosmium was prepared by reductive carbonylation of adsorbed $\text{Os}_3(\text{CO})_{12}$ on MgO at 275 °C (Kulkarni et al., 2009). Complexes with carbonyl ligand are widely used as metal precursors because the carbonyl can be removed easily under mild conditions. Chotisuwan et al. (2006) prepared catalysts by adsorption of $\text{Pt}_3\text{Ru}_6(\text{CO})_{21}-(\mu_3\text{-H})(\mu\text{-H})_3$ on $\gamma\text{-Al}_2\text{O}_3$ and decarbonylation by treatment in He at 300 °C. Characterization of samples after decarbonylation showed that the composition of that metal frame remained unchanged. The material was active for ethylene hydrogenation and *n*-butane hydrogenolysis under conditions mild enough to prevent the cluster disruption.

The first part of this thesis focused on synthesis of zeolite NaY and zeolite ZSM-5 and their use as supports for cobalt catalysts. Transformation of zeolite NaY to NaP under various crystallization conditions was also investigated (Chapter III). The cobalt catalysts supported on zeolite NaY and ZSM-5 were characterized by

XRD, XANES, and BET techniques and their activities for *n*-butane hydrogenolysis was investigated (CHAPTER IV). Besides the supported cobalt catalysts, the preparation and characterization of highly uniform manganese carbonyl complexes supported on MgO was also studied. Binuclear manganese carbonyls (CHAPTER V) and mononuclear manganese carbonyls (CHAPTER VI) were deposited on MgO by a chemical vapor deposition (CVD) method. The manganese carbonyl complexes supported on MgO were investigated by using the complementary of IR, EPR and XAS spectroscopies.

1.3 Research objectives

- 1.3.1 To synthesize zeolite NaY and investigate the conditions that allow transformation of zeolite NaY to zeolite NaP, and its use as a support for supported cobalt catalysts for *n*-butane hydrogenolysis.
- 1.3.2 To compare (a) the activity in *n*-butane hydrogenolysis of supported cobalt catalysts prepared from zeolite NaY and ZSM-5, (b) the effect of cobalt content, and (c) the influence of Pd on supported cobalt catalysts.
- 1.3.3 To prepare and characterize highly uniform samples prepared from manganese carbonyl complexes including $\text{Mn}_2(\text{CO})_{10}$, $\text{Mn}(\text{CO})_5\text{H}$, and $\text{Mn}(\text{CO})_5\text{CH}_3$ on MgO.

1.4 Scope and limitations of study

- 1.4.1 Zeolite NaY and NaZSM-5 were synthesized from rice husk silica.
- 1.4.2 The transformation of zeolite NaY to NaP was investigated by changing the aging time and the crystallization time.
- 1.4.3 Cobalt catalysts with zeolite NaY and zeolite NaZSM-5 as supports were prepared by the incipient wetness impregnation method by using $\text{Pd}(\text{CH}_3\text{COO})_2$ and $\text{Co}(\text{NO}_3)_2 \cdot 6\text{H}_2\text{O}$ as metal precursors.
- 1.4.4 The supported cobalt catalysts were characterized by techniques and instruments available at Suranaree University of Technology, Synchrotron Light Research Institute (Public Organization).
- 1.4.5 The activity for *n*-butane hydrogenolysis of the supported cobalt catalysts was investigated by using a plug flow reactor.
- 1.4.6 The manganese carbonyl complexes $\text{Mn}(\text{CO})_5\text{H}$, $\text{Mn}(\text{CO})_5\text{D}$, and $\text{Mn}(\text{CO})_5\text{CH}_3$ were synthesized from $\text{Mn}(\text{CO})_5\text{Br}$.
- 1.4.7 Highly uniform samples were prepared by treatment of MgO-supported manganese samples in flowing O_2 at room temperature.
- 1.4.8 The supported manganese samples were characterized by electron paramagnetic resonance, X-ray absorption and infrared spectroscopies.

1.5 References

- Bond, G. C. (1993). Strategy of research on supported metal catalysts. Problems of structure-sensitive reactions in the gas phase. **Acc. Chem. Res.** 26: 490-495.
- Bond, G. C. and Hooper, A. D. (2006). Kinetic analysis of *n*-butane hydrogenolysis on a Ru/Al₂O₃ catalyst. **React. Kinet. Catal. Lett.** 87(2): 325-334.
- Boot, L. A., Kerkhoffs, M. H. J. V., van der Linden, B., T., van Dillen, A. J., Geus, J. W., and van Buren, F. R. (1996). Preparation, characterization and catalytic testing of cobalt oxide and manganese oxide catalysts supported on zirconia. **Appl. Catal. A-Gen.** 137: 69-86.
- Caeiro, G., Carvalho, R. H., Wang, X., Lemos, M. A. N. D. A., Lemos, F., Guisnet, M., and Ribeiro, F. R. (2006). Activation of C₂-C₄ alkanes over acid and bifunctional zeolite catalysts. **J. Mol. Catal.** 255: 131-158.
- Chorkendorff, I. and Niemantsverdriet, J. W. (2003). **Concepts of modern catalysis and kinetics**, Weinheim: Wiley-VCH.
- Chotisuwan, S., Wittayakun, J., and Gates, B. C. (2006). Pt₃Ru₆ Clusters Supported on γ -Al₂O₃: synthesis from Pt₃Ru₆(CO)₂₁(μ ₃-H)(μ -H)₃, structural characterization, and catalysis of ethylene hydrogenation and *n*-butane hydrogenolysis. **J. Phys. Chem. B** 110: 12459-12469.
- Cortright, R. D., Watwe, R. M., Spiewak, B. E., and Dumesic, J. A. (1999). Kinetics of ethane hydrogenolysis over supported platinum catalysts. **Catal. Today.** 53: 395-406.
- Dumesic, J. A., Huber, G. W., and Boudart, M. (2008). **Handbook of Heterogeneous Catalysis**. (2nd ed.). Weinheim: Wiley-VCH.

- Farrauto, R. J. and Batholomew, C. H. (1997). **Fundamentals of industrial catalytic processes**. London: Blackie Academic & Professional.
- Fierro-Gonzalez, J. C., Kuba, S., Hao, Y., and Gates, B. C. (2006). Oxide- and zeolite-supported molecular, metal complexes and clusters: physical characterization and determination of structure, bonding, and metal oxidation state. **J. Phys. Chem. B** 110: 13326-13351.
- Göhlich, M., Böttcher, S., Räuchle, K., and Reschetilowski, W. (2011). Influence of platinum dispersion on the hydrodearomatization of toluene to light alkanes on Pt/H-ZSM-5. **Catal. Commun.** 12: 757-760.
- Guisnet, M. and Gnep, N. S. (1996). Mechanism of short-chain alkane transformation over protonic zeolites. Alkylation, disproportionation and aromatization. **Appl. Catal. A-Gen.** 146(1): 33-64.
- Kulkarni, A., Mehraeen, S., Reed, B. W., Okamoto, N. L., Browning, N. D., and Gates, B. C. (2009). Nearly uniform decaosmium clusters supported on MgO: characterization by X-ray absorption spectroscopy and scanning transmission electron microscopy. **J. Phys. Chem. C** 113: 13377-13385.
- Lobo-Lapidus, R. J. and Gates, B. C. (2009). Rhenium complexes and clusters supported on γ -Al₂O₃: Effects of rhenium oxidation state and rhenium cluster size on catalytic activity for *n*-butane hydrogenolysis. **J. Catal.** 268: 89-99.
- Maroto-Valiente, A., Rodríguez-Ramos, I., and Guerrero-Ruiz, A. (2004). Surface study of rhodium nanoparticles supported on alumina. **Catal. Today.** 93-95: 567-574.

- Scirè, S., Burgio, G., Crisafulli, C., and Minicò, S. (2006). One-step conversion of *n*-butane to isobutene over H-beta supported Pt and Pt, M (M = Cu, In, Sn) catalysts: An investigation on the role of the second metal. **J. Mol. Catal. A-Chem.** 260: 109-114.
- Thomas, J. M. and Thomas, W. J. (1997). **Principles and practice of heterogeneous catalysis.** Weinheim: Wiley-VCH.
- van Santen, R. A., Leeuwen, P. W. N. M. van, Mooulijn, J. A., and Averill, B. A. (1999). **Catalysis: An integrated approach,** Amsterdam: Elsevier Science.
- Zhang, J., Wang, H., and Dalai, A. K. (2008). Effects of metal content on activity and stability of Ni-Co bimetallic catalysts for CO₂ reforming of CH₄. **Appl. Catal. A-Gen.** 339: 121-129.
- Zhou, W., Wachs, I. E., and Kiely, C. J. (2011) Nanostructure and chemical characterization of supported metal oxide catalysts by aberration corrected analytical electron microscope. **Curr. Opin. Solid. St. M.** (in press).

CHAPTER II

LITERATURE REVIEW

2.1 Background of zeolite

Zeolites are well-defined crystalline aluminosilicate materials with three-dimensional structures arising from a framework of $[\text{SiO}_4]^{4-}$ and $[\text{AlO}_4]^{5-}$. The frameworks are open and contain channels and cavities in which cations and water molecules are located. The cations often have a high degree of mobility giving rise to facile movement of the water molecules that are readily lost and regained; this property accounts for the well-known desiccant properties of zeolites. Because zeolites have porous structure with regular arrays of apertures, they have size selectivity that take molecules with sizes smaller than pore diameter into their porous structures and reject molecules with sizes larger than pore diameter. This is the property of molecular sieving largely unique to zeolites and responsible for their first commercial success (Dyer, 1988).

The assembly of tetrahedral $[\text{SiO}_4]^{4-}$ and $[\text{AlO}_4]^{5-}$ through their oxygen atoms also creates the infinite lattice composed of identical building blocks or unit cells, with their symmetry related to the classification of zeolite structure. In this work, zeolite NaY and zeolite NaZSM-5 were synthesized and used as supports for catalysts.

2.1.1 Zeolite Y

Structure of zeolite Y is classified as a faujasite (FAU) type framework, which contains unit cells of double 6-rings consisting of a very large cavity with four 12-oxygen ring windows (Figure 2.1).

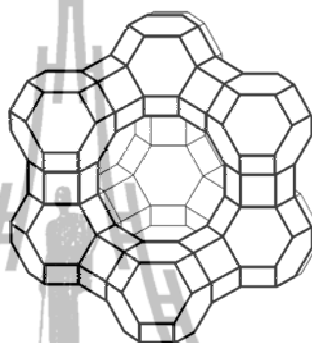


Figure 2.1 Structure of FAU framework.

Generally, zeolite Y is synthesized in a gelling process. Alumina and silica sources are mixed in alkaline aqueous solutions to give a gel. The gel is then usually heated to 70-300°C to crystallize the zeolite (Bhatia, 1990). The crystallization condition is an important factor to induce the transformation of zeolite Y into the other zeolites (Sang et al., 2006). Wittayakun et al. (2008) prepared zeolite NaY by hydrothermal process by using rice husk as a silica source. Various aging and crystallization conditions led to the transformation of zeolite NaY to zeolite NaP.

The most important use of zeolite Y is as a cracking catalyst. For example, Kuznetsov (2003) reported that Pt/HY zeolite is an effective catalyst for *n*-octane hydrocracking. The report from Hopkins et al. (1996) and Williams et al. (2000) showed that ultrastable zeolite Y (USY) was used as a catalyst for cracking of hexane without addition of active metal. The acid sites presented in USY was reported to be

active for alkane cracking. Besides cracking, zeolite Y is also used in the hydrogenolysis reaction. Banu et al. (2011) reported that the conversion of sorbitol hydrogenolysis on 6% Ni/NaY catalyst was approximately 75%. In addition, Mériaudeau et al. (1997) reported that propane hydrogenolysis rate on Pt_{1.7}/NaY was approximately 78 mmol h⁻¹ g⁻¹ catalyst at 450°C.

The other applications of zeolite Y are to be used for a separation of carbon dioxide and nitrogen gases (White et al., 2010), used for removal of heavy metal from the solution (Keane, 1998) or used in fuel cell application (Ahmad et al., 2006).

2.1.2 Zeolite ZSM-5

Zeolite ZSM-5, with an MFI type framework, consists of pentasil units linked together by oxygen bridges to form pentasil chains. Each pentasil unit composed of eight five-membered rings. The pentasil chains are interconnected by oxygen bridges to form corrugated sheets with 10-ring holes (Figure 2.2) (McCusker, 2005).

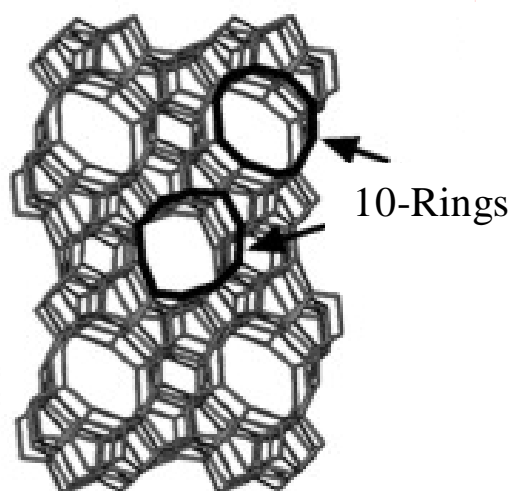


Figure 2.2 Structure of MFI framework.

Zeolite ZSM-5 is typically prepared from SiO_2 , NaAlO_2 and a template, $\text{N}(\text{CH}_2\text{CH}_2\text{CH}_3)_4\text{Br}$, at high temperature and high pressure in a Teflon-coated autoclave (Lermer et al., 1985). In addition, ZSM-5 can be synthesized without using a template (Cheng et al., 2006), but the template-free method produced zeolites with lower structural stability.

Zeolite ZSM-5 itself can be used as a catalyst, exemplified by the use of H-ZSM-5 in the conversion of *n*-butane to *i*-butane, (Kumar et al., 2002). The catalytic activity of nanosize crystallites of ZSM-5 for cracking of 1,3,5-triisopropylbenzene increased 1.3 times from big (82.8 nm) to small (20.7 nm) crystallite (Marales-Pacheo et al., 2011). Zeolite ZSM-5 can be used as a support for active metals. For example, palladium was impregnated into ZSM-5 and used as a catalyst for the combustion of methane (Zhang et al., 2008). The Pt/HZSM-5 catalyst was reported to be used in hydroisomerization of *meta*-xylene (Aboul-Gheit et al., 2001) and Co/ZSM-5 was used for the reduction of NO_x with iso-butane (Wang et al., 2000).

Furthermore, ZSM-5 is also used as membrane due to its size selective property. It was incorporated with poly vinyl alcohol (PVA) and use as a membrane for pervaporation separation of methanol–benzene mixtures (Teli et al., 2011). Sun et al. (2009) prepared Sn-ZSM-5 zeolite supported on $\alpha\text{-Al}_2\text{O}_3$ tubes and used it as a membrane for separation of acetic acid/water mixtures.

2.1.3 Magnesium oxide

Magnesium oxide consists of a lattice of Mg^{2+} ions and O^{2-} ions held together by ionic bonds. The most conventional method for synthesis of MgO is the decomposition of various magnesium salts or magnesium hydroxide ($\text{Mg}(\text{OH})_2$) (Ding et al., 2001). The different Mg–O pairs exist at the surface of MgO, where Mg^{2+} and O^{2-} ions have different coordination numbers depending on their location (terrace, corner, or edge). The basic sites are generally considered to be oxide ions of low coordination, denoted by O_{LC}^{2-} (where LC = 3C, 4C, and 5C refer to tri-, tetra-, and penta-coordinated oxide ions, respectively). Treatment of MgO at increasing temperature led to the removal of contaminants and progressively led to stronger basic sites (Bailly et al., 2005).

2.2 Supported metal catalyst

Supported metal catalysts may be composed of three components: (1) an active phase (2) a promoter, which increases the activity, selectivity and/or stability, and (3) high surface area support that serves to facilitate the dispersion and stability of active phase.

Active phase are usually dispersed on the surface of support in the form of microcrystallites of 1-50 nm diameter. The surface of these crystallites contain active sites for catalyzing various reactions. Promoters are added in small amounts compared to that of active phase. The function of a promoter is to maintain catalytic surface and/or increase the activity (Farrauto and Batholomew, 1997). For example, the addition of small quantities of Ca or Mg into Ni/ α - Al_2O_3 catalysts can improve the activity and selectivity for the steam reforming of hydrocarbon (Lisboa et al.,

2005). The supports refers to the high-surface-area carrier (typically oxides or carbons) that facilitate preparation of well dispersed active phases and improve the thermal stability of the active phase over long period of time.

2.2.1 Preparation of supported metal catalysts

The preparation of supported metal catalysts includes various steps including preparation of the support, deposition of active components onto a support and catalyst activation. There are several methods to apply the active components onto the support, for example, impregnation, adsorption, chemical vapor deposition, ion-exchange and precipitation. In this work, the incipient wetness impregnation and chemical vapor deposition were used in the catalysts preparation.

Incipient wetness impregnation

Incipient wetness impregnation involves bringing the solution containing a salt of an active ion into the pores of support. The amount of solution used in this technique is low and the whole active component is expected to be retained on the support since there is no washing step involving in this technique. The mixing of active ion salt solution and support produces a paste with a distribution of active ion as homogeneous as possible. The paste is subsequently dried and heated to decompose the salt of active ion (Marceau et al., 2008).

Chemical vapor deposition (CVD) method

Chemical vapor deposition is a reaction that occurs by the adsorption of the gas phase (precursor) onto the support. No solvent is required. However, the choices of salt precursor are limited due to their characteristics including; (1) stability at room temperature, (2) sufficient volatility at room temperature, (3) capability of being

produced at a high purity, (4) an ability to react with support without side reactions (Pierson, 1992).

2.2.2 Characterization of supported metal catalysts

Understanding structure of supported metal catalysts is necessary because of the relationship among the physical, chemical properties and catalytic activity. Besides, characterization of catalysts provides an opportunity to determine the cause of deactivation as well as monitor the changes in physical and chemical properties of catalysts during the preparation, activation and reaction testing. The characterization tools used in this work includes the following techniques.

Fourier transform infrared spectroscopy (FTIR) is used to analyze the interaction between two atoms. The incident electromagnetic wave is adsorbed by a molecule upon excitation of molecular vibration modes. The frequency of these vibrations depend on the nature and binding of the molecules. This technique can be used to analyze the catalyst surface during the reaction (*in situ* conditions).

X ray diffraction spectroscopy (XRD) is used to characterize bulk crystal structure and chemical phase composition by the diffraction of an X-ray beam as a function of the angle of the incident beam. Broadening of the diffraction peaks can be used to estimate crystallite diameter.

Electron paramagnetic resonance (EPR) spectroscopy is a technique for investigating paramagnetic species by measuring the interaction of an external magnetic field with the unpaired electron(s) in paramagnetic species.

X-ray absorption (XAS) spectroscopy is a technique that measures the absorption of X-rays as a function of their energy. The energy of the X-rays is varied in the range that the core electrons can be excited. When the energy of an X-ray is

equal to the binding energy of a core electron, the core electron will be ejected from atom and cause a sharp rise in the absorption spectrum. This region is known as the X-ray Absorption Near Edge Structure (XANES) region. The absorption at an energy 50 eV above the sharp rise is called the Extended X-ray Absorption Fine Structure (EXAFS) which corresponds to the scattering between ejected electrons and electrons of neighboring atoms. The spectrum in XANES region provides information about formal valence, coordination environment, (e.g. octahedral, tetrahedral coordination) and subtle geometrical distortions of it. The EXAFS region provides information including the bond distance and the number of atoms surrounding the atom that absorbs X-ray energy.

N₂ adsorption-desorption analysis is a technique that represents the physical adsorption and desorption of gas molecules on a solid surface. Based on the Brunauer Emmett and Teller (BET) equation, data representing the adsorption desorption characteristics can be used to measure the surface area and porosity of material.

2.3 References

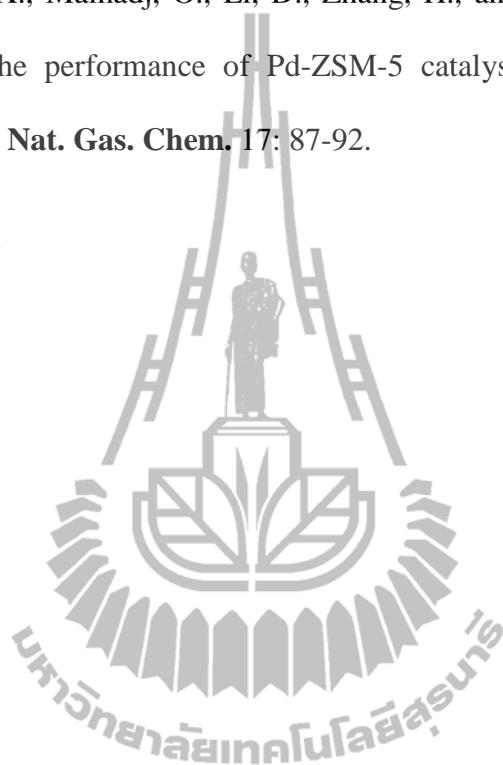
- Aboul-Gheit, A. K., Abdel-Hamid, S. M., and El-Desouki, D. S. (2001). Catalytic *para*-xylene maximization IV. Hydroisomerization of *meta*-xylene on catalysts containing platinum on differently steamed H-ZSM-5. **Appl. Catal. A-Gen.** 209: 179-191.
- Ahmad, I., Javaid Zaidi, S. M., Rahman, S. U., and Ahmed, S. (2006). Synthesis and proton conductivity of heteropolyacids loaded Y-zeolite as solid proton conductors for fuel cell applications. **Micropor. Mesopor. Mat.** 91: 296-304.

- Bailly, M. L., Chizallet, C., Costentin, G., Krafft, J. M., Lauron-Pernot, H., and Che, M. (2005). A spectroscopy and catalysis study of the nature of active sites of MgO catalysts: Thermodynamic Brønsted basicity versus reactivity of basic sites. **J. Catal.** 235: 413-422.
- Banu, M., Sivasanker, S., Sankaranarayanan, T. M., and Venuvanalingam, P. (2011). Hydrogenolysis of sorbitol over Ni and Pt loaded on NaY. **Catal. Commun.** 12: 673-677.
- Bhatia, S. (1990). **Zeolite Catalysis: Principles and Applications**. Florida: CRC Press.
- Cheng, Y., Liao, R., Li, J., Wang, L., and Sun, X. (2006). Synthesis of ZSM-5 zeolite membranes without organic templates using a varying-concentration technique. **Rare Metals.** 25(6): 384-389.
- Ding, Y., Zhang, G., Wu, H., Hai, B., Wang, L., and Qian, Y. (2001). Nanoscale Magnesium Hydroxide and Magnesium Oxide Powders: Control over Size, Shape, and Structure via Hydrothermal Synthesis. **Chem. Mater.** 13: 435-440.
- Dyer, A. (1988). **An introduction to Zeolite Molecular Sieves**. New York: John Wiley & Sons.
- Farrauto, R. J. and Batholomew, C. H. (1997). **Fundamentals of industrial catalytic processes**. New York: Blackie Academic & Professional.
- Hopkins, P. D., Miller, J. T., Meyers, B. L., Ray, G. J., Roginski, R. T., Kuehne, M. A., and Kung, H. H. (1996). Acidity and cracking activity changes during coke deactivation of ultrastable Y zeolite. **Appl. Catal. A-Gen.** 136: 29-48.

- Keane, M. A. (1998). The removal of copper and nickel from aqueous solution using Y zeolite ion exchangers. **Colloid. Surface A.** 138: 11-20.
- Kumar, N., Nieminen, V., Demirkan, K., Salmi, T., Murzin, D. Y., and Laine, E. (2002). Effect of synthesis time and mode of stirring on physico-chemical and catalytic properties of ZSM-5 zeolite catalysts. **Appl. Catal. A-Gen.** 235: 113-123.
- Kuznetsov, P. N. (2003). Study of *n*-octane hydrocracking and hydroisomerization over Pt/HY zeolites using the reactors of different configurations. **J. Catal.** 218: 12-23.
- Lermer, H., Draeger, M., Steffen, J., and Unger, K. K. (1985). Synthesis and structure refinement of ZSM-5 single crystals. **Zeolites.** 5(3): 131-134.
- Lisboa, J. S., Santos, D. C. R. M., Passos, F. B., and Noronha, F. B. (2005). Influence of the addition of promoters to steam reforming catalysts. **Catal. Today.** 101: 15-21.
- Marceau, E., Carrier, X., Che, M., Clause, O., and Marcilly, C. (2008). **Handbook of Heterogeneous Catalysis** (2nd ed.). Weinheim: Wiley-VCH.
- McCusker, L. B. and Baerlocher, C. (2005). Zeolite structure. In Čejka, J. and van Bekkum, H. (eds.). **Zeolites and Ordered Mesoporous Materials: progress and prospects.** (Vol. 157, pp 41). Amsterdam: Elsevier.
- Mériaudeau, P., Thangaraj, A., Dutel, J. F., and Naccache, C. (1997). Studies on Pt_xSn_y Bimetallics in NaY II. Further Characterization and Catalytic Properties in the Dehydrogenation and Hydrogenolysis of Propane. **J. Catal.** 167: 180-186.

- Morales-Pacheco, P., Domínguez, J. M., Bucio, L., Alvarez, F., Sedran, U., and Falco, M. (2011). Synthesis of FAU(Y)- and MFI(ZSM5)- nanosized crystallites for catalytic cracking of 1, 3, 5-triisopropylbenzene. **Catal. Today.** 166: 25-38.
- Pierson, H. O. (1992). **Handbook of Chemical Vapor Deposition-Principles, Technology and Applications.** New Jersey: Noyes.
- Sang, S., Liu, Z., Tian, P., Liu, Z., Qu, L., and Zhang, Y. (2006). Synthesis of small crystals zeolite NaY. **Mater. Lett.** 60: 1131-1133.
- Sun, W., Wang, X., Yang, J., Lu, J., Han, H., Zhang, Y., and Wang, J. (2009). Pervaporation separation of acetic acid–water mixtures through Sn-substituted ZSM-5 zeolite membranes. **J. Membrane. Sci.** 335: 83-88.
- Teli, S. B., Calle, M., and Li, N. (2011). Poly(vinyl alcohol)-H-ZSM-5 zeolite mixed matrix membranes for pervaporation separation of methanol–benzene mixture. **J. Membrane. Sci.** 371: 171-178.
- Wang, X., Chen, H. Y., and Sachtler, W. M. H. (2000). Catalytic reduction of NO_x by hydrocarbon over Co/ZSM-5 catalysts prepared with different methods. **Appl. Catal. B-Environ.** 26: L227-L239.
- White, J. C., Dutta, P. K., Shqau, K., and Verweij, H. (2010). Synthesis of Ultrathin Zeolite Y membranes and their application for separation of carbon dioxide and nitrogen gases. **Langmuir.** 26(12): 10287-10293.
- Williams, B. A., Ji, W., Miller, J. T., Snurr, R. Q., and Kung, H. H. (2000). Evidence of different reaction mechanisms during the cracking of *n*-hexane on H-USY zeolite. **Appl. Catal. A-Gen.** 203: 179-190.

- Wittayakun, J., Khemthong, P., and Prayoonpokarach, P. (2008). Synthesis and characterization of zeolite NaY from rice husk silica. **Korean J. Chem. Eng.** 25(4): 861-864.
- Zhang, B., Wang, X., Mamadj, O., Li, D., Zhang, H., and Lu, G. (2008). Effect of water on the performance of Pd-ZSM-5 catalysts for the combustion of methane. **J. Nat. Gas. Chem.** 17: 87-92.



CHAPTER III

TRANSFORMATION OF ZEOLITE SODIUM Y SYNTHESIZED FROM RICE HUSK SILICA TO SODIUM P DURING HYDROTHERMAL SYNTHESIS

Abstract

This chapter focuses on the synthesis of zeolite NaY and investigation of its transformation to NaP by variation the synthesized conditions. Rice husk silica powder with approximately 98% purity was used as a silica source for zeolite syntheses. The transformation of zeolite NaY to zeolite NaP was investigated during hydrothermal synthesis at 100 °C by fixing the mass ratio of SiO₂, Al₂O₃, and Na₂O at 10:1:4.6. The studied parameters included aging time (1, 2, and 3 days) and crystallization time (1, 2, 3, 4, and 5 days). The change in phase of zeolite was observed by powder X-ray diffraction. The aging time did not have much effect on the transformation. When the crystallization time was fixed at 1 day, the synthesis with 1-day aging produced pure phase NaY and that with 2- and 3-day produced only a small amount of NaP. In contrast, changes of the crystallization time, with a fixed aging time at 1 day, caused a significant transformation. The transformation of NaY to NaP was observed in the synthesis with crystallization of 2 days and the amount of NaP increased with the crystallization time. The NaY phase was not observed after a crystallization time of 4 days and high purity NaP was obtained after crystallization

of 5 days. Consequently, the synthesis condition with an aging time of 1 day and crystallization time of 5 days was the optimum condition for the transformation. Scanning electron micrographs at this optimum condition showed a narrow size distribution in the range of 7-14 μm .

3.1 Introduction

Zeolite P class includes a series of synthetic zeolite phases such as cubic configuration (also termed B or P_c) or tetragonal configuration (also termed P_t). Its conformation depends on the extra-framework ion, the state of dehydration and the chemical composition (Nery et al., 2003). The zeolite P class has the typical oxide formula: $M_{2/n}O \cdot Al_2O_3 \cdot 1.80-5.00SiO_2 \cdot 5H_2O$, where M is an n-valent cation, normally an alkali metal. Crystallites of zeolite P with Si/Al ratios from 0.9 to 1.33 are useful as molecular sieves and detergent builders (Huang et al., 2001). Zeolite P can be synthesized from various silica sources and methods, for example, from a natural clay, Kaolinite, and crystallization at 75-85 $^{\circ}\text{C}$ (Sathupunya et al., 2002); from coal fly ash by agitation at 120 $^{\circ}\text{C}$ (Murayama et al., 2002); or from sodium aluminate and sodium silicate solution by hydrothermal treatment in a microwave oven (Zubowa et al., 2008).

Sang et al. (2006) synthesized small crystals of zeolite NaY by hydrothermal method and found that crystallization at 120 $^{\circ}\text{C}$ caused the formation of zeolite NaP instead of zeolite NaY. Moreover, in the synthesis of zeolite NaY with rice husk silica (RHS), zeolite NaP was observed when the crystallization at 100 $^{\circ}\text{C}$ was longer than 48 h (Wittayakun et al., 2008). Thus the synthesis conditions such as aging and

crystallization time that facilitated the transformation of NaY to NaP were further investigated.

This chapter includes the transformation of zeolite NaY, synthesized with the RHS as reported previously, to NaP at different aging times (1, 2, and 3 days) and crystallization times (1, 2, 3, 4, and 5 days). The product from each condition was characterized by X-ray diffraction (XRD). The sample with the highest degree of transformation was characterized further by fourier transform infrared spectroscopy (FTIR), scanning electron microscopy (SEM), laser diffraction particle size analyzer (DPSA) and thermal gravimetry analysis (TGA).

3.2 Experimental

3.2.1 Materials

Chemicals for the preparation of the RHS and zeolite synthesis were hydrochloric acid (37% HCl, Carlo-Erba), sodium aluminate (~55-56% of NaAlO₂, Riedel-de Haën), sodium hydroxide (97% NaOH, Carlo-Erba), and rice husk (from the local rice mill in Lampang, Thailand). The standard zeolites were NaY with a Si/Al molar ratio 5.7 (JRC with Tosoh Corp) and NaP (Fluka).

The RHS was prepared by the acid-leaching method reported previously (Khemthong et al., 2007). Briefly, the rice husk was washed and dried at 100°C overnight; refluxed with 3 M HCl for 6 h; filtered and washed again with water until pH of the filtrate was neutral and dried at 100°C overnight before pyrolysis in a muffle furnace (Carbolite, CWF1200) at 550°C for 6 h to remove hydrocarbon and volatile organic compounds. The obtained RHS contains amorphous silica with

approximately 98 wt% purity. This RHS was dissolved in 3.5 M NaOH solution to produce Na_2SiO_3 for further zeolite synthesis.

3.2.2 Synthesis of zeolite

The transformation was investigated with the synthesis gel of zeolite NaY prepared similarly to that in a previous work by Wittayakun et al. (2008) by mixing a seed gel and feedstock gel. The seed gel was prepared by dissolving NaOH and NaAlO_2 in deionized water followed by the addition of Na_2SiO_3 solution and kept at room temperature for 1 day. The feedstock gel was prepared in a similar method to that of the seed gel except that it was used immediately without aging. In the synthesis, both gels were mixed to form overall gel, aged (kept undisturbed) at room temperature, and crystallized at 100°C . After the crystallization step, the resulting white powder was separated by filtration, washed, and dried at 100°C .

The transformation of zeolite NaY to NaP was investigated by changing the aging time or crystallization time. In the first set, the overall gel was aged at various times (1, 2, and 3 days) and crystallized for 1 day. These conditions were chosen because the aging time of 1 day and the crystallization of 1 day was the optimum condition for the synthesis of NaY (Wittayakun et al., 2008). Another set of the experiment, the effect of crystallization time was investigated by fixing the aging time at 1 day and varying the crystallization time to 1, 2, 3, 4, and 5 days.

3.2.3 Characterization of the synthesized zeolites

The product from each condition was characterized by XRD (Bruker) with nickel filtered Cu K_α radiation scanning from 4 to 50° . The XRD pattern was compared with that of standard NaY and NaP.

A product with the highest degree of transformation was characterized further by FTIR (Spectrum GX, Perkin-Elmer) using KBr as a medium. IR spectra were scanned in the range of $4,000\text{ cm}^{-1}$ to 400 cm^{-1} with a resolution of 4 cm^{-1} .

Morphology of the zeolite was investigated by SEM (JEOL JSM-6400) with applied potential 10 - 20 kV.

Particle size distribution of zeolites was determined by DPSA (Malvern Instruments, Mastersizer 2000) with the sample dispersed in distilled water and analyzed by He-Ne laser. The standard volume percentiles at 10, 50, and 90, or denoted as $d(0.1)$, $d(0.5)$, and $d(0.9)$, respectively, were recorded from the analysis and used to calculate the width of the distribution. The width was calculated from the equation below:

$$\frac{d(0.9) - d(0.1)}{d(0.5)}$$

Thermal stabilities were investigated by TGA-DTA (TA Instrument/SDT 2960) by heating from 0°C to $1,000^{\circ}\text{C}$ with a heating rate of $10^{\circ}\text{C}/\text{min}$ in nitrogen flow ($100\text{ ml}/\text{min}$).

3.3 Results and discussion

3.3.1 Effect of aging time on transformation of NaY to NaP

The XRD patterns of the sample prepared at aging time of 1, 2, and 3 days were compared with that of NaY and NaP standards as shown in Figure 3.1. The spectrum of the 1-day aging sample was similar to that of standard zeolite Y without any other peaks, indicating that the pure phase of NaY was obtained. With increased aging time, the peaks at $2\theta = 12.5$, 21.6 , and 28.1 degree with low intensity emerged

in the products from 2- and 3-day aging times. The positions of those extra peaks were the characteristic peaks of NaP, indicating that a longer aging time than 1 day causes the transformation of NaY to NaP. The transformation was not significant at these conditions. It was found in the next section that the transformation occurred faster at a higher temperature.

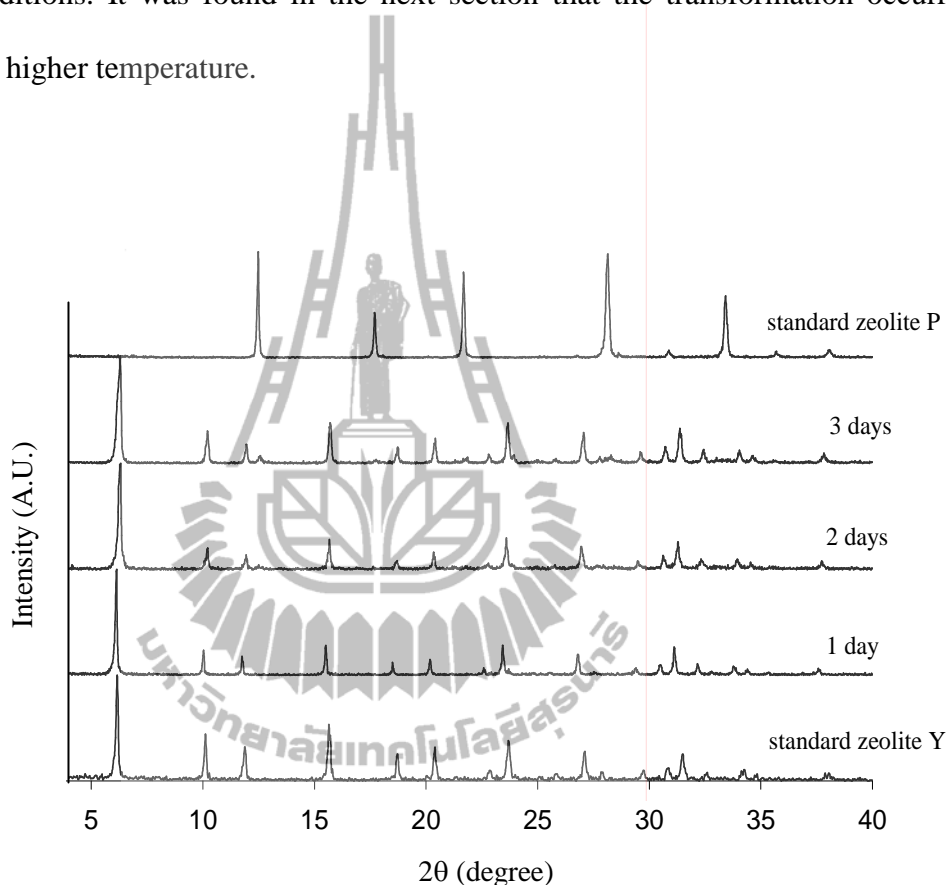


Figure 3.1 Normalized XRD patterns of zeolite synthesized with different aging times compared with the patterns of standard zeolite Y and zeolite P.

3.3.2 Effect of crystallization time on the transformation of NaY to NaP

The effect of crystallization time on the transformation of NaY to NaP was investigated with the aging time of 1 day because it showed no effect on the transformation. The XRD patterns of the products with a crystallization time from 1

to 5 days are displayed in Figure 3.2 along with that of standard zeolites. Only the sample with the 1-day crystallization time showed the pure phase of NaY with the 3- strongest peaks at $2\theta = 6.5, 15.6,$ and 23.7 degree. These 3 peaks had the same positions as those of zeolite Y reported in JCPDS files (International Centre for Diffraction Data, 1979).

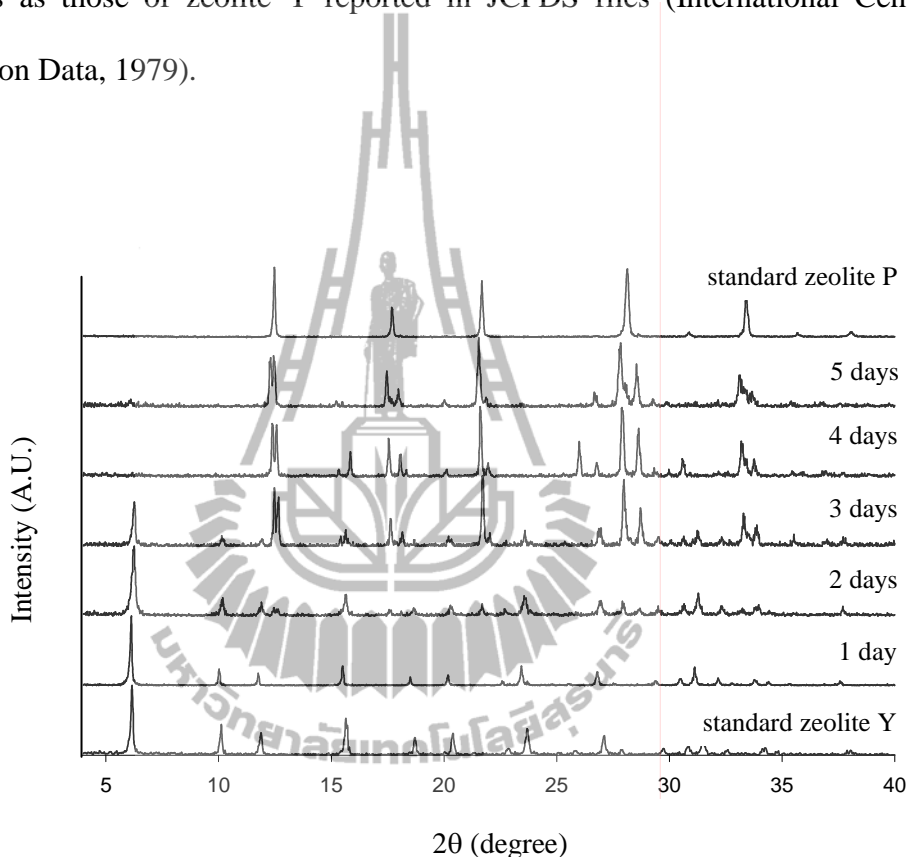


Figure 3.2 Normalized XRD patterns of zeolite synthesized with different crystallization times compared with the patterns of standard zeolite Y and zeolite P.

Characteristic peaks of NaP started to emerge in the sample with the 2-day crystallization time and the intensities of those peaks increased with a longer crystallization time. The main peak of NaY was not observed after crystallization for 4 days and NaP became a major component. Because there was another phase along with NaP, this condition was not suitable for the synthesis of zeolite P.

The first peak of NaP ($2\theta = 12.5$) from this study split into 2 peaks but the position was similar to that of the standard NaP and the peaks of zeolite P from JCPDS database (International Centre for Diffraction Data, 1979). It was possible that there were two types of NaP in this sample and this was confirmed by SEM in the next section. From the literature, the position of this peak of NaP with different morphology was slightly different (within 0.5 degree) (Sathupunya et al., 2002 and Zubowa et al., 2008).

3.3.3 Characterization of product with 5-day crystallization

The product obtained after the 5-day crystallization time contained NaP as a major component. It was further characterized by FTIR, SEM, DPSA, and TGA-DTA.

The FTIR spectrum in transmittance mode in Figure 3.3 shows peaks at 3487, 1638, 1002, 773, 690, 571, and 465 cm^{-1} . These peaks were similar to those of zeolite P reported by Flanigen et al. (1971). The peaks at 571-460 cm^{-1} and 1002 cm^{-1} were assigned to T-O (T = Si, Al) bending and Si-O, Al-O tetrahedral vibration, respectively. The appearance of the peaks at 690, 1638, and 3487 cm^{-1} was attributed to the double ring external linkage, vibration of water molecule, and OH stretching, respectively (Albert et al., 1998).

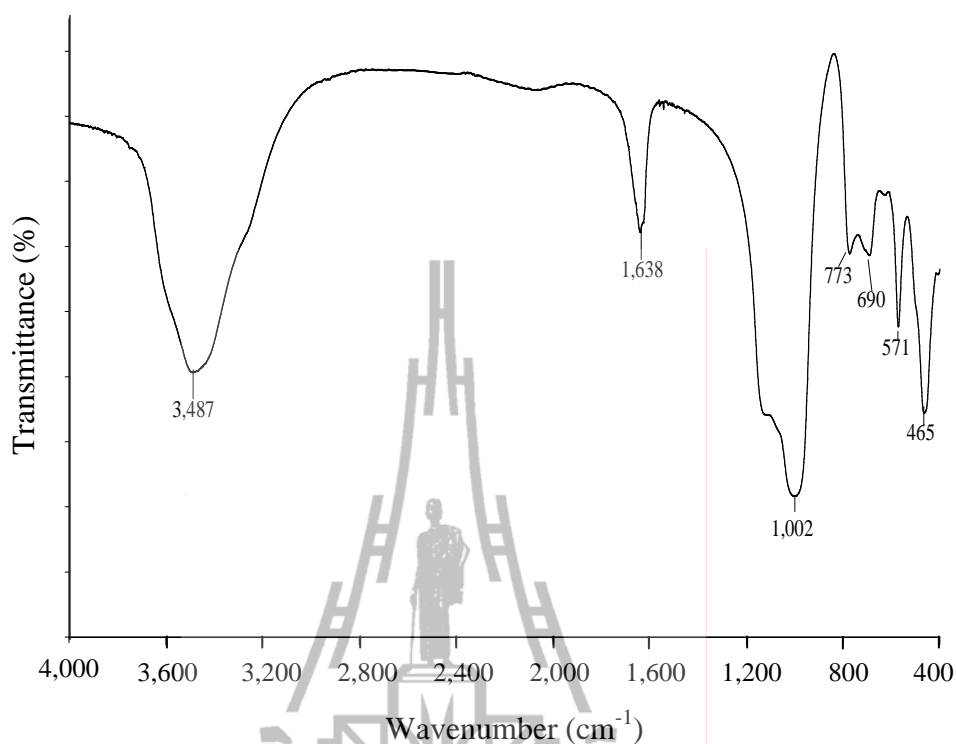


Figure 3.3 FTIR spectrum of product obtained from 1-day aging and 5-day crystallization time.

The SEM micrograph in Figure 3.4 illustrates the morphology of the product from the crystallization of 5 days. There were two types of particles: spherical and multifaceted. The spherical shape was similar to that of NaP reported by Sathupunya et al. (2002) and the multifaceted shape was similar to that of NaP reported by Zubowa et al. (2008). The mixed morphology might be the reason that the XRD peak at $2\theta = 12.5$ degree (Figure 3.2) split into 2 peaks.

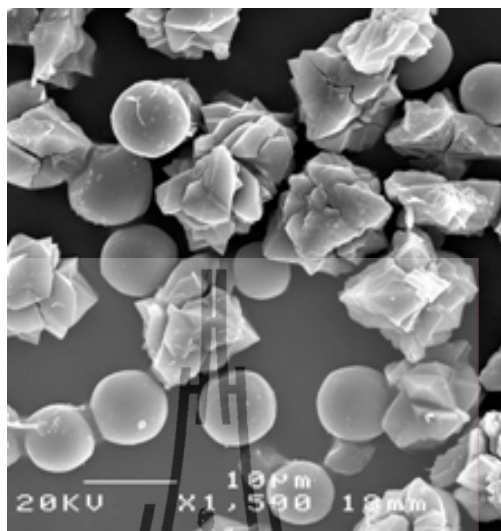


Figure 3.4 SEM image of product obtained from 1-day aging and 5-day crystallization time.

Particle size distribution of the product with the 5-day crystallization time obtained from the DPSA is shown in Figure 3.5. The major population had a particle size in the range of 4-25 μm with a small population with a size in the range of 0.7-3.0 μm . Note that the particle sizes from the DPSA were the size and distribution of bulk particles which might be composed of several small particles aggregated together, and thus were different from the results from the SEM which displayed images of isolate crystals.

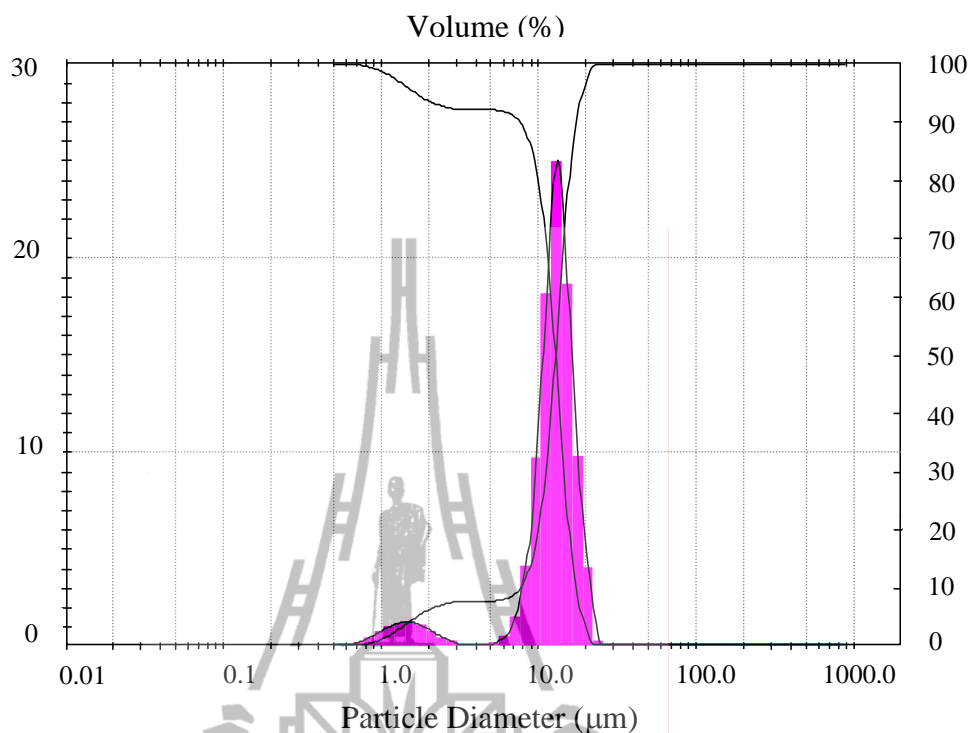


Figure 3.5 Particle size distribution of product obtained from 1-day aging and 5-day crystallization time.

The thermal stability of the product with the 5-day crystallization time obtained from the TGA-DTA experiment is shown in Figure 3.6. The weight loss during heating was approximately 17% up to 400°C, accompanied by 3 endothermic peaks at about 60, 100, and 150°C which was attributed to the loss of water (Zubowa et al., 2008). Further weak endothermic peaks were observed at about 200, 300, and 600°C. These 3 peaks resulted from a 3-step endothermic water loss and, at 900°C at which the zeolite P was irreversibly converted into nepheline, a dense $\text{NaAlSi}_3\text{O}_8$ phase (Albert et al., 1998).

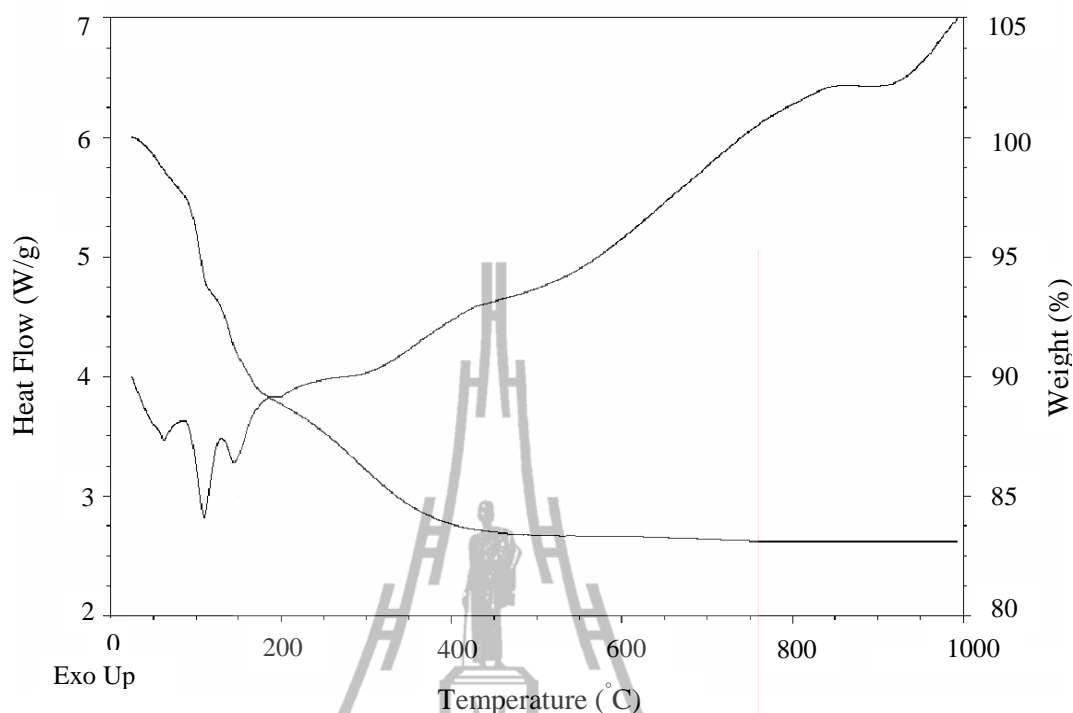


Figure 3.6 TGA-DTA thermogram of product obtained from 1-day aging and 5-day crystallization time.

3.4 Conclusions

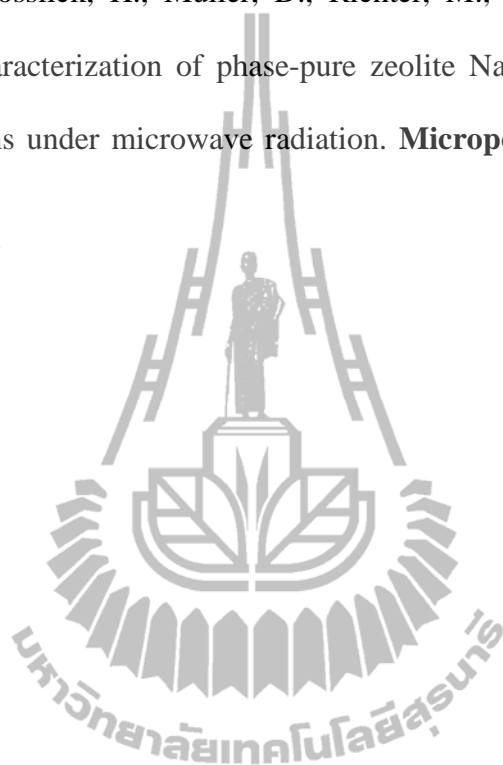
Two parameters that affected the transformation of zeolite NaY to zeolite NaP were the aging time and crystallization time. When the crystallization time was fixed at 1 day, the aging time of 1 day was suitable to produce the pure phase of zeolite NaY whereas 2 and 3 days aging times produced a small amount of NaP. The crystallization time showed a more significant effect on the transformation. The phase of NaY was not observed after crystallization for 4 days and, after a crystallization time of 5 days, NaP was a major product. With the 5-day crystallization time, NaP was a major product with a trace amount of NaY.

3.5 References

- Albert, B. R., Cheetham, A. K., Stuart, J. A., and Adams, C. J. (1998). Investigation on P zeolites: synthesis, characterization and structure of highly crystalline low-silica NaP. **Micropor. Mesopor. Mater.** 21: 133-142.
- Flanigen, E. M., Khatami, H., and Szymanski, H. A. (1971). Molecular sieve zeolites. **Adv. Chem. Ser.** 101: 201-228.
- Huang, S., Jing, S., Wang, J., Wang, Z., and Jin, Y. (2001). White silica obtained from rice husk in fluidized propellant bed. **Powder Technol.** 117: 232-238.
- JCPDS International Centre for Diffraction Data. (1998). Powder Diffraction File. Pennsylvania.
- Khemthong, P., Prayoonpokarach, S., and Wittayakun, J. (2007). Synthesis and characterization of zeolite LSX from rice husk silica. **Suranaree J. Sci. Technol.** 12(4): 367-379.
- Murayama, N., Yamamoto, H., and Shibata, J. (2002). Mechanism of zeolite synthesis from fly ash by alkali hydrothermal reaction. **Int. J. Miner. Process.** 64: 1-17.
- Nery, J. G., Mascarenhas, Y. P., and Cheetham, A. K. (2003). A study of highly crystalline, low-silica, fully hydrated zeolite P ion exchanged with (Mn^{2+} , Cd^{2+} , Pb^{2+} , Sr^{2+} , Ba^{2+}) cations. **Micropor. Mesopor. Mater.** 57: 229-248.
- Sang, S., Liu, Z., Tian, P., Liu, Z., Qu, L., and Zhang, Y. (2006). Synthesis of small crystals zeolite NaY. **Mater. Lett.** 60: 1,131-1,133.
- Sathupunya, M., Gularib, E., and Wongkasemjit, S. (2002). ANA and GIS zeolite synthesis directly from alumatrane and silatrane by sol-gel process and microwave technique. **J. Eur. Ceram. Soc.** 22: 2,305-2,314.

Wittayakun, J., Khemthong, P., and Prayoonpokarach, S., (2008). Synthesis and characterization of zeolite NaY from rice husk silica. **Korean J. Chem. Eng.** 25(4): 861-864.

Zubowa, H. L., Kosslick, H., Muller, D., Richter, M., Wilde, L., and Fricke, R. (2008). Characterization of phase-pure zeolite NaP from MCM-22-type gel compositions under microwave radiation. **Micropor. Mesopor. Mater.** 109: 542-548.



CHAPTER IV

n-BUTANE HYDROGENOLYSIS OVER SUPPORTED COBALT CATALYSTS

Abstract

This chapter focuses on an investigation of the activity of cobalt catalysts supported on zeolite NaY and zeolite ZSM-5 in *n*-butane hydrogenolysis. The conversion in this reaction over cobalt supported on NaY was lower than that of cobalt supported on ZSM-5. Thus monometallic Co/ZSM-5 and bimetallic CoPd/ZSM-5 were further prepared and investigated. Cobalt contents in both mono- and bimetallic catalysts were 1, 4, 7, and 10 wt%, and the amount of palladium was fixed at 1 wt%. The catalysts were characterized by X-ray diffraction, extended X-ray absorption near edge structure (XANES) spectroscopy and N₂ adsorption-desorption; the catalysts with high cobalt content had low surface areas and high degrees of cobalt reduction. The presence of Pd in the bimetallic catalysts did not significantly increase the reducibility. The catalytic testing results on *n*-butane hydrogenolysis showed that activity of monometallic catalysts increased with the cobalt content, except the catalysts with 10 wt% cobalt and the addition of palladium did not significantly enhance the activity of catalysts. The conversion of *n*-butane per cobalt atom demonstrated that 7Co1Pd/ZSM-5 has the highest activity among the catalysts studied in this work.

4.1 Introduction

Oil refining processes produce large amounts of long-chain hydrocarbons (Leclercq et al., 1995) which are less economically interesting than small hydrocarbon molecules. Thus, reactions to convert long chain to small molecules are needed. Hydrogenolysis is a reaction which involves the breakage of carbon-carbon bonds with the uptake of hydrogen. It is also defined as a structure sensitive reaction because the selectivity and specific rate of alkane hydrogenolysis often depend on morphology and chemical properties of the catalysts (Boudart et al., 1969).

In supported catalysts, the properties of the metals have a great influence on the activity and selectivity in the hydrogenolysis reaction. The selectivity aspect for hydrogenolysis is represented by the fragmentation factor, which, by definition, characterizes the depth of hydrogenolysis as the number of fragmented molecules per molecule of feed split up. In single hydrogenolysis, only one C–C bond is cleaved and the fragmentation factor is one. In multiple hydrogenolysis, more than one C–C bond is broken and the fragmentation factor is more than one (Jackson et al., 1998).

Particle sizes of metal in supported catalysts can affect the activity and selectivity in alkane hydrogenolysis. For example, Yao et al. (1979) found that activity and selectivity for *n*-pentane hydrogenolysis on alumina-supported rhodium (Rh) was a function of particle size. The highly dispersed Rh catalysts produced ethane and propane selectively due to the selective cleavage of the C–C bond. In contrast, for the large particles, the cleavage of *n*-pentane became random. Furthermore, Maroto-Valiente et al. (2005) reported that the hydrogenolysis activity of *n*-butane on ruthenium supported on Al₂O₃ decreased with the metal particle size in the approximate range of 1-24 nm.

In this study, the activity of supported cobalt (Co) catalysts on *n*-butane hydrogenolysis was studied. Although Co has been reported to be a good catalyst for hydrogenolysis, only zerovalent cobalt (Co⁰) is an active form. Typically, the cobalt in supported catalysts is in oxide forms after the catalyst preparation is completed. Thus, the reduction process is required to transform the oxide to the zerovalent form.

To enhance the reducibility of cobalt oxide, a noble metal can be added as a promoter. The improvement could be explained by H₂ spillover effect in which dihydrogen molecules adsorb on the noble metal and diffuse to the adjacent cobalt oxide particle, and thus promote the reduction. A report from Xiong et al. (2009) demonstrated that the addition of ruthenium to Co/SBA-15 catalysts enhanced the reducibility of cobalt oxide. The ruthenium oxide was first reduced and subsequently catalyzed the reduction of cobalt oxide to the metallic form. Jacob et al. (2002) showed that the addition of 0.5 wt% Pt to 15 wt% Co supported on Al₂O₃ significantly reduced the reduction temperature of surface cobalt oxide species. By comparing results from temperature programmed reduction (TPR) between Pt-promoted Co/Al₂O₃ and unpromoted catalysts, it was shown that the addition of Pt caused the reduction peaks to shift markedly to lower temperatures, presumably due to spillover of H₂ from the noble metal to reduce the cobalt oxide. According to Al-Saleh et al. (2003), platinum and rhodium were also used to introduce H₂ spillover on Co on highly porous saponite (HPS). TPR studies showed that Pt–Rh combination had more significant effects on the reducibility of Co species on HPS than the unpromoted one and single noble metal (Pt, Rh individually)-promoted catalysts. The Pt–Rh combination shifted the TPR peaks to lower temperatures. Moreover, a report from Khemthong et al. (2010) revealed that the addition of 1.0 wt% Pt to 1 wt%,

6 wt% and 10 wt% Co supported on zeolite NaY enhanced the reducibility of cobalt oxide particle by the H₂ spillover effect.

In this chapter, supported cobalt catalysts were prepared by using zeolite NaY and NaZSM-5 as supports, because they were reported to be good cracking catalysts (Danuthai et al., 2009; Karge et al., 1991). A small amount of palladium was added to improve the cobalt reducibility. The activity of supported metal catalysts were tested for *n*-butane hydrogenolysis reaction. Moreover, the activity of cobalt catalysts supported on NaZSM-5 with various cobalt contents were investigated.

4.2 Experimental

4.2.1 Synthesis of zeolite NaY

Zeolite NaY was synthesized from seed gel and feedstock gel by the procedure described in Chapter III. The seed gel was prepared by dissolving NaOH and NaAlO₂ in deionized water followed by addition of Na₂SiO₃ solution and kept at room temperature for 1 day. The feedstock gel was prepared by a method similar to that of the seed gel except that it was used immediately. Both gels were mixed together to form overall gel, aged (kept undisturbed) at room temperature for 24 h and crystallized at 100 °C for another 24 h. The zeolite product was separated by centrifugation and characterized by XRD.

4.2.2 Synthesis of zeolite ZSM-5

Zeolite NaZSM-5 was synthesized with a procedure adapted from literature (Panpa and Jinawath, 2009). About 6.00 g of rice husk SiO₂, was dissolved in NaOH solution to become Na₂SiO₃ solution, while 1.5 g of tetrapropyl ammonium bromide (TPABr) and NaAlO₃ were dissolved in deionized water and NaOH solution,

respectively. The TPABr solution and NaAlO₃ solution were first mixed together and further mixed with the Na₂SiO₃ solution. The pH of the mixture was adjusted to 11 by 1 M HNO₃ and the mixture was crystallized in an autoclave at 150°C for 48 h. The solid product was separated by centrifugation, calcined at 550°C for 5 h to remove the template and characterized by XRD.

4.2.3 Preparation of cobalt catalysts

4.2.3.1 Monometallic cobalt catalysts

The monometallic cobalt catalysts were prepared by incipient wetness impregnation of Co(NO₃)₂·6H₂O aqueous solution to zeolite NaZSM-5. The samples were dried at room temperature for 24 h, and at 100°C for 3 h before calcination at 300°C for 3 h with 2°C/min heating rate. The cobalt content in samples prepared from zeolite ZSM-5 were 1, 4, 7, and 10 wt%, and the samples were denoted as 1Co/ZSM-5, 4Co/ZSM-5, 7Co/ZSM-5 and 10Co/ZSM-5, respectively.

4.2.3.2 Bimetallic cobalt catalysts

The bimetallic cobalt catalysts were synthesized by incipient wetness impregnation of Pd(CH₃COO)₂ (98%, Aldrich Chem) in NH₃ solution (25% Fisher Chemicals) into the monometallic cobalt catalysts. The amount of Pd(CH₃COO)₂ was fixed to give 1.0 wt% Pd. The samples were dried at room temperature for 24 h, then 3 h at 100°C before calcination in air at 400°C for 3 h with 2°C/min heating rate. The bimetallic samples with 1, 4, 7 and 10 wt% Co and 1 wt% Pd were denoted as 1Co1Pd/ZSM-5, 4Co1Pd/ZSM-5, 7Co1Pd/ZSM-5, and 10Co1Pd/ZSM-5, respectively. The cobalt supported on zeolite NaY was also prepared in a similar method. The metal containing in this sample were 7 wt% cobalt and 1 wt% Pd and it was denoted as 7Co1Pd/NaY.

4.2.4 Catalyst characterization

4.2.4.1 X-ray diffraction spectroscopy (XRD)

The crystalline phase of NaZSM-5 and NaY were confirmed by X-ray diffraction using Cu K α radiation. The scanning range is 5-50° for zeolites and 5-80° for supported cobalt catalysts with a step size of 0.02 degree and scan speed of 0.5 degree/s.

4.2.4.2 X-ray absorption near edge structure (XANES)

XANES spectra of monometallic and bimetallic samples were recorded in a transmission mode at the Beamline 8 of the Synchrotron Light Research Institute, Thailand. The storage ring was operated with the electron energy of 1.2 GeV and electron current between 90 and 140 mA. The beam was monochromatized using a Ge (220) double crystal, and the Co K-edge at 7709 eV was calibrated by using Co foil. The samples were prepared by treatment in He at 150°C for 1 h and reduced in H₂ at 400°C for 5 h. The reduced samples were pressed to form a pellet with a hydraulic pressure of 10 tons for 30 seconds.

The pellet was then sealed by using Kapton tape and attached to the sample holder. The spectra of samples and standard materials were collected in transmission mode at room temperature using an ionization chamber as a detector. Three scans of XANES spectra were acquired and averaged for each sample before the data analysis. Data reduction process and linear combination fitting were performed by using Athena program (Ravel and Neville, 2005).

4.2.4.3 N₂ adsorption-desorption

The prepared catalysts were dried at 100°C overnight before analyzing by N₂ adsorption-desorption method. The adsorption-desorption isotherm was

obtained by a Micromeritics ASAP 2010 Autosorb-1 series. Surface area of each sample was determined by using Brunauer-Emmett-Teller (BET) method.

4.2.5 Catalytic testing

The catalytic performance of all cobalt catalysts for *n*-butane hydrogenolysis was investigated in a fixed-bed flow reactor. The catalyst powder was pressed by a hydraulic press (Carver[®], Carver INC., USA) and sieved to the size of 250-425 μm . Approximately, 0.05 g of catalyst was mixed with 0.3 g $\alpha\text{-Al}_2\text{O}_3$ and packed in a quartz wool bed in a 6 mm diameter quartz tube. The catalyst was treated in He (TSG, 99.995% purity) (50 ml/min) at 150°C for 1 h. The temperature was ramped up to 400°C (10°C /min) in H₂ (TSG, 99.999%) and maintained at this temperature for 5 h.

Once the reduction process was completed, the catalyst was cooled down to the reaction temperature in flowing He and the reactant gases He: H₂: *n*-butane in a mass ratio of 69.5: 30: 0.5 ml/min were fed through the reactor. The catalytic testing was conducted from 200 to 410°C. The gas outlet was analyzed every 30°C by a gas chromatograph (SRI-GC-310C) equipped with a thermal conductivity detector (TCD).

4.3 Results and discussion

4.3.1 Effect of support

To compare effects of the support on the catalytic activity, catalysts containing 7 wt% Co and 1 wt% Pd supported on ZSM-5 and NaY were prepared, characterized and tested for *n*-butane hydrogenolysis.

4.3.1.1 Characterization of 7Co1Pd/ZSM-5 and 7Co1Pd/NaY

XRD spectroscopy

The XRD patterns of 7Co1Pd/NaY and 7Co1Pd/ZSM-5 are shown in Figure 4.1. The XRD pattern of 7Co1Pd/NaY shows characteristic peaks of NaY at $2\theta = 6.16, 10.08, 11.82, 15.54, 18.58, 20.14, 23.44, 26.78,$ and 31.12 degree (Wittayakun et al., 2008). The characteristic peaks of Co_3O_4 were observed at $2\theta = 36.76, 54.84,$ and 63.96 degree (Jiang et al., 2002). The XRD pattern of 7Co1Pd/ZSM-5 shows peaks attributed to ZSM-5 at $2\theta = 7.84, 8.72, 22.97,$ and 23.84 degree (Panpa and Jinawath, 2009) and peaks correspond to Co_3O_4 at $2\theta = 36.76, 54.84,$ and 63.96 degree. The presence of the XRD peaks of zeolite in both samples indicated that addition of cobalt and palladium did not change the zeolite structure. The characteristic peaks of CoO were not observed in the diffraction pattern of either samples. However, the presence of peaks due to Co_3O_4 suggested that cobalt nitrate precursor decomposed during the calcinations and converted to Co_3O_4 . The Co_3O_4 is the typical species observed in cobalt supported on metal oxide samples. For example, the XRD pattern of cobalt supported on ZrO_2 after calcination, shows peaks due to Co_3O_4 as well as the peaks of support (Yung et al., 2007).

The XRD pattern of 7Co1Pd/NaY shows Co_3O_4 peaks with lower intensity than that of 7Co1Pd/ZSM-5. This result preliminarily suggests that cobalt

species in 7Co1Pd/NaY are better dispersed than in 7Co1Pd/ZSM-5. The peaks corresponding to PdO were not observed in either sample probably because both samples contain low Pd loadings which results in good dispersions.

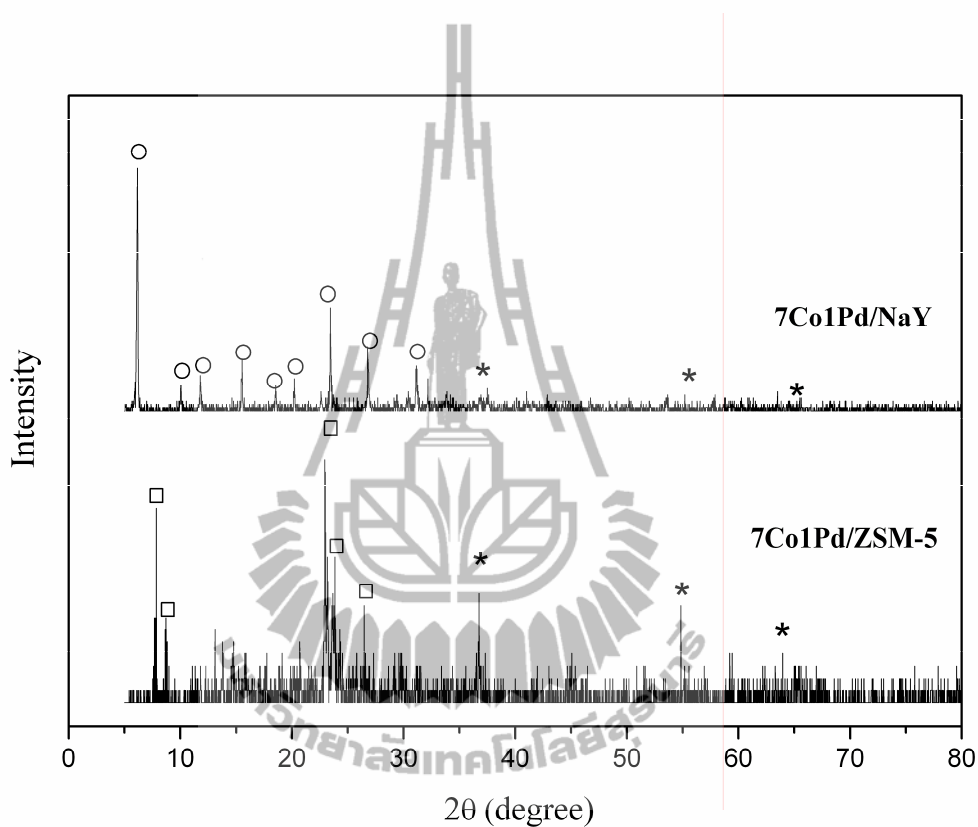


Figure 4.1 XRD patterns of 7Co1Pd/ZSM-5 and 7Co1Pd/NaY; o, peaks corresponded to zeolite NaY, □, peaks corresponded to zeolite ZSM-5 and, *, peaks corresponded to Co_3O_4 .

XANES of reduced samples

The XANES spectra of both samples after reduction at 400°C for 5 h were compared to those of reference materials (Figure 4.2).

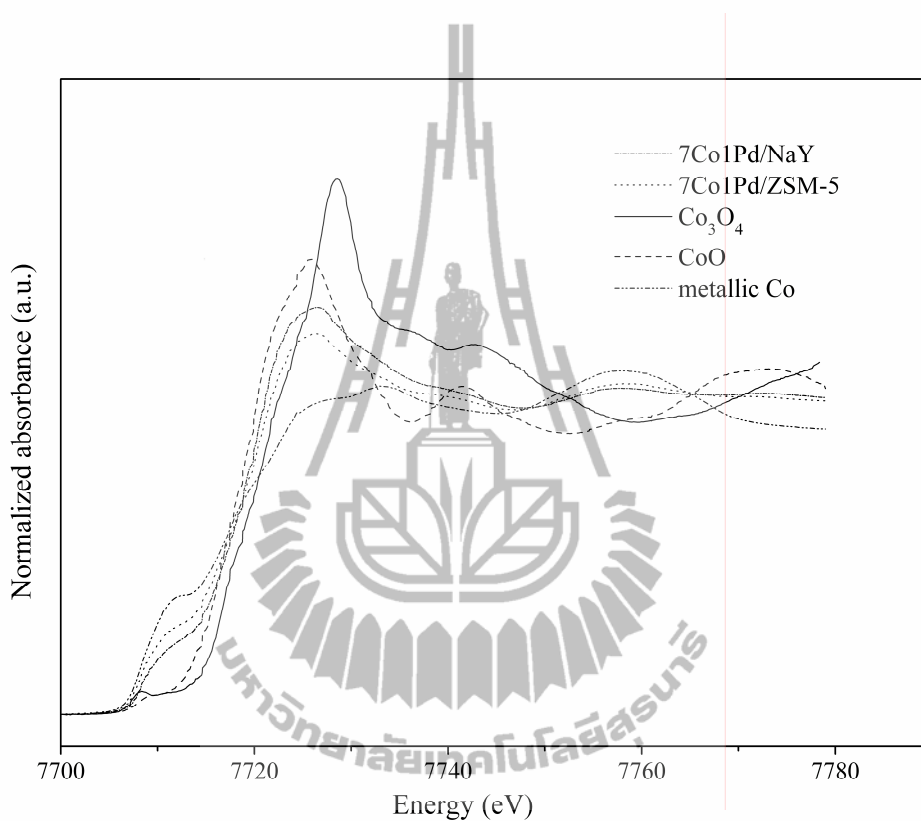


Figure 4.2 Normalized XANES spectra of 7Co1Pd/NaY and 7Co1Pd/ZSM-5 compared to the standard materials.

The shift in cobalt edge of the sample from that of the standard metallic cobalt is related to its oxidation state. Namely, if cobalt oxide is reduced, the cobalt K-edge shifts to lower energy. A white line, sharp peak in XANES spectrum, is a characteristic of cobalt in cationic form as can be observed in the spectra of CoO and Co₃O₄ standards. The white line in spectrum of 7Co1Pd/ZSM-5 has lower intensity than that of 7Co1Pd/NaY. It is preliminarily suggested that the cobalt

species in 7Co1Pd/ZSM-5 was reduced more than that in 7Co1Pd/NaY. Another important feature of XANES spectra is the pre-edge, which is a small peak before the sharp rise of the edge. Pre-edge feature associated with the symmetry effects in the environment of cobalt and $1s \rightarrow 3d$ transition (Jacobs et al., 2007). As described by Moen et al. (1997), the transition is most intense when the first coordination shell lacks inversion symmetry. Therefore, the pre-edge feature is most intense for tetrahedral symmetry but should not be presented for octahedral symmetry. In practice, a very weak pre-edge feature could be observed in a distorted octahedral symmetry. For Co_3O_4 , a spinel structure with one-third of the cobalt is +2 oxidation state and occupied tetrahedral site and two-thirds is +3 oxidation state and occupied octahedral site. Thus the pre-edge feature represents a combination of more intense tetrahedral and less intense octahedral peak. On the other hand, cobalt in CoO has octahedral symmetry; therefore the pre-edge feature is not permitted. In Figure 4.2 the XANES spectrum of Co_3O_4 shows pre-edge feature at about 7709 eV and it was also observed in the spectrum of CoO, but much less intense. However, the pre-edge feature was not observed in the spectrum of metallic cobalt. The spectra of 7Co1Pd/NaY and 7Co1Pd/ZSM-5 show features that lies between the pre-edge of cobalt oxide and metallic cobalt, suggesting that some fractions of cobalt in each sample were transformed to metallic cobalt. The fraction of metallic cobalt was further determined by linear combination fitting.

Linear combination fitting was performed by using XANES spectra of CoO, Co_3O_4 , and metallic cobalt as references. The fraction of each reference in the samples was estimated, and the fitting results of both samples are shown in Figure 4.3 and 4.4. The Co_3O_4 and CoO were used as reference materials in this fitting because

CoO is an intermediate species of the reduction process of Co_3O_4 to metallic cobalt as shown in the TPR of Co_3O_4 (Tang et al., 2008).

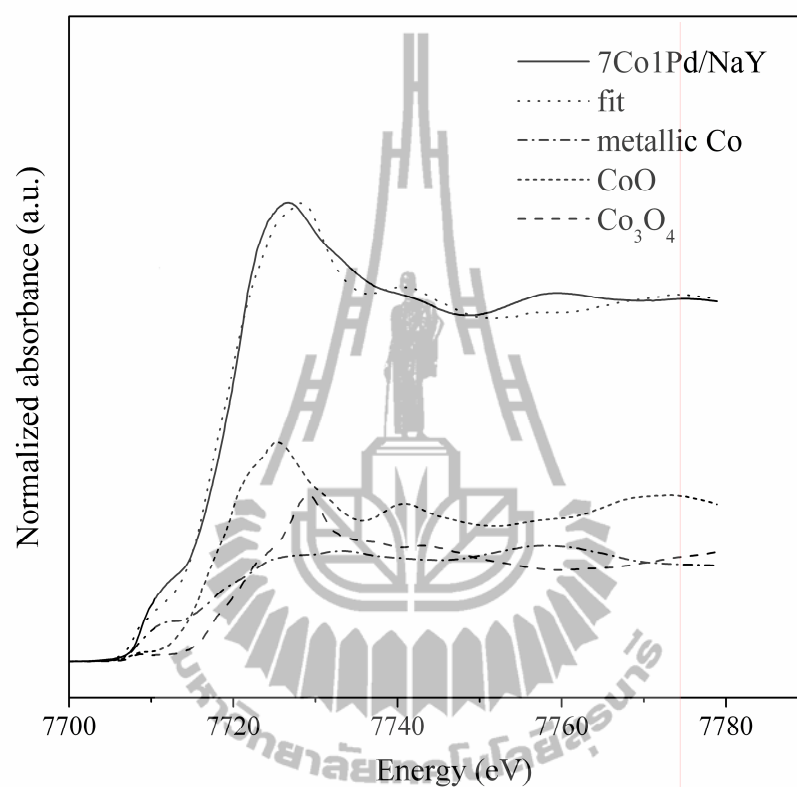


Figure 4.3 Linear combination fit of 7Co1Pd/NaY after reduction at 400°C for 5 h.

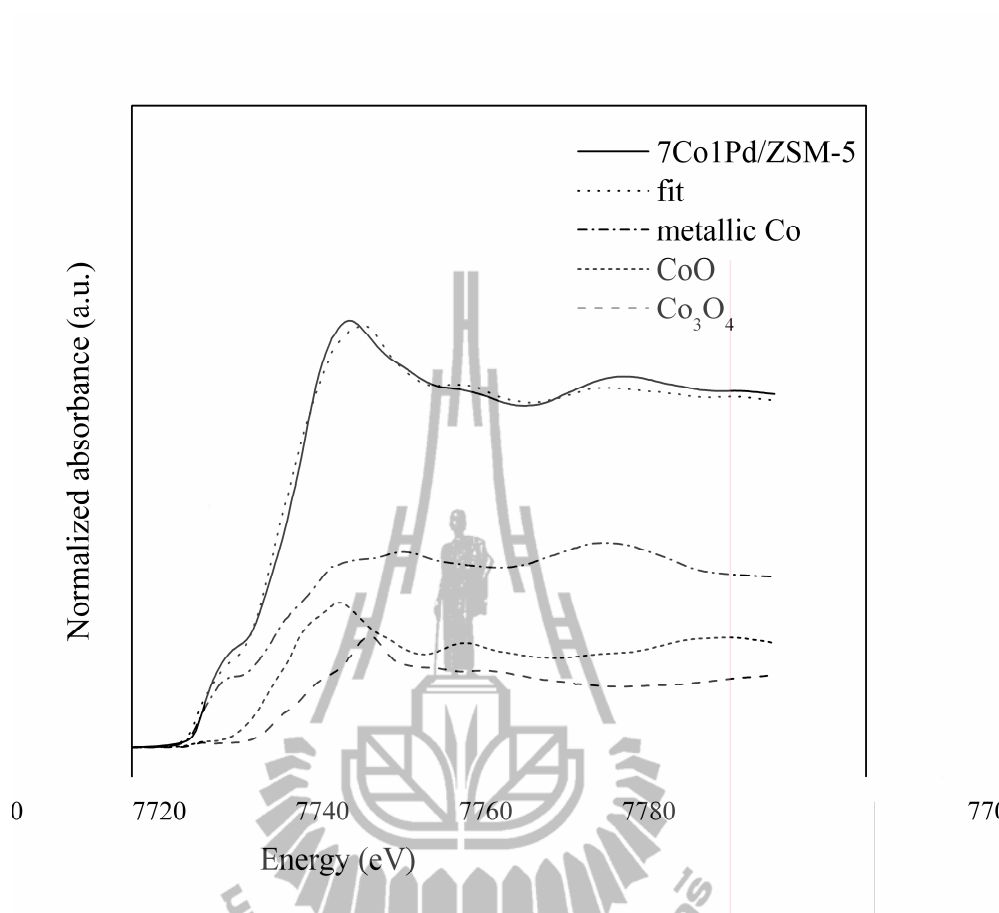


Figure 4.4 Linear combination fit of 7Co1Pd/ZSM-5 after reduction at 400°C for 5 h.

Fraction of Co species from linear combination fitting are shown in Table 4.1. Both samples consisted of Co₃O₄, CoO, and metallic cobalt. The fraction of metallic cobalt observed in 7Co1Pd/ZSM-5 was higher than that of 7Co1Pd/NaY, demonstrating that the catalyst supported on ZSM-5 was reduced more easily than that supported on NaY.

Table 4.1 Fraction of cobalt species in samples after reduction in H₂ at 400 °C for 5 h.

Samples	Fraction		
	Co foil	CoO	Co ₃ O ₄
7Co1Pd/NaY	0.298	0.425	0.277
7Co1Pd/ZSM-5	0.532	0.284	0.185

According to the XRD patterns of both samples, the peaks attributed to Co₃O₄ particles in the diffraction pattern of 7Co1Pd/ZSM-5 had higher intensity than that of 7Co1Pd/NaY, suggesting that the Co₃O₄ particles in 7Co1Pd/ZSM-5 are larger than those of 7Co1Pd/NaY. The size of oxide particle plays a key role in the reducibility. Pârvolescu et al. (1998) reported that the big cobalt oxide particle was reduced more easily than the small particle due to its weakened metal surface interaction.

4.3.2 Catalytic testing results

The activities for *n*-butane hydrogenolysis of 7Co1Pd/NaY and 7Co1Pd/ZSM-5 are shown in Figure 4.5. The conversion observed with each catalyst increased in accordance with temperature. For 7Co1Pd/ZSM-5, the conversion reached 100% at 320 °C and it tends to be stable until 400 °C. For 7Co1Pd/NaY, the conversion was gradually increased with temperature and it was only 60% at 400 °C. These results indicated that the catalyst supported on ZSM-5 had higher conversion than catalyst supported on NaY. Since only metallic cobalt is active for the hydrogenolysis reaction (Chu et al., 2007), the conversions of both samples agree with the fraction of metallic cobalt determined by linear combination fitting. The difference of metal dispersion over both supports might be explained by difference in acid sites of NaY and ZSM-5. Since NaY contains more acid sites than ZSM-5 (Morales-Pacheco et al., 2011), the

interaction between cobalt oxide and surface of NaY might be stronger than that on ZSM-5, as a result of stronger metal-support interaction and small oxide particle.

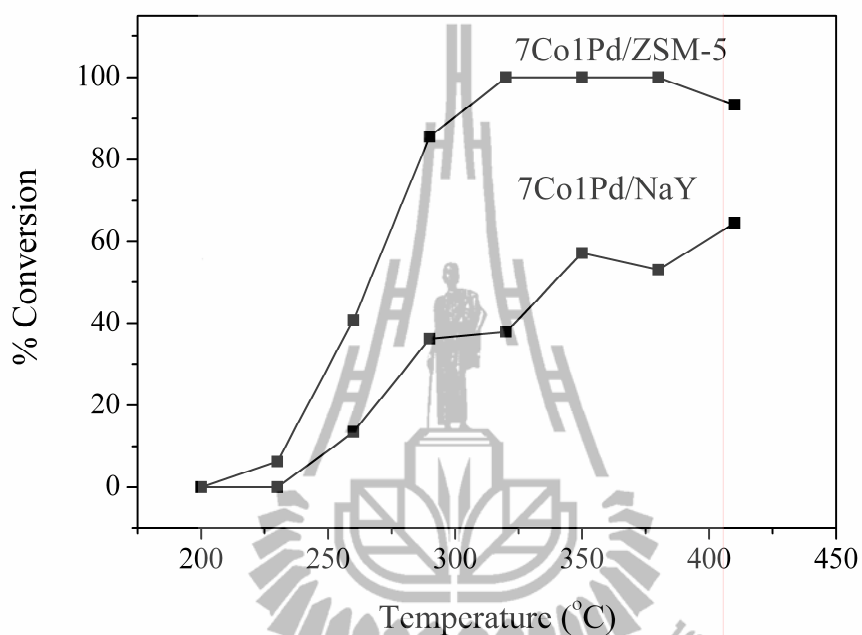


Figure 4.5 Conversion of *n*-butane on 7Co1Pd/NaY and 7Co1Pd/ZSM-5.

Reactant gases included He: H₂: *n*-butane in a mass ratio of 69.5: 30: 0.5 ml/min.

The activity of *n*-butane hydrogenolysis over 7Co1Pd/NaY was lower than that of 7Co1Pd/ZSM-5. The activity of supported cobalt catalysts with different metal loadings was further investigated by using ZSM-5 as a support. The catalysts studied in this work include mono- and bimetallic cobalt catalysts.

4.3.3 XRD spectroscopy characterizing supported cobalt catalysts on ZSM-5

The XRD patterns of catalysts including mono- and bimetallic cobalt present 2 θ peaks of ZSM-5 at 7.84, 8.72, 22.97, and 23.84 degree as shown in Figure 4.6, indicating that the structure of zeolite did not change during the catalyst preparation.

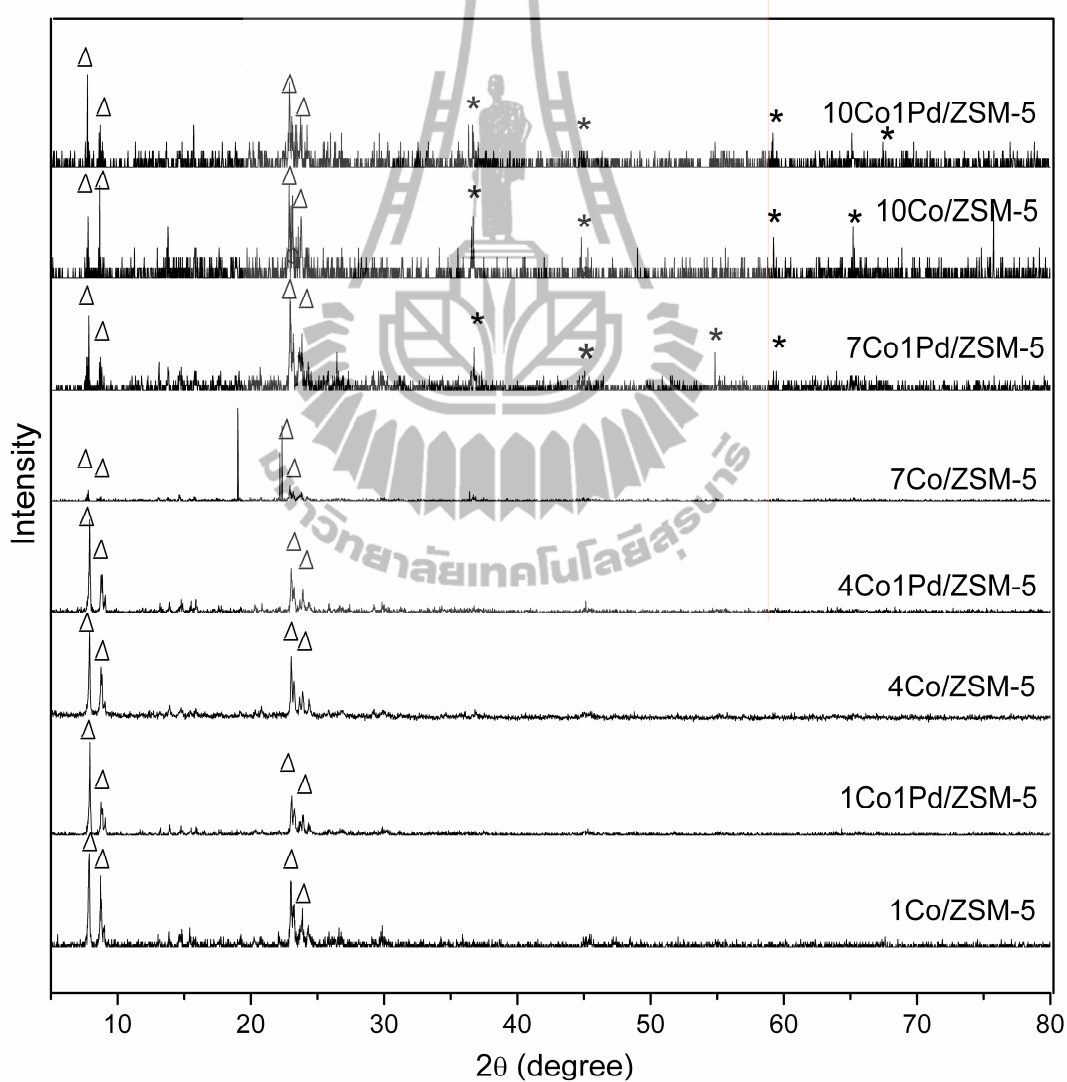


Figure 4.6 XRD patterns of mono- and bimetallic cobalt catalysts; Δ , peaks corresponded to ZSM-5 framework and, *, peaks corresponded to Co_3O_4 .

The peaks of CoO were not observed in all samples. On the other hand, the catalysts with cobalt loading at least 7 wt% showed peaks of Co_3O_4 at $2\theta = 36.76$, 54.84 , and 63.96 degree, similar to the XRD patterns of 7Co1Pd/ZSM-5 and 7Co1Pd/NaY previously mentioned. The absence of Co_3O_4 peaks for XRD pattern of catalysts with lower cobalt loading might be a result of smaller Co_3O_4 particles.

4.3.4 N_2 adsorption-desorption characterizing supported cobalt catalysts on ZSM-5

The adsorption isotherms of mono- and bimetallic cobalt catalysts on ZSM-5 are presented in Appendix B. All isotherms are type II which indicate that all samples are microporous materials. The adsorbed volume increased quickly at low pressure, illustrating that the samples contain narrow pore. The BET surface area and micropore volume of the as-prepared samples are shown in Table 4.2, Figure 4.7 and Figure 4.8. For monometallic cobalt catalysts, the surface area was remarkably decreased when the cobalt content increased from 1 wt% to 4 wt% but slightly decrease in 7Co/ZSM-5 and 10Co/ZSM-5. The decreasing in surface area was observed together with the decreasing in micropore volume. Thus, this phenomenon possibly occurred from partial blockage of zeolite pore by metal.

Considering catalysts with the same cobalt content, addition of 1 wt% Pd to monometallic cobalt catalyst slightly increased its surface area (Table 4.2). However, the surface area of bimetallic cobalt catalyst was not significantly higher than that of monometallic catalyst. A small increasing in surface area could be a result from the higher cobalt dispersion when adding palladium into catalyst. This effect also found in the addition of Pd into Co/SiO₂ sample reported by Sun et al. (2002). Moreover, there was a report indicated that addition of trace amount of Pd into Co-saponite

catalysts improved the cobalt dispersion (Hossain, 2006). The metal with high melting point and low surface mobility such as Rh, Pt and Pd should retain high dispersion over metal oxide because a strong metal-support interaction (Sault, 1995). Thus, the strong Pd-support interaction could be the reason for enhancing metal dispersion of cobalt in this work.

Table 4.2 BET surface area of mono- and bimetallic cobalt supported on ZSM-5.

Catalyst	BET surface area (m ² /g)	Micropore volume (cm ³ /g)
ZSM-5	332.03	0.1057
1Co/ZSM-5	344.82	0.0964
4Co/ZSM-5	287.24	0.0885
7Co/ZSM-5	268.76	0.0829
10Co/ZSM-5	266.65	0.0814
1Co1Pd/ZSM-5	342.18	0.1057
4Co1Pd/ZSM-5	326.71	0.1038
7Co1Pd/ZSM-5	288.81	0.0854
10Co1Pd/ZSM-5	271.19	0.0835

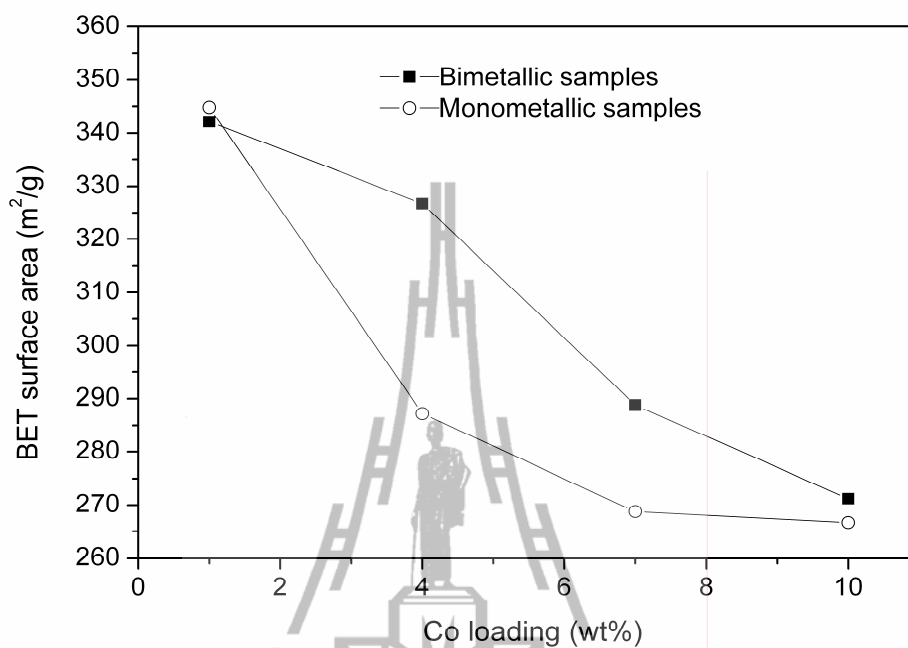


Figure 4.7 BET surface area of bimetallic and monometallic cobalt catalysts.

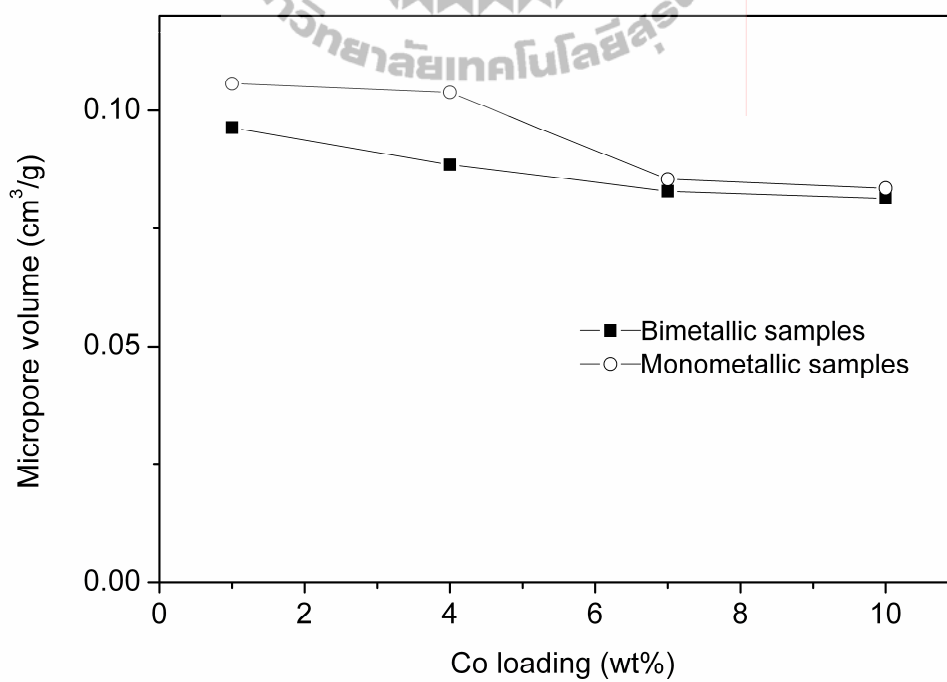


Figure 4.8 Micropore volume of bimetallic and monometallic cobalt catalysts.

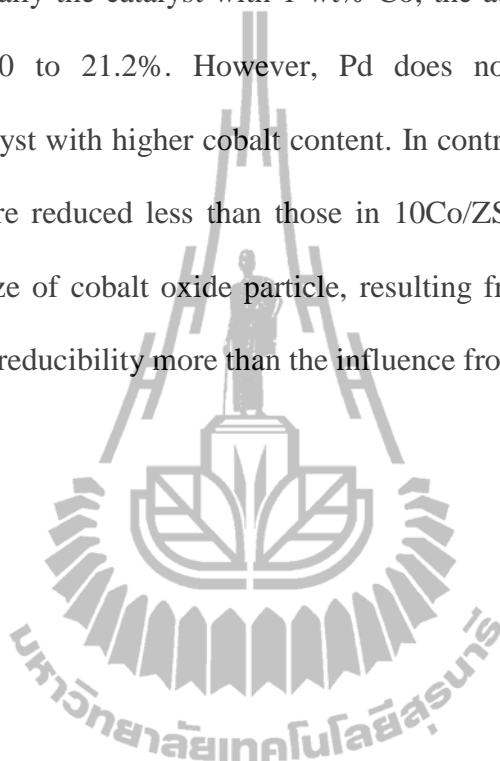
The correlation between cobalt content and surface area of catalyst is in the same trend as the work of El-Shobaky et al. (2002). They prepared 0.05, 0.1 and 0.2 Co_3O_4 supported on MgO (mol/mol). The particle sizes of Co_3O_4 determined by using Scherrer equation were 83, 90 and 136 Å for samples with 0.05, 0.1 and 0.2 mole Co_3O_4 /mol MgO, respectively. The BET surface area of these three samples also decreased with the increasing size of Co_3O_4 from 64 to 54 and 44 m^2/g , respectively. Thus, it can be implied from the result in this work that the size of cobalt oxide in the high cobalt content catalyst was larger than that in the sample with low cobalt content.

4.3.5 XANES spectroscopy of reduced catalysts supported on ZSM-5

XANES spectra of the reduced monometallic cobalt catalysts were used to determine the degree of reducibility by using the linear combination fitting. The fitting results are shown in Figure 4.9-4.12 and Table 4.3. For catalyst with 1 wt% Co, the fraction of metallic cobalt was not observed, indicating that the cobalt oxide can not be reduced under this condition. For the other samples, the fraction of metallic cobalt increased with the increasing cobalt content.

This result is consistent with the degree of reducibility of supported cobalt on NaY catalysts reported from Khemthong et al. (2010). Lapidus et al. (2007) also suggested that for catalysts with high cobalt content, there was more cationic cobalt phase that was not stabilized by interaction with support (large cobalt oxide particle). Thus, the catalyst with high amount of cobalt will be reduced easily. Moreover, other reports suggested that the reduction is strongly affected by the particle size of Co crystallite. The smaller particles are more difficult to reduce than the larger particle (Jacob et al., 2007; Saib et al., 2006).

The result from linear combination fitting of reduced bimetallic cobalt catalysts is shown in Table 4.3 and Figure 4.9-4.12. For catalysts with the same cobalt content, the addition of Pd to monometallic cobalt catalysts increased the reducibility. Especially the catalyst with 1 wt% Co, the addition of Pd increased the reducibility from 0 to 21.2%. However, Pd does not significantly affect the reducibility of catalyst with higher cobalt content. In contrast, cobalt oxide species in 10Co1Pd/ZSM-5 are reduced less than those in 10Co/ZSM-5. Therefore, it can be inferred that the size of cobalt oxide particle, resulting from the variation in cobalt content, affects the reducibility more than the influence from Pd addition.



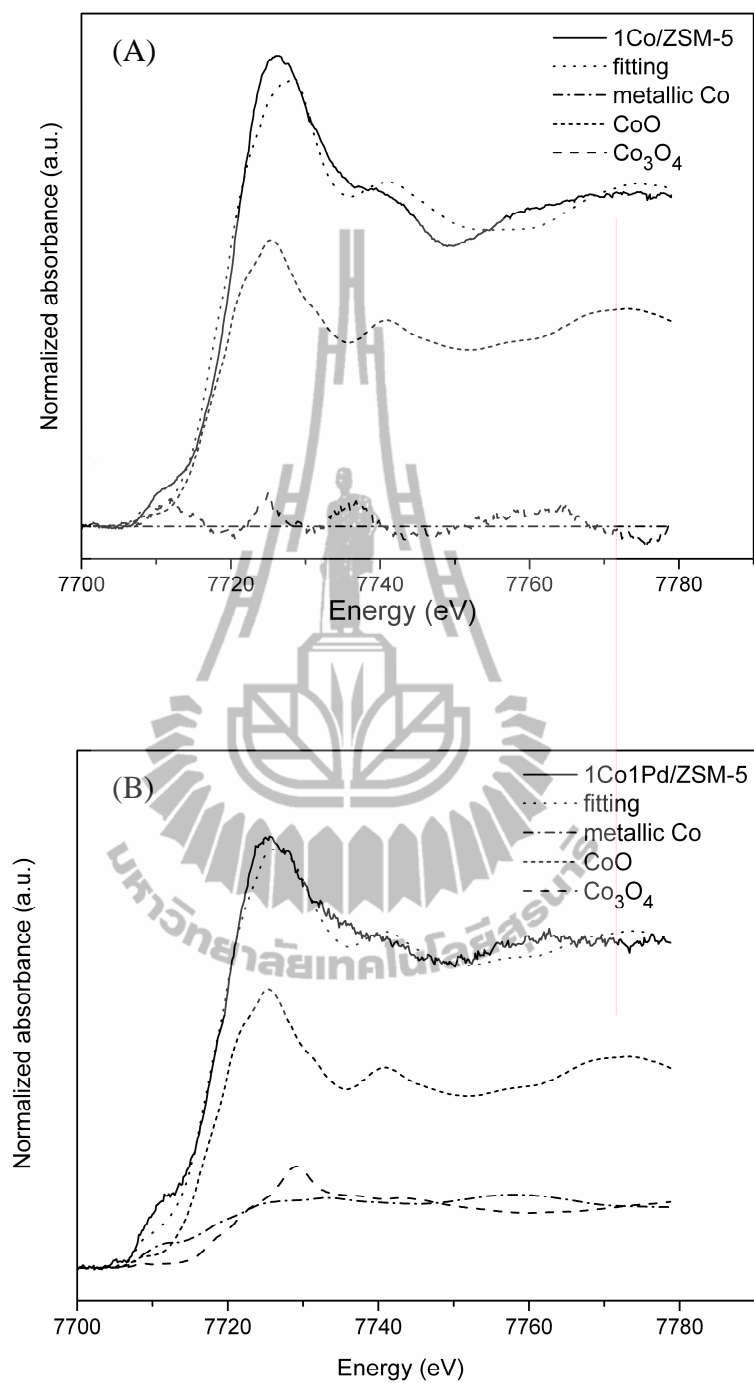


Figure 4.9 Linear combination fitting of 1Co/ZSM-5 (A) and 1Co1Pd/ZSM-5 (B) after reduction at 400 °C for 5 h.

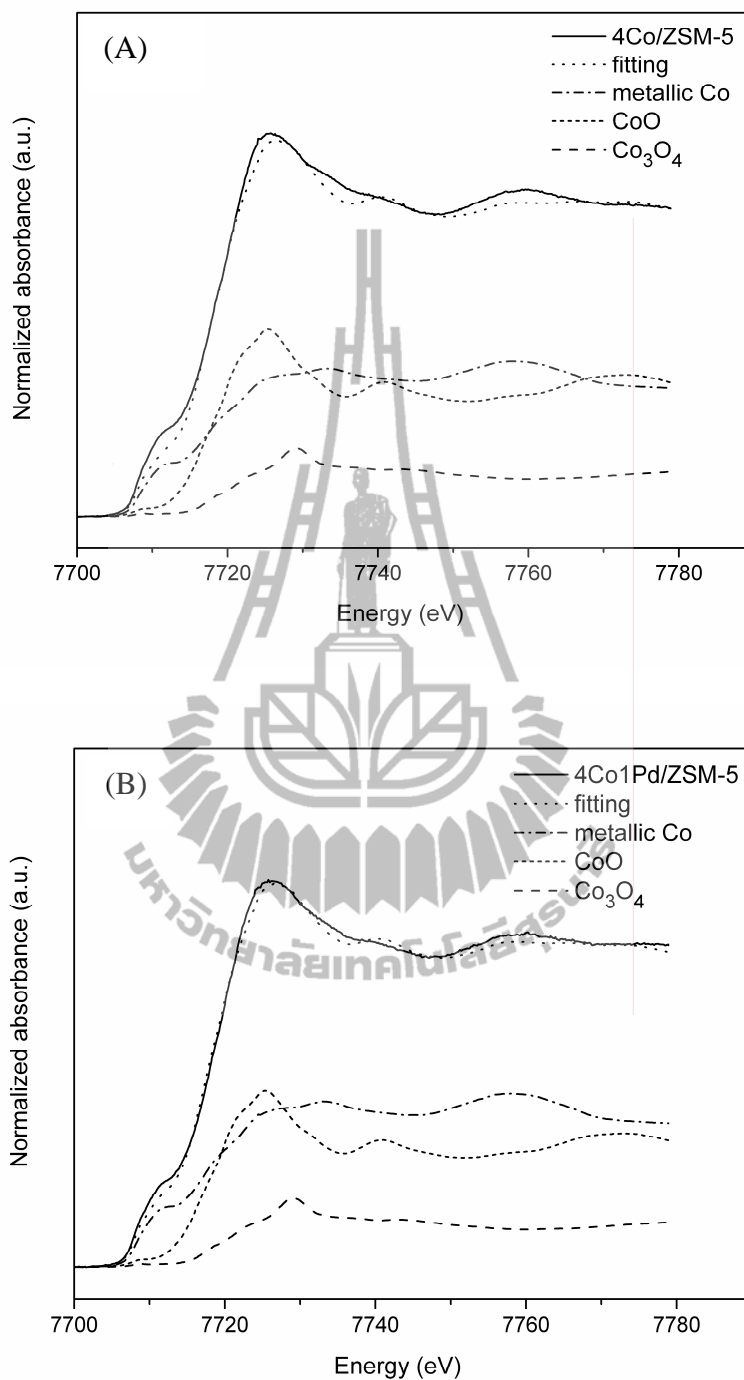


Figure 4.10 Linear combination fitting of 4Co/ZSM-5 (A) and 4Co1Pd/ZSM-5 (B) after reduction at 400 °C for 5 h.

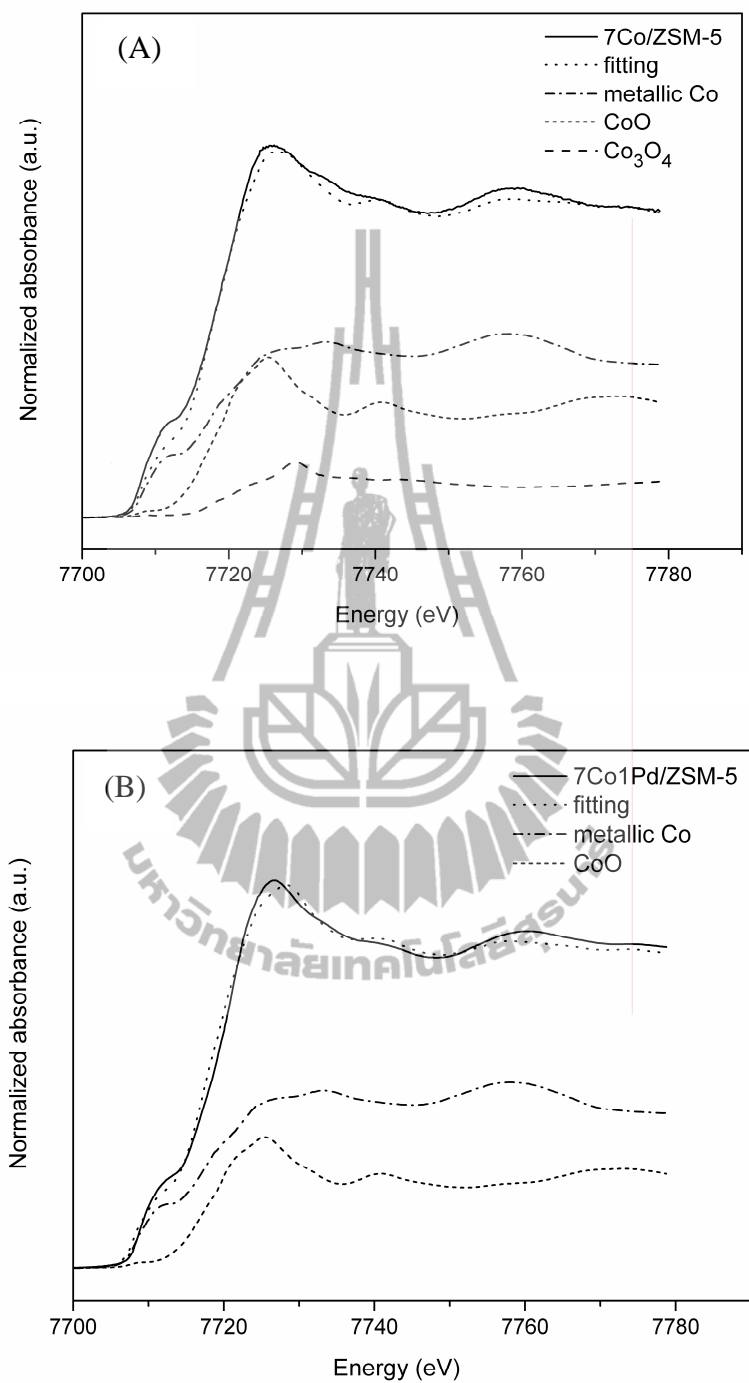


Figure 4.11 Linear combination fitting of 7Co/ZSM-5 (A) and 7Co1Pd/ZSM-5 (B) after reduction at 400 °C for 5 h.

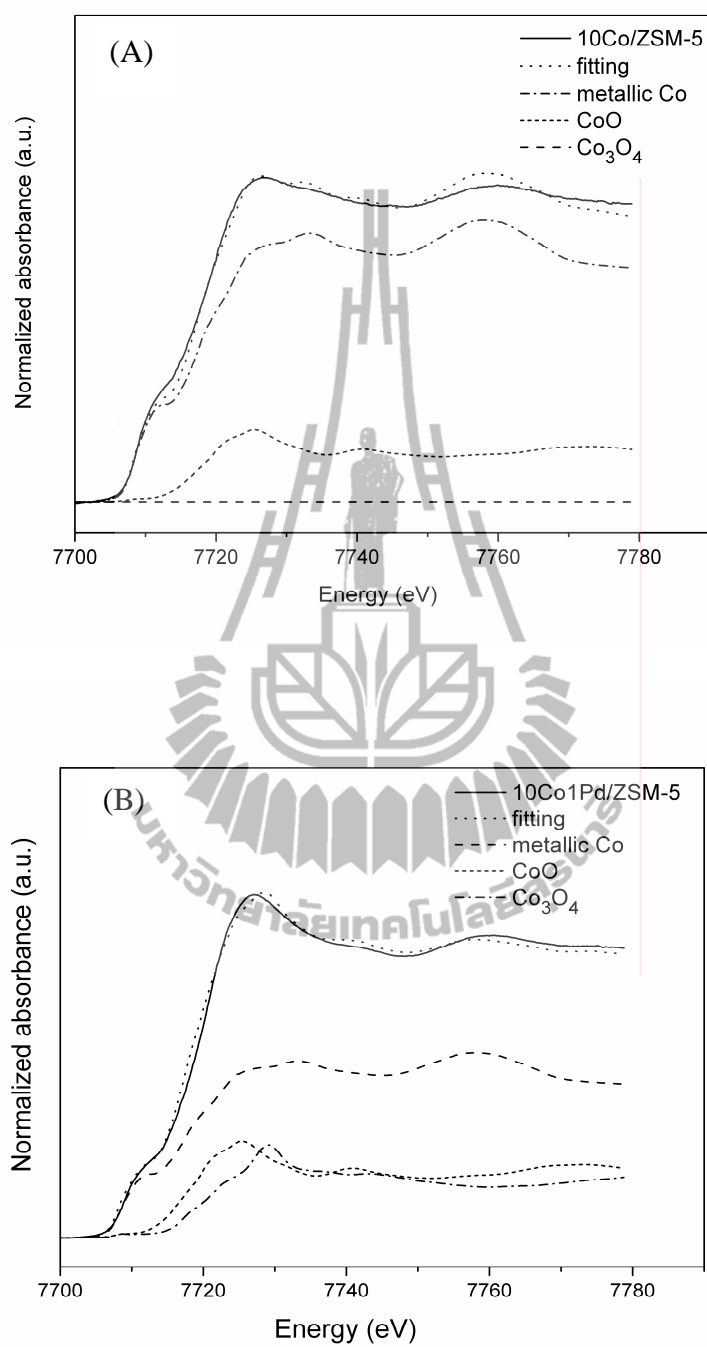


Figure 4.12 Linear combination fitting of 10Co/ZSM-5 (A) and 10Co1Pd/ZSM-5 (B) after reduction at 400 °C for 5 h.

Table 4.3 The fraction of cobalt species in mono- and bimetallic cobalt catalysts supported on ZSM-5 after reduction at 400°C for 5 h determined by linear combination fitting.

Samples	Fraction of cobalt species		
	Metallic Co	CoO	Co ₃ O ₄
1Co/ZSM-5	0.000	0.624	0.376
4Co/ZSM-5	0.456	0.415	0.129
7Co/ZSM-5	0.540	0.355	0.105
10Co/ZSM-5	0.853	0.168	0.000
1Co1Pd/ZSM-5	0.212	0.602	0.187
4Co1Pd/ZSM-5	0.491	0.380	0.125
7Co1Pd/ZSM-5	0.532	0.283	0.185
10Co1Pd/ZSM-5	0.582	0.230	0.188

4.3.6 Catalytic testing of supported cobalt catalysts on ZSM-5

4.3.6.1 Conversion

The activities for *n*-butane hydrogenolysis of monometallic cobalt catalysts supported on ZSM-5 are presented in Figure 4.13. The conversion at 410°C increased with the increasing of cobalt content in catalysts. This effect could be a result from an increasing number of active sites. In contrast, the conversion of catalyst with 7Co/ZSM-5 was higher than that of 10Co/ZSM-5. According to the surface area of 7Co/ZSM-5 and 10Co/ZSM-5 (Table 4.2), it could be inferred that the

cobalt particle in 10Co/ZSM-5 is larger than that of 7Co/ZSM-5. Even though the cobalt oxide in 10Co/ZSM-5 was reduced more than that in 7Co/ZSM-5, it might contain less surface cobalt active sites, which consequently exhibited less conversion.

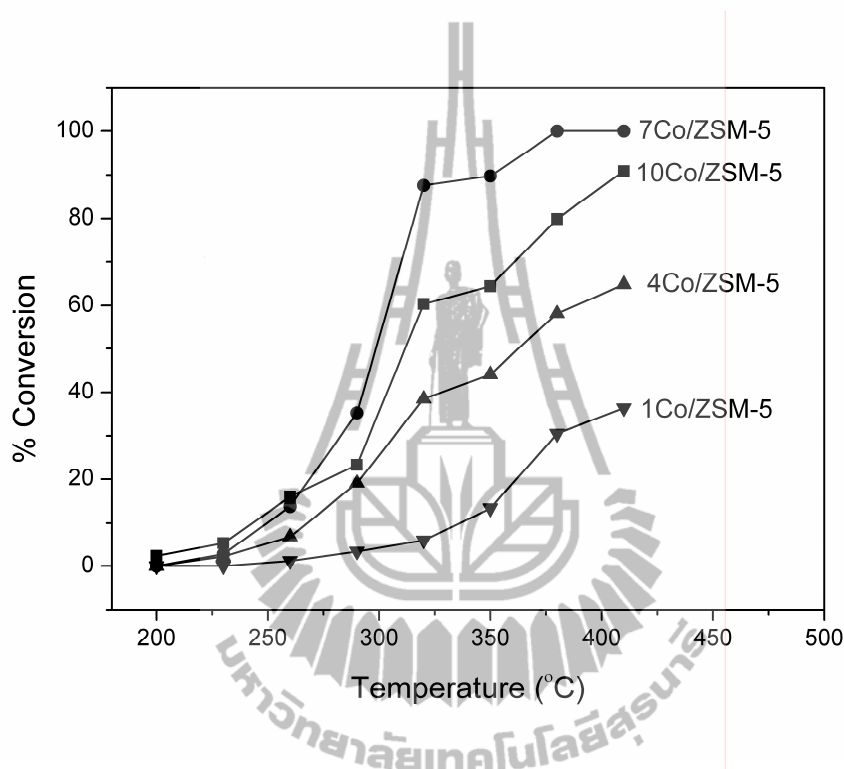


Figure 4.13 Conversion of *n*-butane on monometallic cobalt catalysts.

Reactant gases included He: H₂: *n*-butane in a mass ratio of 69.5: 30: 0.5 ml/min.

The activity of *n*-butane hydrogenolysis over bimetallic cobalt catalysts are presented in Figure 4.14. Conversion of *n*-butane hydrogenolysis over bimetallic cobalt catalysts increased when the cobalt content increased. Comparing to the monometallic cobalt catalysts in the same amount of cobalt, addition of palladium did not significantly enhance the overall conversion. However, it resulted in decreasing the reaction temperature as can be seen in Figure 4.13 and Figure 4.14. The conversion at 320°C for all bimetallic cobalt catalysts was higher than that of

monometallic catalysts. This phenomenon can be explained by the effect of H₂ spillover. This result is in accordance with the result reported from Ali et al. (2002). They found that addition of 1 wt% noble metal to cobalt clay-based catalysts two times increased the conversion of crude oil hydrocracking. The authors suggested that improvement in conversion was a result from H₂ spillover.

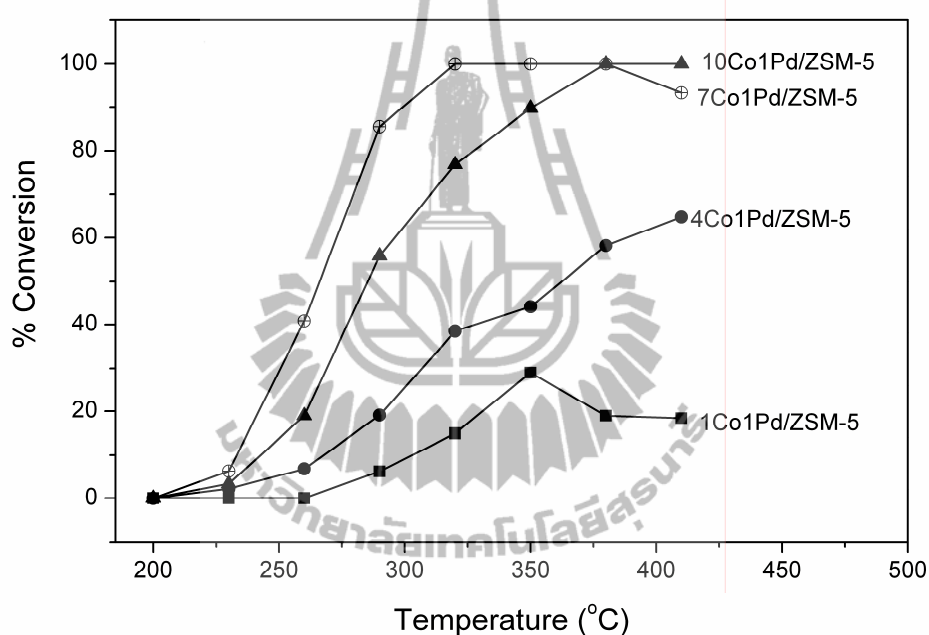


Figure 4.14 Conversion of *n*-butane on bimetallic cobalt catalysts.

Reactant gases included He: H₂: *n*-butane in a mass ratio of 69.5: 30: 0.5 ml/min.

Figure 4.15-4.16 shows the *n*-butane conversion per millimole of cobalt in catalysts tested in this work. Among these catalysts, the 1Co/ZSM-5 clearly showed the highest conversion per millimole of cobalt; however, its activity was maximum only approximately 40% conversion. On the other hand, the 7Co1Pd/ZSM-5 shows lower conversion per millimoles of cobalt but the reaction over this catalyst

occurred at lower temperature and its overall conversion was essentially high. Thus, it could be concluded that the 7Co1Pd/ZSM-5 had the highest activity among the catalysts in this work.

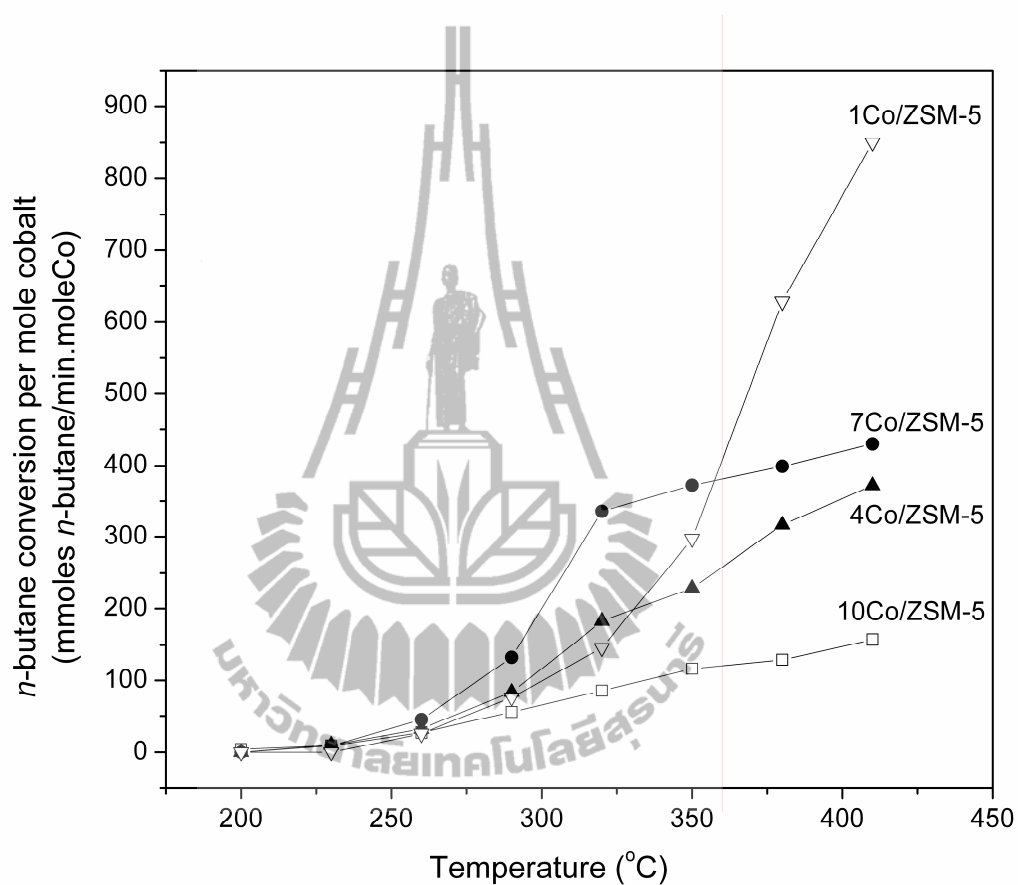


Figure 4.15 Conversion of *n*-butane per mole cobalt of monometallic cobalt catalysts. Reactant gases included He: H₂: *n*-butane in a mass ratio of 69.5: 30: 0.5 ml/min.

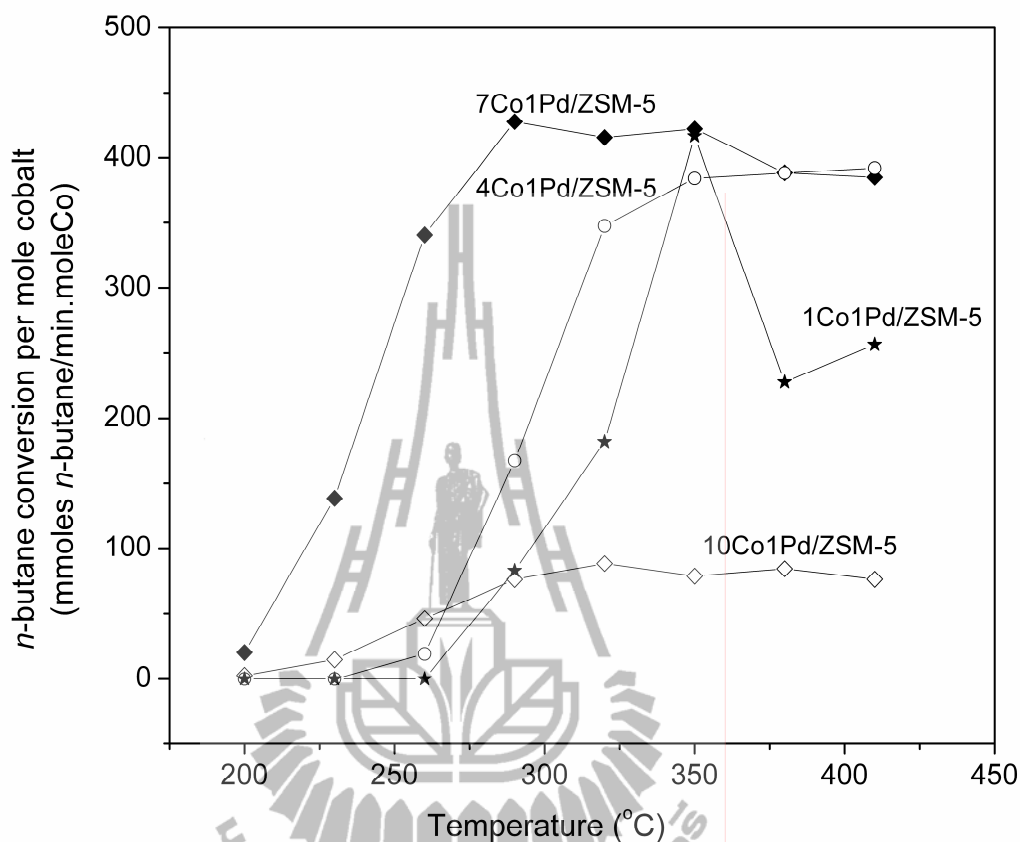


Figure 4.16 *n*-butane conversion per mole cobalt of bimetallic cobalt catalysts.

Reactant gases included He: H₂: *n*-butane in a mass ratio of 69.5: 30: 0.5 ml/min.

4.3.6.2 Selectivity

Methane was the only product observed in *n*-butane hydrogenolysis over monometallic cobalt catalysts (Figure 4.17-4.18), indicating that cobalt was very selective to the multiple hydrogenolysis. For bimetallic cobalt catalysts (Figure 4.19-4.20), besides methane, small amount of ethane and propane is observed especially at high temperature. According to Jackson et al. (1998), the metals Pt and Pd have high selectivity for single hydrogenolysis. On the other hand, W, Ta, Fe and Co all have high tendency for total degradation to methane. Thus the product selectivity from this

work suggested that the presence of ethane and propane over the bimetallic cobalt catalyst could be a result from Pd in catalysts.

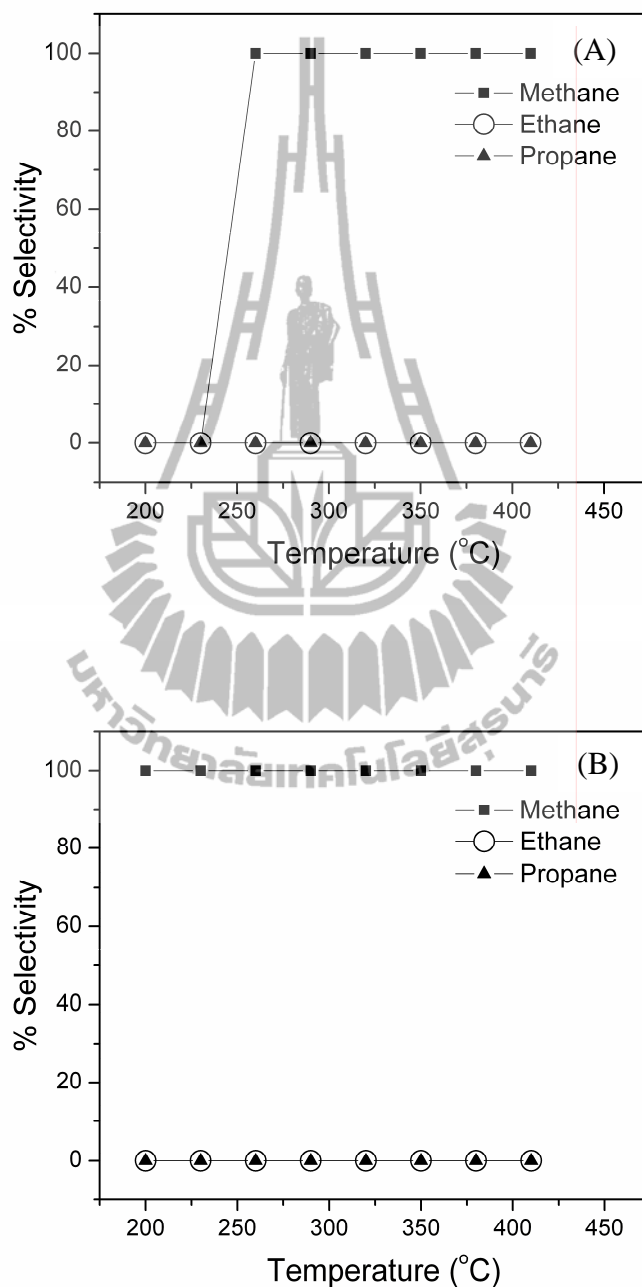


Figure 4.17 Selectivity of product from *n*-butane hydrogenolysis on 1Co/ZSM-5 (A) and 4Co/ZSM-5 (B). Reactant gases included He: H₂: *n*-butane in a mass ratio of 69.5: 30: 0.5 ml/min.

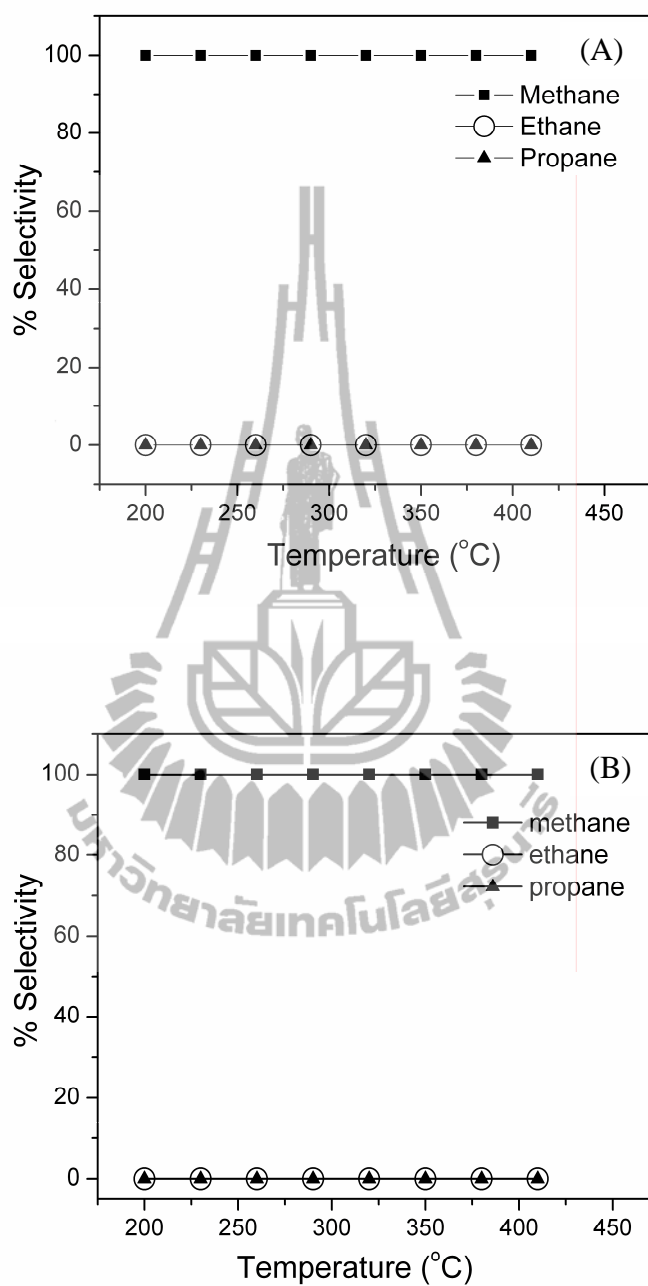


Figure 4.18 Selectivity of product from *n*-butane hydrogenolysis on 7Co/ZSM-5 (A) and 10Co/ZSM-5 (B). Reactant gases included He: H₂: *n*-butane in a mass ratio of 69.5: 30: 0.5 ml/min.

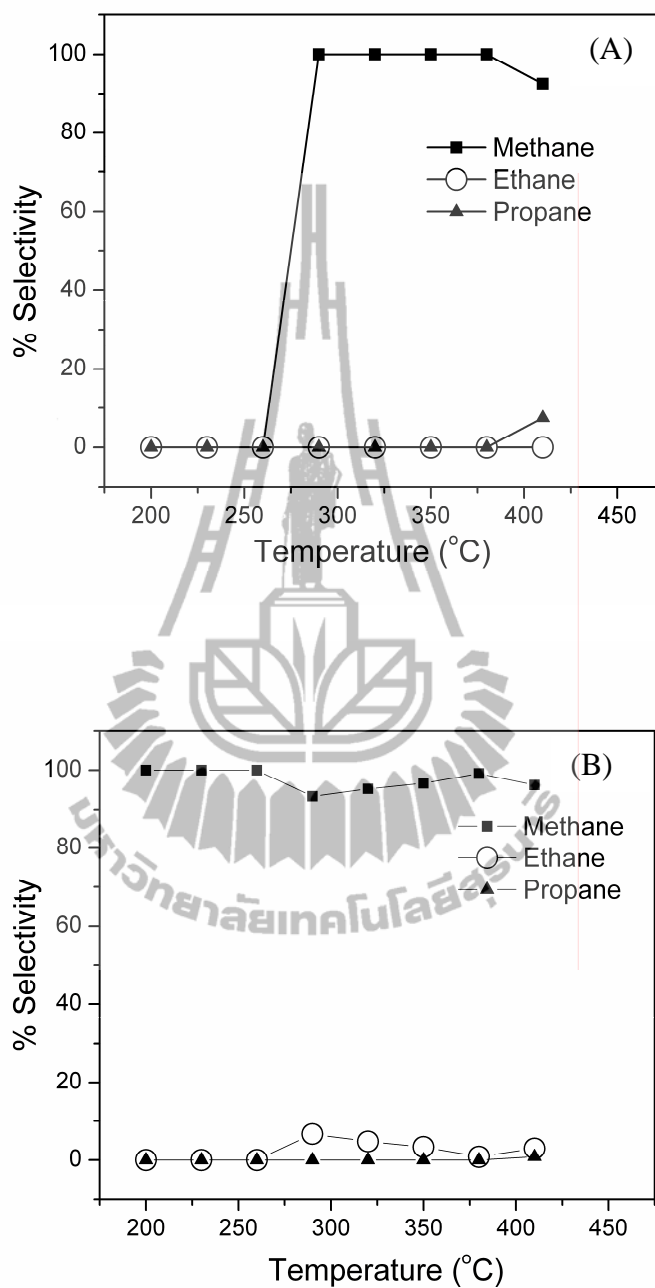


Figure 4.19 Selectivity of *n*-butane hydrogenolysis on 1Co1Pd/ZSM-5 (A) and 4Co1Pd/ZSM-5 (B). Reactant gases included He: H₂: *n*-butane in a mass ratio of 69.5: 30: 0.5 ml/min.

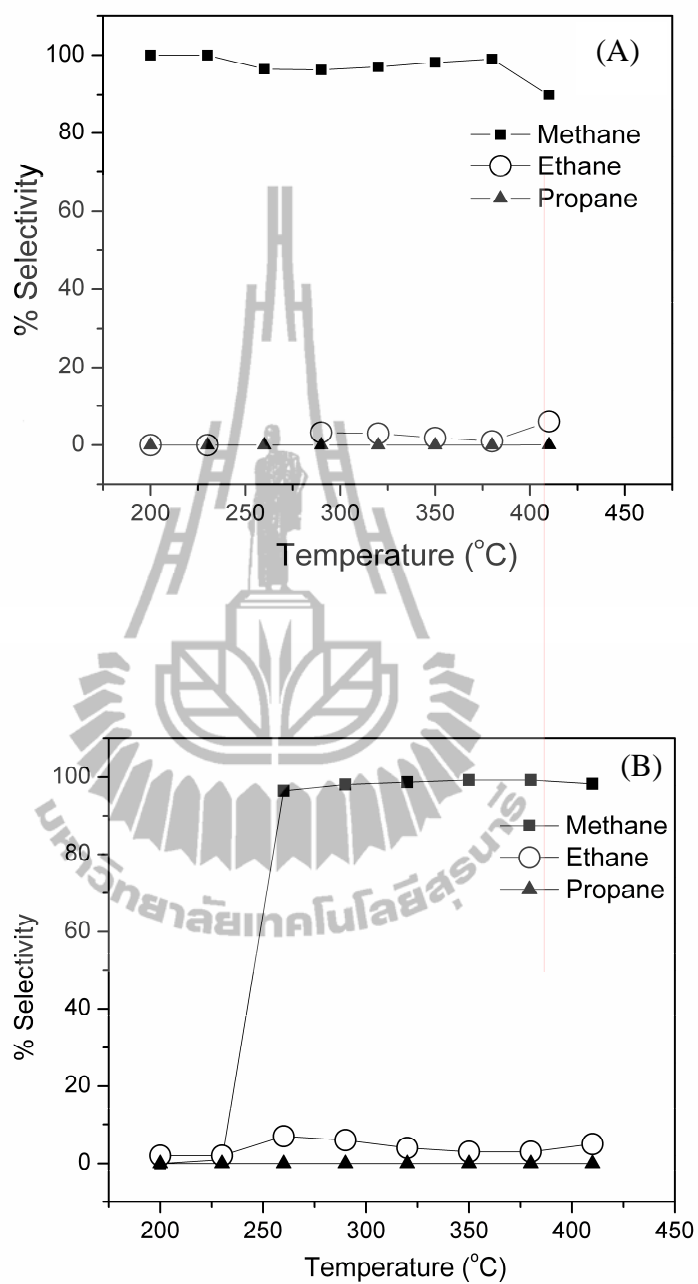


Figure 4.20 Selectivity of *n*-butane hydrogenolysis on 7Co1Pd/ZSM-5 (A) and 10Co/ZSM-5 (B). Reactant gases included He: H₂: *n*-butane in a mass ratio of 69.5: 30: 0.5 ml/min.

4.4 Conclusions

Types of support greatly influenced reducibility of supported cobalt species. In this study, the cobalt species supported on zeolite ZSM-5 were reduced easier than those on zeolite NaY. The activity for *n*-butane hydrogenolysis of 7Co1Pd/ZSM-5 was consequently higher than that of 1Pd7Co/NaY. The reducibility of cobalt species supported on ZSM-5 also depended on cobalt content. In general, catalysts with low metal loading consisted of small cobalt oxide particles which are difficult to reduce to the metallic form. Thus, the catalyst with high cobalt loading had high degree of reduction relative to the low cobalt loading catalysts.

Addition of 1 wt% Pd to Co/ZSM-5 catalyst promoted the reducibility only in 1Co/ZSM-5. It showed non-significant effect on the samples with higher cobalt contents. Activity for *n*-butane hydrogenolysis on Co/ZSM-5 catalysts increased with cobalt loading up to 7 wt% Co. The 10Co/ZSM-5 showed lower activity than 7Co/ZSM-5 even though it presented a high degree of reduction. This effect could be explained by the difference in active sites in the two catalysts.

4.5 References

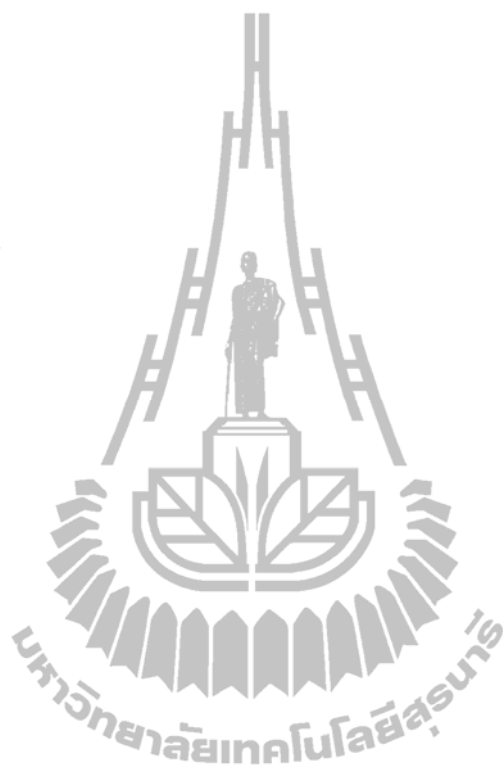
- Ali, M. A., Kimura, T., Suzuki, Y., Al-Saleh, M. A., Hamid, H., and Inui, T. (2007). Hydrogen spillover phenomenon in noble metal modified clay-based hydrocracking catalysts. **Appl. Catal. A-Gen.** 277: 63-72.
- Al-Saleh, M. A., Hossain, M. M., Shalabi, M. A., Kimura, T., and Inui, T. (2003). Hydrogen spillover effects on Pt–Rh modified Co–clay catalysts for heavy oil upgrading. **Appl. Catal. A-Gen.** 253: 453-459.
- Boudart, M. (1969). Catalysis by supported metals. **Adv. Catal.** 20: 153-166.
- Chu, W., Chernavskii, P. A., Gengembre, L., Pankina, G. A., Fongarland, P., and Khodakov, A. Y. (2007). Cobalt species in promoted cobalt alumina-supported Fischer–Tropsch catalysts. **J. Catal.** 252: 215-230.
- Danuthai, T., Jongpatiwut, S., Rirksomboon, T., Osuwan, S., and Resasco, D. E. (2009). Conversion of methylesters to hydrocarbons over an H-ZSM-5 zeolite catalyst. **Appl. Catal. A-Gen.** 361: 99-105.
- El-Shobaky, G. A., Doheim, M. M., Ghozza, A. M., and El-Boohy, H. A. (2002). Catalytic conversion of ethanol over $\text{Co}_3\text{O}_4/\text{MgO}$ system treated with γ -irradiation. **Mater. Lett.** 57: 525-531.
- Hossain, M. M. (2006). Influence of noble metals (Rh, Pd, Pt) on Co-saponite catalysts for HDS and HC of heavy oil. **Chem. Eng. J.** 123: 15-23.
- Jackson, S. D., Kelly, G. J., and Webb, G. (1998). Supported metal catalysts; preparation, characterization, and function part VI. Hydrogenolysis of ethane, propane, *n*-butane and iso-butane over supported platinum catalysts. **J. Catal.** 176: 225-234.

- Jacobs, G., Das, T. K., Zhang, Y., Li, J., Zacoillet, G., and Davis, B. H. (2002). Fischer–Tropsch synthesis: support, loading, and promoter effects on the reducibility of cobalt catalysts. **Appl. Catal. A-Gen.** 233: 263-281.
- Jacobs, G., Ji, Y., Davis, B. H., Cronauer, D., Kropf, A. J., and Marshall, C. L. (2007). Fischer–Tropsch synthesis: temperature programmed EXAFS/XANES investigation of the influence of support type, cobalt loading, and noble metal promoter addition to the reduction behavior of cobalt oxide particles. **Appl. Catal. A-Gen.** 333: 177-191.
- Jiang, Y., Wua, Y., Xie, B., Xie, Y., and Qian, Y. (2002). Moderate temperature synthesis of nanocrystalline Co_3O_4 via gel hydrothermal oxidation. **Mater. Chem. Phys.** 74: 234-237.
- Karge, H. G., Mavrodinova, V., Zheng, Z., and Beyer, H. K. (1991). Cracking of n-decane over Lanthanum Y catalysts: Comparison of Lanthanum Y catalysts obtained by solid-state ion exchange and ion exchange in solution. **Appl. Catal.** 75(1): 343-357.
- Khemthong, P., Klaysubun, W., Prayoonpokarach, S., Roessner, F., and Wittayakun, J. (2010). Comparison between cobalt-platinum supported on zeolite NaY: Cobalt reducibility and their catalytic performance for butane hydrogenolysis. **J. Ind. Eng. Chem.** 16: 531-538.
- Khemthong, P., Prayoonpokarach, S., and Wittayakun, J. (2007). Synthesis and characterization of zeolite LSX from rice husk silica. **Suranaree J. Sci. Technol.** 12(4): 367-379.
- Lapidus, A. L., Budtsov, V. S., Eliseev, O. L., and Erofeev, A. B. (2007). Prediction of stability of cobalt catalysts for hydrocarbon synthesis from CO and H_2 in

- terms of resistance of cobalt crystallites against high-temperature agglomeration. **Solid. Fuel. Chem.** 41(6): 331-334.
- Leclercq, G., Pietrzyk, S., Lamonier, J. F., Leclercq, L., Bouleau, L. M., and R. Maurel. (1995). Bimetallic nickel-rhodium catalysts. II. Activity and selectivity in hydrogenolysis of butane. **Appl. Catal. A-Gen.** 123: 161-172.
- Maroto-Valiente, A., Cerro-Alarcón, M., Guerrero-Ruiz, A., and Rodríguez-Ramos, I. (2005). Effect of the metal precursor on the surface site distribution of Al₂O₃ –supported Ru catalysts: Catalytic effects on the *n*-butane/H₂ test. **Appl. Catal. A-Gen.** 283: 23-32.
- Moen, A., Nicholson, D. G., Ronning, M., Lambie, G. M., Lee, J. F., and Emerich, H. (1997). X-Ray absorption spectroscopic study at the cobalt K-edge on the calcination and reduction of the microporous cobalt silicoaluminophosphate catalyst CoSAPO-34. **J. Chem. Soc. Faraday T.** 93(22): 4071-4077.
- Morales-Pacheco, P., Domínguez, J. M., Bucio, L., Alvarez, F., Sedranc, U., and Falco, M. (2011). Synthesis of FAU(Y) and MFI(ZSM5)-nanosized crystallites for catalytic cracking of 1,3,5-triisopropylbenzene. **Catal. Today.** 166: 25-38.
- Panpa, W. and Jinawath., S. (2009). Synthesis of ZSM-5 zeolite and silicalite from rice husk ash. **Appl. Catal. B-Environ.** 90: 389-394.
- Pârvulescu, V., Ruwet, M., Grange, P., and Pârvulescu, V. I. (1998). Preparation, characterization and catalytic behaviour of cobalt-niobia catalysts. **J. Mol. Catal. A-Chem.** 135: 75-88.

- Ravel., B. and Newville, M. (2005). ATHENA, ARTEMIS, HEPHAESTUS: data analysis for X-ray absorption spectroscopy using IFEFFIT. **J. Synchrotron Radiat.** 12: 537-541.
- Saib, A. M., Borgna, A., van de Loosdrecht, J., van Berge, P. J., and Niemantsverdriet, J. W. (2006). XANES study of the susceptibility of nano-sized cobalt crystallites to oxidation during realistic Fischer-Tropsch synthesis. **Appl. Catal. A-Gen.** 312: 12-19.
- Sault, A. G. (1995). Reduction behavior of metals supported on hydrous titanium oxide ion-exchange materials. **J. Catal.** 156: 154-162.
- Sun, S., Fujimoto, K., Yoneyama, Y., and Tsubaki, N. (2002). Fischer-Tropsch synthesis using Co/SiO₂ catalysts prepared from mixed precursors and addition effect of noble metals. **Fuel** 81: 1583-1591.
- Tang, C. W., Wang, C. B., and Chien, S. H. (2008). Characterization of cobalt oxides studied by FT-IR, Raman, TPR and TG-MS. **Thermochim. Acta.** 473: 68-73.
- Wittayakun, J., Khemthong, P., and Prayoonpokarach, S., (2008). Synthesis and characterization of zeolite NaY from rice husk silica. **Korean J. Chem. Eng.** 25(4): 861-864.
- Xiong, H., Zhang, Y., Liew, K., and Li, J. (2009). Ruthenium promotion of Co/SBA-15 catalysts with high cobalt loading for Fischer-Tropsch synthesis. **Fuel. Process. Technol.** 90: 237-246.
- Yao, H. C., Yao, Y. F. Y., and Otto, K. J. (1979). Effects of the surface structure of Rh γ -Al₂O₃ on the hydrogenolysis of *n*-pentane on the oxidation of *n*-butane, and on the reduction of nitric oxide. **J. Catal.** 56: 21-31.

Yung, M. M., Holmgren, E. M. and Ozkan, U. S. (2007). Cobalt-based catalysts supported on titania and zirconia for the oxidation of nitric oxide to nitrogen dioxide. **J. Catal.** 247: 356-367.



CHAPTER V

**FORMATION OF MANGANESE TRICARBONYL ON
THE MgO SURFACE FROM Mn₂(CO)₁₀ :
CHARACTERIZATION BY INFRARED, ELECTRON
PARAMAGNETIC RESONANCE, AND X-RAY
ABSORPTION SPECTROSCOPIES**

Abstract

This chapter focuses on preparation a structurally well-defined manganese complexes on high-area MgO powder by vapor deposition of Mn₂(CO)₁₀. The supported species were treated under O₂ at 673 K and evacuated at the same temperature and then characterized by infrared (IR), electron paramagnetic resonance (EPR), and X-ray absorption spectroscopies. The results show that when the manganese loading of the sample was 3.0 wt%, most of the Mn₂(CO)₁₀ was physisorbed, but when the loadings were less, chemisorbed species predominated, being formed by reaction of Mn₂(CO)₁₀ with hydroxyl groups on the MgO surface. Treatment of samples containing 1.0 wt% Mn with O₂ at room temperature resulted in oxidation of the manganese and the formation of surface species that are well represented as the d⁴ complex Mn(CO)₃(O_s)₃ (where O_s is surface oxygen of MgO), as indicated by IR and extended X-ray absorption fine structure (EXAFS) spectra. The

EXAFS data show Mn–C, C≡O, and Mn–O_s bond lengths as 1.90, 1.43, and 1.98 Å, respectively.

5.1 Introduction

Oxide-supported metal complexes are widely investigated materials that find important applications as industrial catalysts (Giebeler et al., 2007; Niaei et al., 2010). They offer unique opportunities for fundamental investigations of organometallic compounds in the absence of solvents, because they may be understood as metal complexes incorporating extremely heavy ligands-the supports-allowing investigation of their chemistry in the presence of gas-phase reactants.

The supports in supported metal complex catalysts are typically porous metal oxides (Yang et al., 2009), chosen because they provide high surface areas on which the metal complexes can be highly dispersed-giving high catalytic activities per unit volume of material. Some of the best-understood supported metal complexes are carbonyls of group-8 metals (Ishihara et al., 1994). The chemistry of carbonyls of group-7 metals has also been investigated, for example, that of rhenium carbonyls, including mono-, di-, and tri-nuclear species (Kirlin et al., 1990; Papile et al., 2000), but only little has been reported about supported complexes of manganese.

This chapter reports an investigation of samples prepared by the reaction of dimanganese decacarbonyl, Mn₂(CO)₁₀, with MgO and reactions of the supported species. Manganese was chosen because its complexes are important in homogeneous catalysis (Yang and Eckert, 1988; Vartzouma et al., 2007) and their supported analogues might be expected to be good candidate catalysts, being characterized by robustness and ease of separation from products combined with the uniformity and

selectivity of homogeneous catalysts. $\text{Mn}_2(\text{CO})_{10}$ was chosen as the precursor because it is reactive with metal oxides and zeolites e.g., $\gamma\text{-Al}_2\text{O}_3$ (Zecchina, 1998), MCM-41 (Burch et al., 1996) and zeolite NaY (Dossi et al., 1997) and the infrared (IR) spectra of CO ligands on the resulting surface species provide valuable information about the structure and bonding of the metal complexes. The high vapor pressure of $\text{Mn}_2(\text{CO})_{10}$ allows sample preparation by chemical vapor deposition (CVD).

MgO was chosen as a support because it is available as a powder with high surface area, facilitating the preparation of surface species in samples with high enough loadings of the metal complex per unit volume to give good signal-to-noise ratios in the spectra (Paganini et al., 1997; Rainer et al., 1998). Our specific goal was to elucidate the surface chemistry of relatively well-defined manganese carbonyls on MgO by taking advantage of a set of methods that are highly complementary and expected to provide insight into the structures of the surface species, namely, IR, electron paramagnetic resonance (EPR), extended X-ray absorption fine structure (EXAFS), and X-ray absorption near edge structure (XANES) spectroscopies.

5.2 Experimental

5.2.1 Treatment of MgO

MgO powder (EMD Science, 98.0%) was calcined in flowing dry O_2 (Airgas, 99.9999%) as the temperature was ramped from room temperature to 400°C at a rate of $3^\circ\text{C}/\text{min}$, then held in flowing O_2 at 400°C for 4 h, and subsequently treated under vacuum (pressure $\approx 1 \times 10^{-3}$ mbar) at 400°C for an additional 16 h. The calcined MgO, which had been partially decarbonated and partially dehydroxylated, was kept under vacuum as it was cooled to room temperature, and then it was stored in an N_2 -filled

glovebox (Vacuum Atmospheres, with O₂ and moisture contents each <1.0 ppm) before being used for the preparation of the supported manganese complexes or subjected to characterization by IR and EPR spectroscopies (as described below). The BET surface area of the calcined MgO was approximately 70 m²/g.

5.2.2 Synthesis of MgO-supported samples from Mn₂(CO)₁₀

The MgO-supported samples were synthesized from Mn₂(CO)₁₀ (Strem, 98.0%). The synthesis and handling were performed with exclusion of air and moisture on a double-manifold Schlenk line. Glassware was dried at 120°C overnight prior to use. In an N₂-filled glovebox, a flask containing the highly volatile Mn₂(CO)₁₀ was quickly connected to another flask containing calcined MgO powder via a glass tube equipped with a Teflon® valve separating the two flasks and ground-glass joints. The apparatus was removed from the glovebox and connected to the Schlenk line via a line with a Teflon® valve. The flask containing Mn₂(CO)₁₀ was placed in a dry-ice/isopropanol bath (temperature ≈ -25°C). The system was evacuated for 15 min and then warmed to room temperature in static vacuum to allow sublimation of the Mn₂(CO)₁₀. The masses of Mn₂(CO)₁₀ and MgO were chosen to give supported samples containing 0.10, 1.0, and 3.0 wt% Mn. Each sample was evacuated overnight and stored in the glovebox.

5.2.3 Sample treatment

5.2.3.1 Decarbonylation in the presence of H₂

The samples formed from Mn₂(CO)₁₀ on MgO were decarbonylated in the presence of flowing H₂ in a once-through quartz tubular flow reactor. The powder sample (0.50 g) was loaded into the reactor in the glovebox. The sample was held by a frit mounted near the center of the tube, which was sealed on both ends with O-ring

compression fittings. The tube was removed from the glovebox and held in an electrically heated tube furnace, and then both ends of the reactor were connected to the flow system, all without exposure of the sample to air. The temperature in the reactor was measured below the frit with a K-type thermocouple. H₂ (Airgas, 99.9999%) flowed through the reactor at 70 mL(NTP)/min as the temperature was ramped to 700 °C at a rate of 2 °C /min. The temperature of the reactor was held at 700 °C for 2 h, and then it was cooled to room temperature while the H₂ flow continued. The effluent gases from the reactor were analyzed by an online mass spectrometer (Pfeiffer Vacuum, OmniStar). The reactor was then flushed with helium (Praxair, 99.999%) before being transferred back to the glovebox.

5.2.3.2 Treatment in O₂

Each sample was loaded into a once-through quartz tubular flow reactor and connected to the flow system as in the decarbonylation experiment. At room temperature, O₂ (Airgas, 10% by volume in helium) was fed to the reactor at 60 mL(NTP)/min for 6 h, then the sample was flushed with helium, and the reactor was sealed and returned to the glovebox. In some experiments, the effluent was analyzed with the online mass spectrometer.

5.2.4 Sample characterization

5.2.4.1 IR spectroscopy

The MgO support and the supported samples were characterized by IR spectroscopy at room temperature with a Bruker IFS 66v Fourier transform spectrometer equipped with DTGS and HgCdTe detectors. In the glovebox, each sample was pressed between two KBr windows and placed in a gas-tight cell (International Crystal Laboratories). The cell was then loaded into an airtight

container as a precaution to minimize air exposure before transfer of the cell to the spectrometer. The sample chamber of the spectrometer was evacuated (pressure ≈ 1 mbar), and the vacuum was maintained as spectra of the sample were recorded in transmission mode with a resolution of 4 cm^{-1} . Each reported spectrum is the average of 128 scans.

5.2.4.2 EPR spectroscopy

The untreated and calcined MgO and the supported samples prepared from $\text{Mn}_2(\text{CO})_{10}$ were characterized by EPR spectroscopy. Each sample in the N_2 -filled glovebox was loaded into a 4-mm O.D. quartz EPR tube and sealed with an Ultra-torr® fitting. The EPR tube was removed from the glovebox and evacuated (pressure $\approx 1 \times 10^{-3}$ mbar) for 30 min and then flame sealed. EPR data were collected at the CalEPR center at the University of California, Davis. Each sample was scanned at room temperature in a Bruker ECS 106 X-band (≈ 9.5 GHz) spectrometer equipped with a Bruker ER4102ST cavity operating in the TE102 mode. Measurements were performed with a microwave power of 10 mW, a field modulation of 0.2 mT at 100 kHz, and a sweep rate of 0.1 mT/s. For each spectrum, 10 scans were accumulated.

5.2.4.3 EXAFS spectroscopy

The sample formed from $\text{Mn}_2(\text{CO})_{10}$ and MgO (1.0 wt% Mn) after treatment in O_2 was characterized by X-ray absorption spectroscopy. Data collection was performed at beamline 9-BM at the Advanced Photon Source (APS) at Argonne National Laboratory. The beamline is equipped with a double-crystal Si(111) monochromator which was detuned by approximately 30% at the Mn K edge to minimize the presence of higher harmonics in the X-ray beam. The intensity of the X-rays entering and exiting the sample was measured with two gas-filled ion chambers

(FMB-Oxford), and a third ion chamber was used to collect the spectrum of a manganese foil used as a reference for energy calibration.

The sample was loaded into a stainless steel vacuum tube sealed with O-rings and transferred to the synchrotron, where it was handled in an N₂-filled glovebox; the O₂ and moisture contents of the glovebox were 0.10 and 1.3 ppm, respectively. The mass of the sample was calculated to provide an absorbance about 2.5 and the optimized signal-to-noise ratio. The sample was weighed, mixed with inert boron nitride powder (Aldrich, 98.0%, particle diameter \cong 1 μ m), pressed into a self-supporting wafer, and loaded into the cell (Jentoft et al., 1996) which allowed scanning of the sample without exposure to air. The cell was transferred to the beam line and mounted between the first two ion chambers. The sample was scanned at room temperature in transmission mode at the Mn K edge (6539 eV) with a step size of 0.07 k (k is the wave vector) in the EXAFS region. The reported spectrum is the average of five spectra.

5.2.5 EXAFS data analysis

EXAFS data analysis was conducted by using the “difference file” technique (Koningsberger et al., 2000) with the software XDAP (Vaarkamp et al., 1995). First, the five scans were aligned and averaged. The functions used to construct the structural models and minimize the error are shown elsewhere (Koningsberger et al., 2000). Reference backscattering amplitudes were calculated by using the FEFF7.0 software (Rehr and Albers, 2000). Crystallographic data characterizing Mn₂(CO)₁₀ (Dahl and Rundle, 1963) for the representation of Mn–C, Mn–O* (O* is carbonyl oxygen; the Mn–C–O moiety is characterized by collinear multiple scattering), and Mn–Mn contributions were included in the fitting. Crystallographic data

characterizing Mn_2O_3 and MnMg alloy (Pearson et al., 1985) were used for Mn–O_s (Mn–O_s refers to a relatively short Mn–O distance in supported samples incorporating oxygen of the support surface) and Mn–Mg contributions, respectively.

The fitting was done in *R*-space (distance space) by using three *k*-weightings (k^0 , k^1 , and k^2). In the fitting with a candidate model, the parameters characterizing each contribution, the coordination number *N*, the $\Delta\sigma^2$ value (Debye-Waller factor), the interatomic distance *R*, and the inner potential correction ΔE_0 were varied until an optimized fit was obtained for all *k*-weightings. For a candidate model to be considered acceptable, it was required to fit satisfactorily with all the *k*-weightings. The EXAFS data were analyzed with 11 free parameters over the range $3.08 < k < 9.50 \text{ \AA}^{-1}$. The number of parameters used in the fitting did not exceed the statistically justified number calculated with the Nyquist theorem (14.3) (Sayers et al., 1971).

Two criteria were used to determine whether an EXAFS fit was satisfactory; first, analysis was done to determine whether the addition of each shell to the model decreased the value of $(\Delta\chi)^2$ (International XAFS Society, www, 2010) and, second, the parameters for each shell were checked to determine whether they were physically appropriate; specifically, the value of ΔE_0 was considered to be appropriate in the range -10 to 10 eV, and the value of $\Delta\sigma^2$ was constrained not to exceed $1.5 \times 10^{-2} \text{ \AA}^{-2}$.

5.2.6 XANES data analysis

Data in XANES region were analyzed with the software Athena (Ravel and Newville, 2005). The edge position of the manganese in the sample was taken as the inflection point in the measured X-ray absorption spectrum. The energy scale of the XAFS spectrum was calibrated by setting the edge position of the manganese foil to the reported value. The reported XANES spectrum is the average of five spectra.

5.3 Results

5.3.1 Spectroscopic characterization of MgO

The EPR spectrum of MgO calcined at 400 °C (Figure 5.1, spectrum b) lacks information that would identify the MgO, but the data provide evidence of impurities in the MgO. The spectrum includes signals at $g = 2.0073$ and 2.0180 which match reported signals of the carbonate radical, $\text{CO}_3^{\cdot-}$ (Meguro and Ikeya, 1993; Shpak et al., 2003). The signal at $g = 1.9804$, including a very weak quartet (coupling constant, $A = 18$ G) (Figure 5.1B), matches the g value of chromium, reported at $g = 1.9804$ (Biasia and Grillo, 2004). The quartet corresponds to ^{53}Cr (the natural abundance of this isotope is 9.3%), which has a nuclear spin I of $3/2$. A weak sextet of hyperfine lines with a coupling constant of 82.11 G attributed to Mn^{2+} species ($I = 5/2$) was also observed in this sample. These impurities are common in commercial MgO samples (Lange, 1975). The signal corresponding to oxygen radicals was not observed in the spectrum of this sample.

Evidence of the surface chemistry of the MgO is provided by the IR spectra. The spectrum of the calcined MgO (Figure 5.2, spectrum D) includes bands in the interval between 3730 and 3767 cm^{-1} , which are assigned on the basis of results reported by Diwald et al. (2002). The high-frequency (3767 cm^{-1}) component is assigned to OH groups in which the oxygen atom bonds to one surface cation (1-coordinated OH group), whereas the low-frequency component is assigned to OH groups in which the oxygen atom is coordinated with 3 to 5 cations (3, 4, and 5-coordinated OH group).

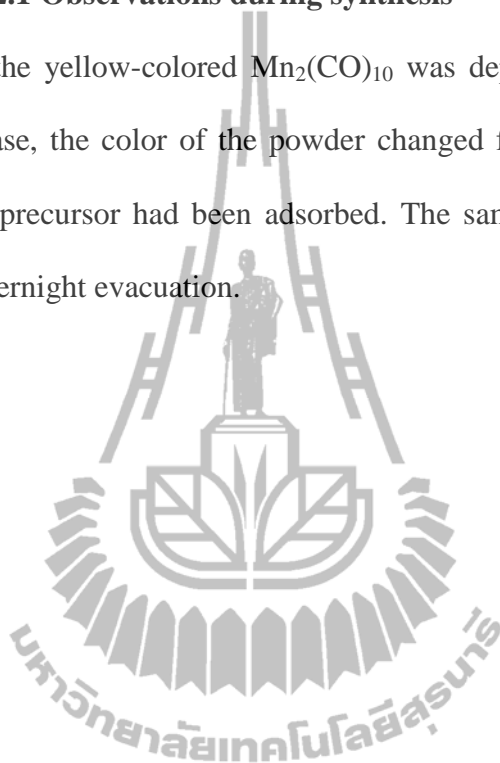
The carbonate region of the IR spectrum characterizing the calcined MgO (Figure 5.3, spectrum A) shows the presence of peaks at 1482 and 1422 cm^{-1} , which

are assigned to monodentate carbonate and carboxylate group, respectively (Hadjiivanov and Vayssilov, 2002).

5.3.2 Reaction of $\text{Mn}_2(\text{CO})_{10}$ with partially dehydroxylated MgO

5.3.2.1 Observations during synthesis

As the yellow-colored $\text{Mn}_2(\text{CO})_{10}$ was deposited onto MgO powder from the vapor phase, the color of the powder changed from white to pale yellow, indicating that the precursor had been adsorbed. The sample remained pale yellow after subsequent overnight evacuation.



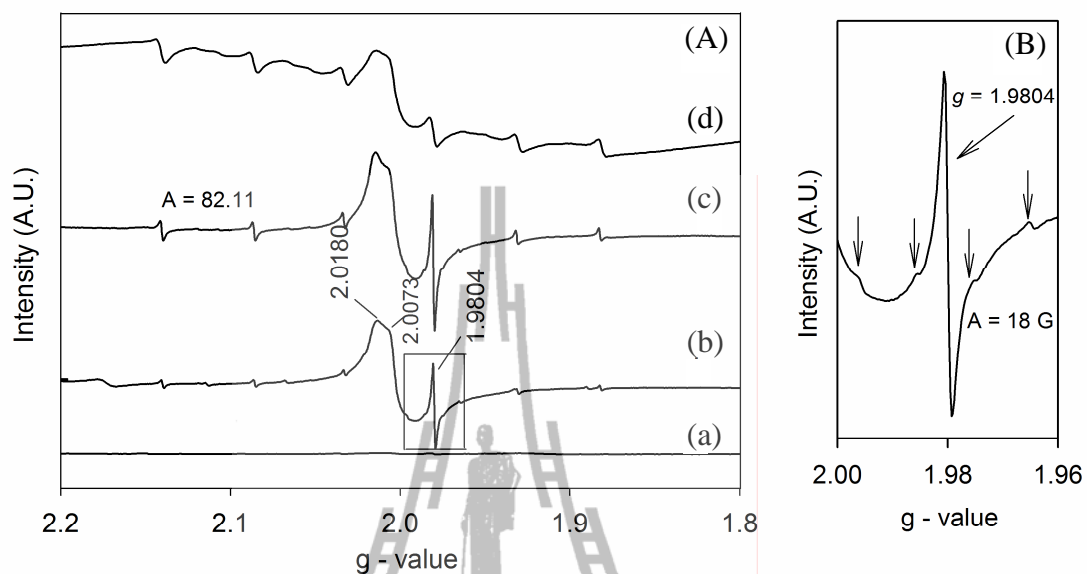


Figure 5.1 EPR spectra (A) of untreated MgO (a), MgO after treatment in O_2 at $400^\circ C$ followed by evacuation at the same temperature (b), sample prepared from $Mn_2(CO)_{10}$ on MgO (0.10 wt% Mn) (c), and sample prepared from $Mn_2(CO)_{10}$ on MgO (1.0 wt% Mn) (d) and (B) magnification of Figure 5.1A, spectrum b, at g equal to approximately 1.9804.

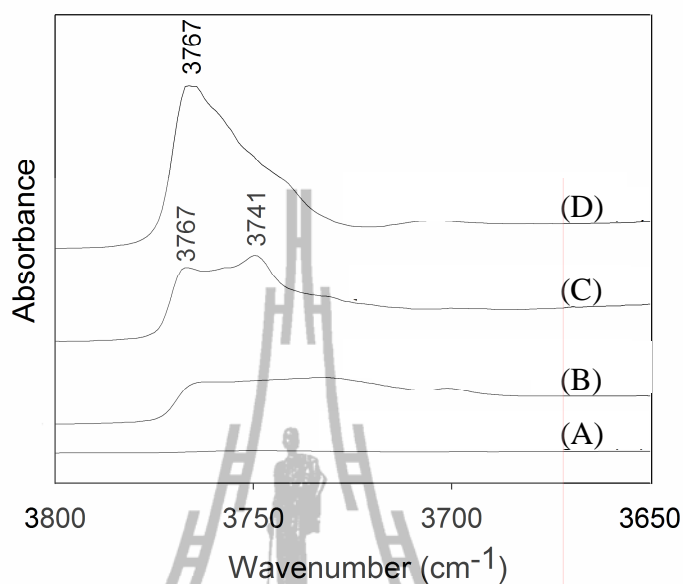


Figure 5.2 Normalized IR spectra in the ν_{OH} region characterizing samples prepared from $\text{Mn}_2(\text{CO})_{10}$ on MgO: the respective Mn contents (wt%) of the samples were 3.0 (A), 1.0 (B), 0.10 (C), and 0.0 (D). Spectra were normalized with respect to the carbonate band at 1264 cm^{-1} .

5.3.2.2 IR evidence of reactions of $\text{Mn}_2(\text{CO})_{10}$ with surface OH groups of MgO

When the manganese loading of the sample was only 0.10 wt%, the intensity of the band characteristic of the singly coordinated OH group (at 3767 cm^{-1}) decreased after the $\text{Mn}_2(\text{CO})_{10}$ had been adsorbed, but the intensity of the band at approximately 3741 cm^{-1} remained essentially unchanged (Figure 5.2, spectrum C). These results indicate that adsorption of $\text{Mn}_2(\text{CO})_{10}$ on MgO took place initially on the singly coordinated OH groups. The spectrum shows that this low loading of manganese was not sufficient to convert all the surface hydroxyl groups.

When the loading of manganese on the MgO was increased to 1.0 and then to 3.0 wt%, the intensities of both hydroxyl bands decreased, and they finally became unobservable (Figure 5.2, spectra B and A, respectively). Thus, when the manganese loading was 3.0 wt%, all the hydroxyl groups had reacted, and some of the precursor might have interacted with sites other than OH groups on the MgO.

5.3.2.3 IR evidence of reactions of $\text{Mn}_2(\text{CO})_{10}$ with surface CO_3^{2-} groups of MgO

When $\text{Mn}_2(\text{CO})_{10}$ was adsorbed on MgO, there was a decrease in intensity of the IR band at 1484 cm^{-1} (Figure 5.3, spectra A, B) assigned to monodentate carbonate (Hadjiivanov and Vayssilov, 2002) on MgO, and there was an increase in intensity of a band at 1393 cm^{-1} , assigned to carboxylates, relative to those at 1484 and 1422 cm^{-1} , which are not visible in the spectrum after adsorption (Hadjiivanov and Vayssilov, 2002). This result indicates that the $\text{Mn}_2(\text{CO})_{10}$ interacts weakly with the carbonate groups on MgO upon adsorption.

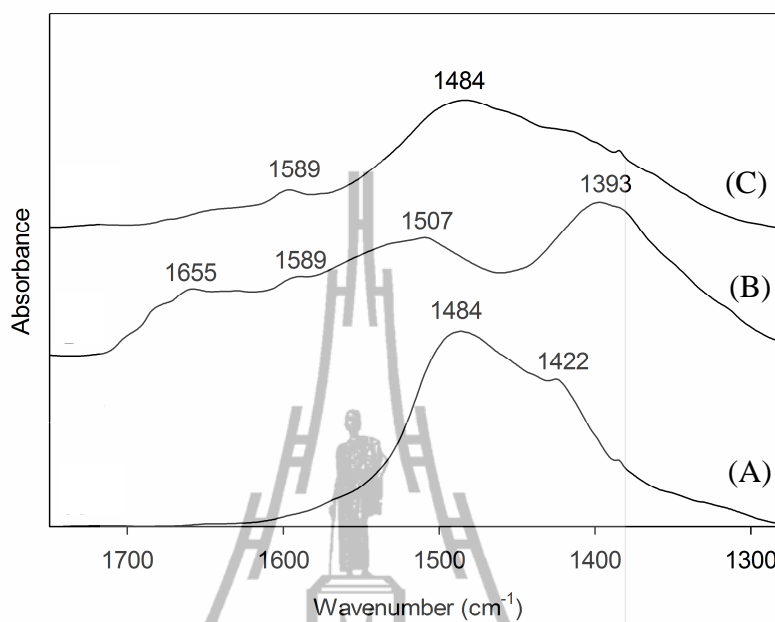


Figure 5.3 Normalized IR spectra in the carbonate region characterizing MgO (A), sample prepared from $\text{Mn}_2(\text{CO})_{10}$ on MgO (1.0 wt% Mn) (B), and after treatment in O_2 (C). The spectra were normalized by setting the value of the intensity of the strongest band in each spectrum equal to 1.0.

5.3.3 Characterization of sample containing 3.0 wt% Mn

5.3.3.1 IR Spectra

The interpretation of the IR spectra of the highly loaded sample is based on a comparison of the observed IR bands with those reported for a family of manganese carbonyl compounds, including $\text{Mn}_2(\text{CO})_{10}$ (Table 5.1). The spectrum characterizing the sample containing 3.0 wt% Mn includes two broad, intense bands, at 2050(m) and 2011(s) cm^{-1} (Figure 5.4, spectrum C). These bands essentially match those characterizing $\text{Mn}_2(\text{CO})_{10}$ in CH_2Cl_2 solution (Table 5.1 and Figure 5.4,

spectrum D). Furthermore, the spectrum also includes a shoulder at approximately 2029 cm^{-1} and a broad absorption extending from approximately 1889 to 1981 cm^{-1} . The similarity of the two intense bands to those in the spectrum of the precursor indicates that some of the $\text{Mn}_2(\text{CO})_{10}$ was adsorbed on MgO with its structure essentially intact; the data do not determine the degree of any aggregation of the $\text{Mn}_2(\text{CO})_{10}$ on the surface (thus, they do not determine whether it was molecularly dispersed). The broad lower-frequency absorption suggests the presence of adsorbed species other than $\text{Mn}_2(\text{CO})_{10}$, and our goal in investigating samples with lower loadings of $\text{Mn}_2(\text{CO})_{10}$ was to characterize these latter adsorbed species.

5.3.4 Characterization of sample containing 0.10 wt% Mn

5.3.4.1 IR spectra

The IR spectrum of the sample with the lowest manganese loading (0.10 wt%) (Figure 5.4, spectrum A) was markedly different from that of the sample with the high loading (and different from that of $\text{Mn}_2(\text{CO})_{10}$). The spectrum includes three intense bands, at $2029(\text{m})$, $1934(\text{s})$, and $1895(\text{m})\text{ cm}^{-1}$, which fall in the range reported for a number of manganese tricarbonyl compounds (Table 5.1). The data characterizing these manganese carbonyl compounds show that the positions of the carbonyl bands depend on the non-carbonyl ligands on the manganese. We therefore hypothesize that the adsorption of $\text{Mn}_2(\text{CO})_{10}$ took place by a reaction with hydroxyl groups of MgO formed manganese tricarbonyls with the support as a ligand.

Furthermore, the spectrum of the sample containing 0.10 wt% Mn (Figure 5.4, spectrum A) includes a weak shoulder at about 1869 cm^{-1} . By comparison with the spectra of manganese pentacarbonyls (Table 5.1), the shoulder might indicate the presence of manganese pentacarbonyls on the MgO surface.

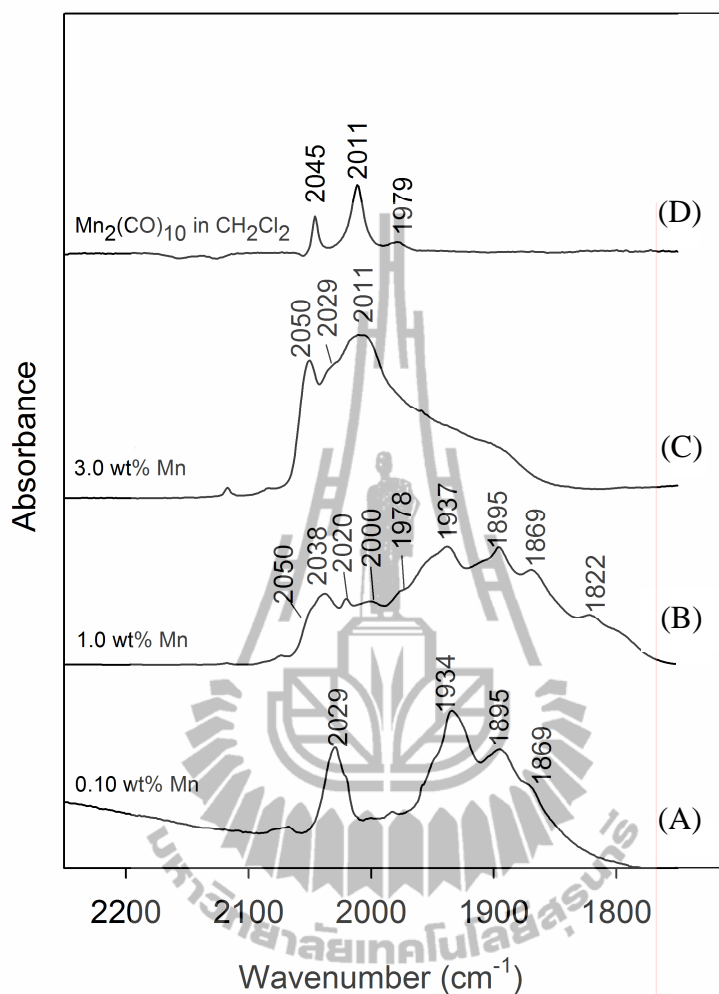


Figure 5.4 Normalized IR spectra in the ν_{CO} region characterizing a sample prepared from $\text{Mn}_2(\text{CO})_{10}$ on MgO : the respective Mn contents (wt%) of the samples were 0.10 (A), 1.0 (B), and 3.0 (C). Spectra A–C were normalized with respect to the carbonate band at 1264 cm^{-1} . Spectrum D corresponds to $\text{Mn}_2(\text{CO})_{10}$ in CH_2Cl_2 solution.

Manganese pentacarbonyls typically are characterized by a band at about 1898 cm^{-1} ; however, any peaks with frequencies near this would likely overlap bands of the manganese tricarbonyl species, and therefore we are not able to draw a

conclusion about the presence of manganese pentacarbonyls on the surface from this region of the spectra.

5.3.4.2 EPR spectroscopy

The EPR spectrum of the sample containing 0.10 wt% Mn (Figure 5.1, spectrum c) includes a signal at $g = 2.0015$ and a sextet of hyperfine lines with a coupling constant 82.11 G, which is characteristic of isolated Mn^{2+} (Mariscal et al., 1994). The spectrum of this sample also includes signals at $g = 2.0180$ and $g = 2.0073$, which correspond to CO^{3-} on MgO, which indicates that the decarbonation during the calcination was not completed. Furthermore, the signal characteristic of the chromium impurity in the MgO was still observed.

The presence of the Mn^{2+} signal demonstrates that the manganese was oxidized as it reacted with the MgO (the manganese in $\text{Mn}_2(\text{CO})_{10}$ is formally Mn^0), consistent with our IR evidence that $\text{Mn}_2(\text{CO})_{10}$ reacted with the MgO. We emphasize that this evidence of Mn^{2+} does not rule out the presence of manganese in other oxidation states that are not EPR active.

5.3.5 Characterization of sample containing 1.0 wt% Mn.

5.3.5.1 IR spectroscopy

The IR spectrum characterizing the sample prepared from $\text{Mn}_2(\text{CO})_{10}$ on MgO containing 1.0 wt% Mn (Figure 5.4, spectrum B) includes bands in the ν_{CO} stretching region, at 1822, 1869, 1895, 1937, 1978, 2000, 2020, 2038, and 2050 cm^{-1} . The locations of these bands differ from those of the bands characterizing $\text{Mn}_2(\text{CO})_{10}$ and the supported samples incorporating 0.10 and 3.0 wt% Mn. These IR bands are assigned to manganese carbonyl species, as follows: the bands at 2038(m), 1937(s), and 1895(s) cm^{-1} are in the range of those reported for manganese tricarbonyl

compounds, as summarized in Table 5.1. The band at 1869 cm^{-1} is characteristic of manganese pentacarbonyl compounds (Table 5.1). The small peak at about 1822 cm^{-1} could also correspond to a manganese pentacarbonyl, and some of the bands (at 2050, 2000, and 1978 cm^{-1}) correspond to $\text{Mn}_2(\text{CO})_{10}$ itself. Thus, we infer from the IR spectra that the sample prepared from $\text{Mn}_2(\text{CO})_{10}$ that contained 1.0 wt% Mn included a mixture of at least these three manganese carbonyl species, including unreacted precursor.

5.3.5.2 EPR spectroscopy

The EPR spectrum characterizing the sample containing 1.0 wt% Mn (Figure 5.1A, spectrum d) includes the sextet of hyperfine lines mentioned above (coupling constant = 82.11 G) that is characteristic of Mn^{2+} (Mariscal et al., 1994), along with signals at $g = 2.0180$ and $g = 2.0073$ corresponding to the $\text{CO}^{\cdot-}$ radical and the signal at $g = 1.9804$ characterizing the chromium impurity. Moreover, a broad base line was observed, which results from dipolar interactions (Mariscal et al., 1994). The presence of the base line in the spectrum suggests that the distance between Mn atoms in the sample containing 1.0 wt% Mn was significantly less on average than that in the sample containing 0.1 wt% Mn.

Table 5.1 ν_{CO} IR bands characterizing isolated and supported manganese carbonyl complexes.

Sample	Metal		ν_{CO} band position (cm^{-1})	Number of ν_{CO} bands	Refs.
	coor- dina- tion number	Number of Mn valence electrons			
$\text{Mn}_2(\text{CO})_{10}$ in CH_2Cl_2	6	18	2046(m) 2011(s) 1979(w)	3	This work
Sample formed from $\text{Mn}_2(\text{CO})_{10}$ on MgO and containing 0.1 wt% Mn (and represented as $\text{Mn}(\text{CO})_3(\text{O}_s)_3$)	N.A.	N.A.	2029(s) 1934(s) 1895(m)	3	This work
Sample formed from $\text{Mn}_2(\text{CO})_{10}$ on MgO and containing 1.0 wt% Mn (represented as $\text{Mn}(\text{CO})_3(\text{O}_s)_3$)	N.A.	16	2038(m) 1937(s) 1895(s)	3	This work

Table 5.1 ν_{CO} IR bands characterizing isolated and supported manganese carbonyl complexes (continued).

Sample	Metal		ν_{CO} band position (cm^{-1})	Number of ν_{CO} bands	Refs.
	coordination number	Number of Mn valence electrons			
Sample formed from $\text{Mn}_2(\text{CO})_{10}$ on MgO and containing 1.0 wt% Mn after O_2 treatment (and represented as $\text{Mn}(\text{CO})_3(\text{O}_s)_3$)	3	16	2042(s), 1947(s), 1905(s)	3	This work
$[\text{Mn}(\text{CO})_5]^-$ on MgO (inferred to be weakly interacting with surface)	5	18	1891, 1863	2	Keyes et al., 1989
$[\text{Mn}(\text{CO})_5]^-$ on MgO (inferred to be ion paired with Mg^{2+} sites)	5	18	2035, 1916, 1898, 1800	4	Keyes et al., 1989.
$\text{Mn}(\text{CO})_5\text{H}$ in tetrahydrofuran solution	6	18	2118(vw), 2016(vs), 2007(s)	3	Keyes et al., 1989.

Table 5.1 ν_{CO} IR bands characterizing isolated and supported manganese carbonyl complexes (continued).

Sample	Metal coordination number	Number of Mn valence electrons	ν_{CO} band position (cm^{-1})	Number of ν_{CO} bands	Refs.
$[\text{Mn}(\text{CO})_5]^-$ in tetrahydrofuran solution	5	18	1898, 1863	2	Keyes et al., 1989.
$\text{CH}_3\text{Mn}(\text{CO})_5$	6	18	2045(sh), 2024(vs), 2002(s,sh), 1961(w,sh)	4	Bulter et al., 1992.
$[\text{Mn}(\text{CO})_5\{\text{C}(\text{O})\text{O}(\text{C}_7\text{H}_{15})\}]$	6	18	2124(w), 2031(s), 2007(s)	3	Yin et al., 1998.
$[\text{Mn}(\text{CO})_3(\text{tripod})]^{+b}$	6	18	2030(s), 1962(s), 1902(ms), 1860(s)	4	Keyes et al., 1989.

Table 5.1 ν_{CO} IR bands characterizing isolated and supported manganese carbonyl complexes (continued).

Sample	Metal coordination number	Number of Mn valence electrons	ν_{CO} band position (cm^{-1})	Number of ν_{CO} bands	Refs.
$[\text{Mn}(\text{CO})_3(\text{PEt}_3)_3]^+$ $[\text{ClO}_4^-]$ in CH_2Cl_2 solution	6	18	2021(s), 1943(s)	2	Stiegman et al., 1986
$\text{Mn}(\text{CO})_3(\text{triphos})^{+c}$	6	18	2026(s), 1960(sh), 1945(s)	3	Stiegman et al., 1986
<i>mer,trans-</i> $[\text{MnBr}(\text{CO})_3$ $\{\text{P}(\text{C}_6\text{H}_4\text{Cl-4})_3\}_2]$	6	18	2033(w), 1951(vs), 1901(s)	3	Beckett et al., 2003
<i>mer,trans-</i> $[\text{MnBr}(\text{CO})_3\text{P}$ $(\text{CH}_2\text{C}_6\text{H}_4)_3\}_2]$	6	18	2031(w), 1945(vs), 1912(s)	3	Beckett et al., 2003
<i>mer,trans-</i> $[\text{MnBr}(\text{CO})_3$ $\{\text{P}(\text{C}_6\text{H}_4\text{O Me-4})_3\}_2]$	6	18	2031(w), 1946(vs), 1908(s)	3	Beckett et al., 2003

Table 5.1 ν_{CO} IR bands characterizing isolated and supported manganese carbonyl complexes (continued).

Sample	Metal coordination number	Number of Mn valence electrons	ν_{CO} band position (cm^{-1})	Number of ν_{CO} bands	Refs.
<i>fac,cis</i> - [MnBr(CO) ₃ (dppb)] ^d	6	18	2028(s), 1962(s), 1910(s)	3	Beckett et al., 2003
[Mn(CO) ₃ (3,5-DBCat)] ^e in CH ₂ Cl ₂ solution	5	16	1998(s), 1891(br)	2	Harlt, 1998
[Mn(CO) ₃ (3,5-DBCat)] ^e in CH ₂ Cl ₂ solution at 193 K	5	16	1998(s), 1894(s), 1883(s)	3	Harlt, 1998
[Mn(CO) ₃ (3,5-DBCat)(py)] ^f in pyridine solution	6	18	1995(s), 1885(s), 1862(s)	3	Harlt, 1998
[Mn(CO) ₃ (3,5-DBCat)(PPh ₃)] ^g in CH ₂ Cl ₂ solution	6	18	2001(s), 1904(s), 1867(s)	3	Harlt, 1998
[Mn(CO) ₃ (S,S-C ₆ H ₄)] ^h in THF solution	5	16	1996(s), 1887(s)	2	Lee et al., 1999

Table 5.1 ν_{CO} IR bands characterizing isolated and supported manganese carbonyl complexes (continued).

Sample	Metal coordination number	Number of Mn valence electrons	ν_{CO} band position (cm^{-1})	Number of ν_{CO} bands	Refs.
[Mn(CO) ₃ (S-C ₅ H ₄ -N)(S-C ₅ H ₄ N)]- in THF solution	6	18	1994(s), 1901(s), 1801(s)	3	Lee et al., 1999
[Mn(CO) ₃ (H ₂ O) ₃] ⁺	6	18	2051, 1944	2	Prinz et al., 2004
<i>fac</i> -MnBr(CO) ₃ [H(pzAn ^{Me})] ^h	6	18	KBr: 2029, 1923, 1902	3	Liddle et al., 2010
{ <i>fac</i> -Mn(CH ₃ CN)(CO) ₃ [H(pzAn ^{Me})] ^h } (PF ₆)	6	19	KBr: 2052, 1956, 1919	3	Liddle et al., 2010

Table 5.1 ν_{CO} IR bands characterizing isolated and supported manganese carbonyl complexes (continued).

Sample	Metal coordination number	Number of Mn valence electrons	ν_{CO} band position (cm^{-1})	Number of ν_{CO} bands	Refs.
$[\text{fac-Mn}(\text{CO})_3(\text{l-pzAn}^{\text{Me}})]_2^h$	6	19	KBr: 2002, 1905, 1884	3	Liddle et al., 2010
$(n\text{-Bu}_4\text{N})_2[\text{Mn}(\text{CO})_3(\text{H}_2\text{O})\{\text{Mo}_5\text{O}_{13}(\text{OMe})_4(\text{NO})\}]$	6	18	2029(s), 1933(s), 1916(s)	3	Villannn eau et al., 1982
$(n\text{-Bu}_4\text{N})_3[\text{Na}\{\text{Mo}_5\text{O}_{13}(\text{OMe})_4(\text{NO})\}_2]\cdot\text{Mn}(\text{CO})_3\cdot\text{MeOH}$	6	18	2036(s), 1930(s), 1920(s)	3	Villannn eau et al., 1982

Table 5.1 ν_{CO} IR bands characterizing isolated and supported manganese carbonyl complexes (continued).

Sample	Metal coordination number	Number of Mn valence electrons	ν_{CO} band position (cm^{-1})	Number of ν_{CO} bands	Refs.
$\text{Mn}(\text{CO})_3(\text{C}_5\text{H}_5)$	6	N.A.	2033,	2	Kläui et
$\text{Co}\{\text{P}(\text{O})\text{R}_2\}_3$			1920		al., 1985
$\text{Re}_2(\text{CO})_{10}$ in cyclohexane solution	6	18	2070, 2014, 1976	3	Purnell et al., 1994
$\text{Re}(\text{CO})_3\{\text{O-Mg}\}\{\text{OH-Mg}\}_2$	6	N.A.	2028, 1905, 1862	3	Kirlin et al., 1986

^aOs = Oxygen originating from the support.

^btripod = 1, 1, 1-tris((diphenylphosphino)methyl)ethane

^ctriphos = bis(2-(diphenylphosphino)ethyl)phenylphosphine

^ddppb = 1,4-bis(diphenylphosphino)butane

^e3,5-DBCat = 3,5-di-tert-butylcatecholate

^fPy = Pyridine

^gPPh₃ = Triphenylphosphine

^hH(pzAnMe) = 2-(pyrazolyl)-4-toluidine ligand

5.3.6 Characterization of sample containing 1.0 wt% Mn following treatment in H₂

5.3.6.1 IR spectra

The IR spectrum of the sample after treatment in flowing H₂ as the temperature was ramped to 700 °C lacks bands in the ν_{CO} region (Figure 5.5, spectrum C), indicating that all the carbonyl ligands had been removed.

5.3.6.2 EPR spectra

The EPR spectrum of this decarbonylated sample (Figure 5.6, spectrum C) is characterized by an intense sextet of hyperfine lines characteristic of Mn²⁺ species, with the intensity being greater than that characterizing the sample prior to treatment in H₂; evidently the treatment that led to decarbonylation of the manganese species affected the EPR signals, but the data do not determine the ligands replacing CO on the manganese and, as discussed below, they do not simply indicate a change in the amount of Mn²⁺ in the sample.

5.3.6.3 Mass spectra of effluent gas

As the sample was being treated in flowing H₂, mass spectra of the effluent gas were recorded (Figure 5.7). Consistent with the IR data demonstrating decarbonylation, the mass spectra of the effluent gas indicate the presence of CO in the effluent stream; furthermore, the effluent contained CO₂, CH₄, and CH₃ fragments presumably formed from CO, H₂, and possibly the support surface. As the temperature was ramped up, CO signals appeared at 128, 323, and 513 °C suggesting the presence of multiple surface manganese carbonyl species in the sample prior to treatment in H₂. The CO₂ signals appeared at temperatures higher than those characteristic of the CO, namely, at 200, 336, and 514 °C consistent with the

formation of CO₂ by reaction of CO. Furthermore, the signals representing CH₄ and CH₃ were observed at 205, 336, and 514 °C suggesting that they were also formed in reactions of CO and H₂.

5.3.7 Characterization of sample containing 1.0 wt% Mn following treatment in O₂

5.3.7.1 IR spectra in the ν_{CO} region

The sample containing 1.0 wt% Mn was treated in flowing O₂ at room temperature. The sample color changed from pale yellow to light brown after the treatment. The IR spectrum changed as a result of the treatment (Figure 5.5, spectra A and B). The bands representing the untreated sample corresponding to Mn₂(CO)₁₀ on MgO (at 2050(sh), 2000(m), and 1978(sh) cm⁻¹) and that corresponding to manganese pentacarbonyls (at 1869(m) cm⁻¹) were no longer observed; It can be inferred that these species were removed in the oxidative treatment. The resultant spectrum (Figure 5.5, spectrum B) includes only three bands in the ν_{CO} region (at 2042(s), 1947(s), and 1905(s) cm⁻¹), which are in agreement with ν_{CO} bands characteristic of manganese tricarbonyls (Table 5.1). These three bands shifted slightly to higher frequencies as a result of the O₂ treatment. The IR spectrum of this O₂-treated sample was simpler than that of the initial sample, suggesting the presence of more nearly uniform surface species; consequently, this sample was characterized by EXAFS spectroscopy.

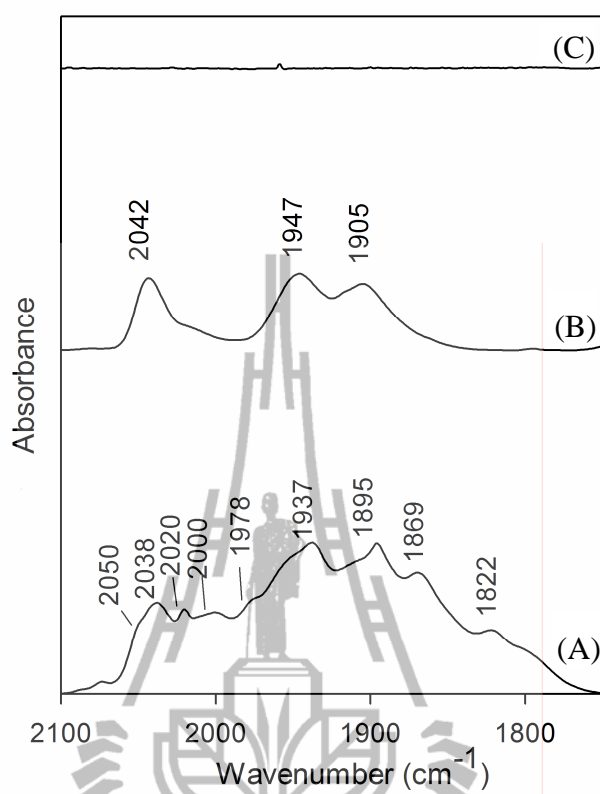


Figure 5.5 Normalized IR spectra in the ν_{CO} region of sample prepared from $\text{Mn}_2(\text{CO})_{10}$ and MgO (1.0 wt% Mn) (A), sample from spectrum A after treatment in flowing O_2 (B), and sample from spectrum A after decarbonylation (C).

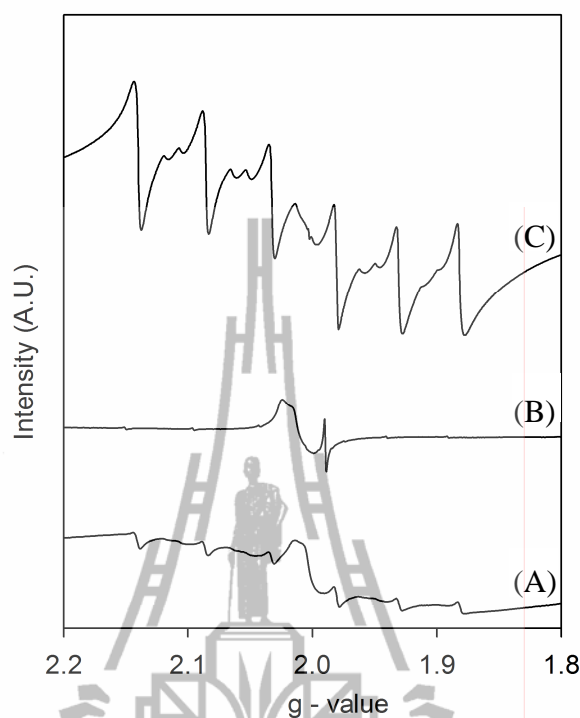


Figure 5.6 EPR spectra of sample prepared from $\text{Mn}_2(\text{CO})_{10}$ and MgO (1.0 wt% Mn) (A), sample from spectrum A after treatment in flowing O_2 (B), and sample from spectrum A after decarbonylation (C).

5.3.7.2 Mass spectra of effluent gas

The mass spectra characterizing the effluent gas during the O_2 treatment (Figure 5.7) indicate the presence of CO, demonstrating that carbonyl ligands in the sample were removed during the O_2 treatment.

5.3.7.3 IR spectra in carbonate region

The IR spectrum in the carbonate region representing the sample after the O_2 treatment (Figure 5.3, spectrum C) shows an increase in the intensity of the band associated with monodentate carbonate (at 1484 cm^{-1}). This result suggests that the O_2 treatment caused the formation of carbonate. Because the CO ligands attached

to the Mn atoms were the only carbon-containing species in the sample, it can be inferred that some of the CO was removed and reacted with O₂ and form carbonate groups adsorbed on the MgO. This inference is supported by the evidence of removal of CO during the treatment as observed by the mass spectra of the effluent.

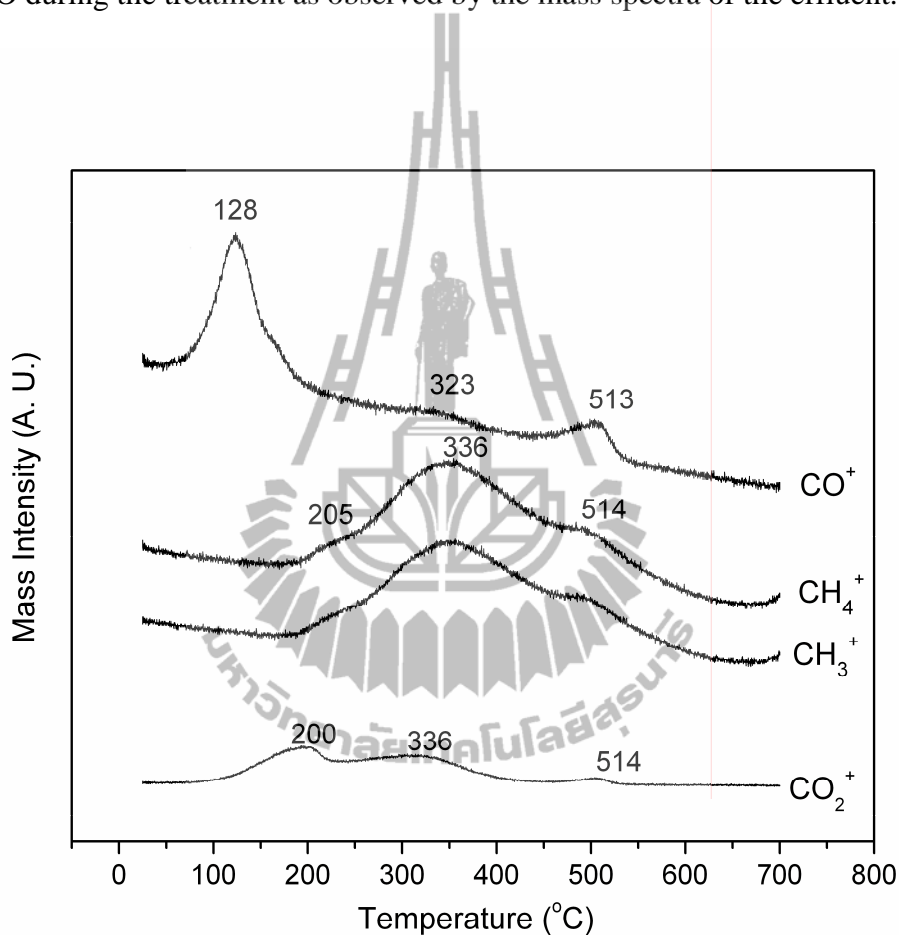


Figure 5.7 Mass spectra of the effluent gases formed by treatment of the sample prepared from Mn₂(CO)₁₀ on MgO (1.0 wt% Mn) in flowing H₂. The data were not normalized.

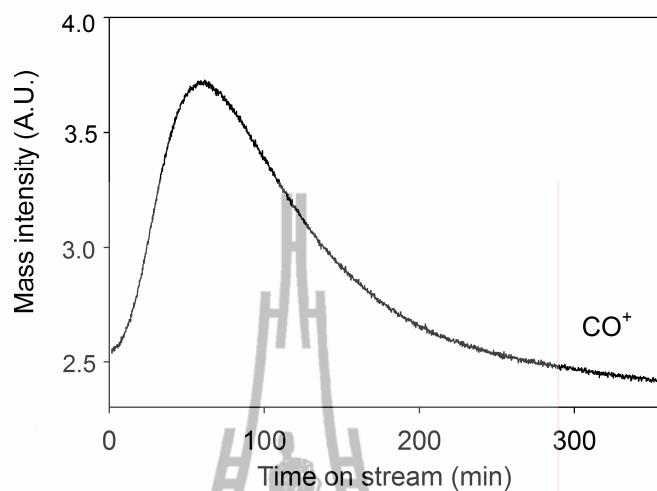


Figure 5.8 Mass spectrum: the CO^+ signal characterizing the effluent gas formed by treatment of the sample prepared from $\text{Mn}_2(\text{CO})_{10}$ on MgO (1.0 wt% Mn) in flowing O_2 at room temperature.

5.3.7.4 EPR spectra

The signal of sextet hyperfine lines corresponding to Mn^{2+} was still observed in the spectrum of the sample after the O_2 treatment (Figure 5.6, spectrum B), but its intensity was greatly reduced relative to that of the untreated sample (Figure 5.6, spectrum A), indicating that almost all of the Mn^{2+} had been converted; we infer that the manganese had been oxidized. Furthermore, the broad base line observed in the spectrum of the untreated sample was removed by the treatment, consistent with the inference that almost all the Mn^{2+} had been oxidized. These data are consistent with the IR spectra showing that the $\text{Mn}_2(\text{CO})_{10}$ and manganese pentacarbonyl species were converted by reaction with O_2 .

5.3.7.5 XANES spectra

The XANES spectrum characterizing the sample containing 1.0 wt% Mn after treatment in O₂ is shown in Figure 5.9. The spectrum shows a significant shift in the edge position (relative to that of metallic manganese) to higher energies, strongly suggesting that the manganese in the sample was cationic, in agreement with the EPR results and the treatment conditions. The edge shift of 9.7 eV is compared with the literature values determined by XANES of various manganese compounds, shown in Figure 5.10. The comparison provides a basis for estimating the oxidation state of manganese in the O₂-treated sample, but the comparison is open to question because of the inconsistency of the literature values of the edge energies. A comparison of our data with those of López et al. (2004) (Figure 5.10) indicates manganese in an oxidation state of approximately +5, whereas a comparison of our data with those of Stueben et al. (2004) indicates manganese in an oxidation state of approximately +3, and a comparison of our data with those of Campos et al. (2010) indicates manganese in an oxidation state of approximately +2 (Figure 5.10). We discount the third of these possibilities on the basis of our EPR data indicating that almost all the Mn²⁺ had been removed in the oxidative treatment.

5.3.7.6 EXAFS spectra

EXAFS data characterizing the sample containing 1.0 wt% Mn after O₂ treatment and the best-fit model are shown in Figure 5.11 (the plots for the other models are shown in appendix A). Each of the models that led to satisfactory fits included Mn–C, Mn–O*, and Mn–O_s, contributions, described below. An attempt was made to fit the data by including a Mn–Mn contribution, but no such contribution was found. The inclusion of a Mn–Mg contribution, although it gave a model with a

good fit, did not give an acceptable $(\Delta\chi)^2$ value. Details are presented in Appendix A. The fitting demonstrated that the data quality was less than excellent, and the k -range for which meaningful analysis could be done was limited to 3.08 to 9.50 \AA^{-1} .

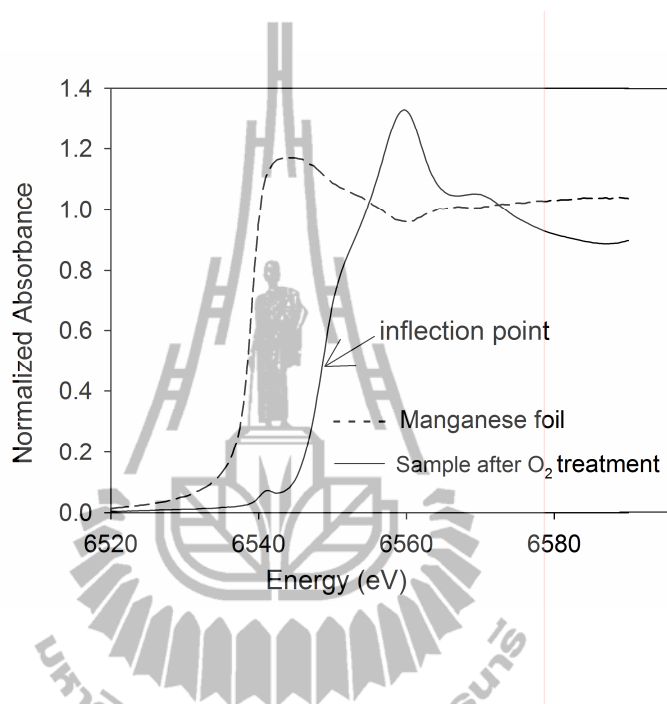


Figure 5.9 XANES spectra characterizing the sample prepared from $\text{Mn}_2(\text{CO})_{10}$ on MgO (1.0 wt% Mn), after O_2 treatment and manganese foil.

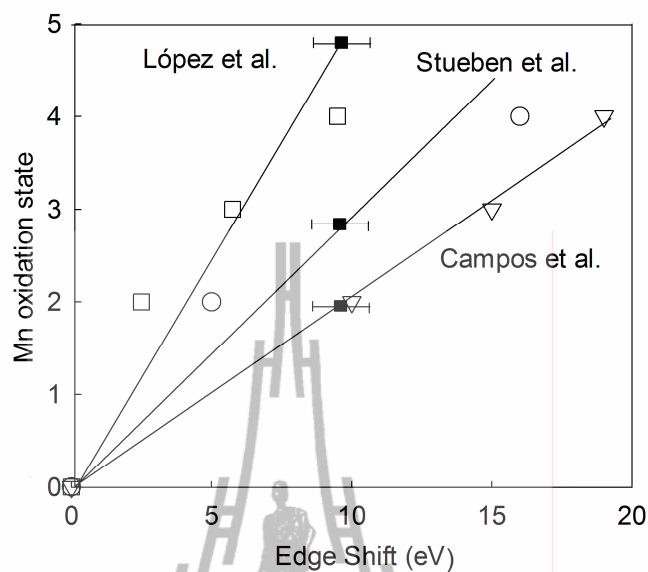


Figure 5.10 XANES calibration data and comparison with edge shift of supported manganese carbonyl species after treatment in O_2 . Literature data characterizing standard samples (including manganese foil and manganese oxides) as shown: \square , López et al.; \circ , Stueben et al.; ∇ , Campos et al.; \blacksquare , datum obtained in this work shown on each of the three lines to indicate the manganese oxidation state according to each of the three literature data sets.

Thus, the EXAFS fits that were found to be most appropriate included Mn–C, Mn–O*, and Mn–O_s contributions (Table 5.2). For each of these models, the results indicate Mn–C and Mn–O* contributions with coordination numbers of approximately 3, indicating manganese tricarbonyls, consistent with the IR spectra. A Mn–O_s contribution was consistently indicated, but, because the strong correlation between the coordination number and the Debye-Waller factor, it was not possible to discriminate between the models with Mn–O_s coordination numbers of approximately 1, 2, and 3 (for Models 1, 2, and 3, respectively (Table 5.2) The Mn–O_s distances in

each case were found to be close to 2.0 Å (Table 5.2). All three of these models provide satisfactory overall fits, but model 3 is preferred because the number of ligands and total valence electrons of manganese (18-electron rules) is the most likely possible (see the discussion part). The lack of Mn–Mn contributions is consistent with the presence of mononuclear manganese complexes.

In summary, the data indicate that the Mn–Mn bond in $\text{Mn}_2(\text{CO})_{10}$ had been cleaved, resulting in mononuclear manganese species, and these cationic complexes are well approximated as manganese tricarbonyls.

5.4 Discussion

5.4.1 Reaction of $\text{Mn}_2(\text{CO})_{10}$ with MgO

The data clearly demonstrate that $\text{Mn}_2(\text{CO})_{10}$ reacted with OH groups and CO_3^{2-} on the MgO surface and thus that the deposition led to some chemisorption. The IR spectra characterizing the resultant supported manganese carbonyls can be compared with the results of Keyes et al. (1989), who also used vapor deposition of $\text{Mn}_2(\text{CO})_{10}$ to prepare MgO-supported samples. Their support was a pressed 0.3-mm-thick wafer that was thin enough for transmission IR spectroscopy; it had been pretreated at 400°C, as had our MgO. Keyes et al. (1989) observed ν_{CO} spectra as the $\text{Mn}_2(\text{CO})_{10}$ deposition was taking place, presenting results that they interpreted as evidence of adsorption combined with breaking of Mn–Mn bonds and decarbonylation. Specifically, they observed bands at 2052, 2000, and 1978 cm^{-1} (among others), in good agreement with the bands in this work at 2050(sh), 2000(m), and 1978(sh) cm^{-1} , for example. They inferred the presence of $\text{Mn}_2(\text{CO})_{10}$ itself, of $[\text{Mn}(\text{CO})_5]^-$, and of $\text{Mn}(\text{CO})_x(\text{O}_s)_{6-x}$ ($x = 2-4$), in broad agreement with data and

interpretation in this work. However, the manganese loadings in the samples of Keyes et al. (1989) were not reported, any role of surface hydroxyl groups was overlooked, and the surface species generally consisted of complicated mixtures, in contrast to what we observed after treatment of our sample in O₂ or the samples made by adding only small amounts of Mn₂(CO)₁₀ to the MgO.

The oxidative fragmentation of Mn₂(CO)₁₀ in our work is in line with the chemistry of Mn₂(CO)₁₀ in solutions of nitrogen- and oxygen-donor ligands reported by Stiegman and Tyler (1984). They observed that disproportionation and decarbonylation of Mn₂(CO)₁₀ occurred with 1,2-bis(dimethylphosphino)ethane (dppe) or bis-(2-(diphenylphosphino)ethyl)phenylphosphine (triphos), to give products including [Mn(CO)₅]⁻ and [Mn(CO)_xL_{6-x}]ⁿ⁺ where x = 0–4 and L is a ligand.

The EPR evidence of Mn²⁺ in the initially prepared sample in this work indicates that manganese in the precursor Mn₂(CO)₁₀ was oxidized as a result of the chemisorption on MgO. It can be proposed that the surface hydroxyl groups on MgO, which the IR spectra show reacted with the Mn₂(CO)₁₀, were the oxidizing agents. There are other examples of the oxidation of metals on oxide supports by surface hydroxyl groups, exemplified by the oxidation of ruthenium-osmium clusters on γ-Al₂O₃ (Scott et al., 1981) and rhodium clusters on γ-Al₂O₃ (van't Blik et al., 1985).

Table 5.2 EXAFS parameters characterizing sample prepared from $\text{Mn}_2(\text{CO})_{10}$ supported on MgO (1.0 wt% Mn) after O_2 treatment^a.

Model Number	Absorber–backscatterer pair	N	R (Å)	$\Delta\sigma^2 \times 10^{-3}$	ΔE_0 (eV)	$(\Delta\chi)^2$ ^b
				(Å ⁻²)		
1	Mn–C	3.2	1.93	9.0	6.3	107
	Mn–O*	3.0	3.29	12.1	6.3	
	Mn–Os	1.1	2.05	10.0	2.7	
2	Mn–C	2.7	1.92	7.8	3.9	122
	Mn–O*	3.0	3.33	11.9	3.9	
	Mn–Os	1.8	2.00	10.5	8.9	
3	Mn–C	3.2	1.90	10.4	3.4	140
	Mn–O*	3.2	3.33	12.6	3.4	
	Mn–Os	2.6	1.98	13.8	9.9	

^a*Notation:* N , coordination number; R , distance between absorber and backscatterer atoms; $\Delta\sigma^2$, sigma-squared value (disorder term); ΔE_0 , inner potential correction; O*, oxygen of carbonyl group; Os, oxygen atom of MgO. In the fitting, the ΔE_0 values for Mn–C and Mn–O were constrained to be equal. Typical errors: N , $\pm 20\%$; R , ± 0.04 Å; $\Delta\sigma^2$, $\pm 20\%$; ΔE_0 , $\pm 20\%$.

^b $(\Delta\chi)^2$ is a measure of the quality of the fit, as defined in elsewhere (International XAFS Society, www, 2010).

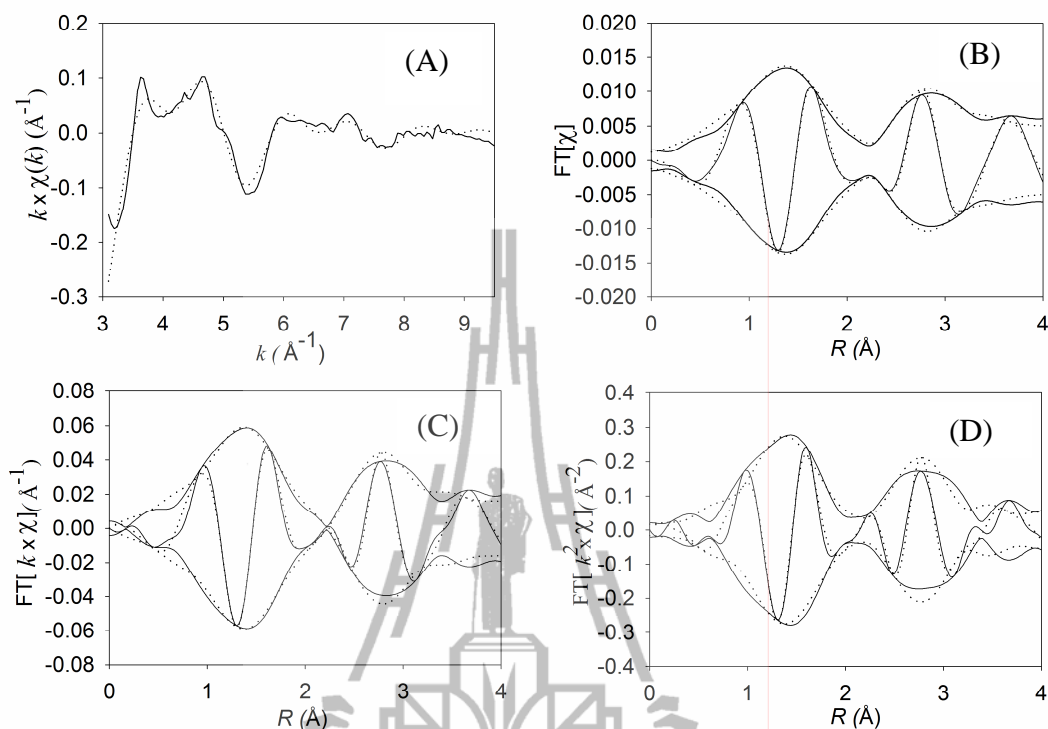


Figure 5.11 EXAFS data characterizing sample prepared from $\text{Mn}_2(\text{CO})_{10}$ on MgO (1.0 wt% Mn) after O_2 treatment (— ; data, best-fit according to model 3): k -weighted EXAFS function in k -space (A); imaginary part and magnitude of EXAFS function in R -space with FT k^0 -weighting (B), FT k^1 -weighting (C), and FT k^2 -weighting (D).

5.4.2 Oxidation of initially prepared supported manganese carbonyls

The oxidative treatment at room temperature led to conversion of the surface manganese carbonyls, as shown by the change in the IR spectrum and by the formation of gas-phase products (such as CO and CH_4) observed by mass spectrometry. The EPR data show clearly that the divalent manganese was removed, evidently by oxidation.

The XANES data show that the manganese was in an oxidized state after the sample had been exposed to O₂. However, as a consequence of the inconsistency in the literature regarding the XANES edge position values (Figure 5.10), determination of the oxidation state(s) of Mn in our sample by XANES spectroscopy is not unequivocal.

To elucidate the state of the manganese, examination of the likely forms of the manganese complexes that are expected on the basis of the known organomanganese chemistry was performed. The most common (stable) complexes of manganese are 18-electron and 16-electron complexes (Shriver et al., 1990). We infer from the EPR data (and the treatment conditions) that the oxidation state of manganese was greater than +2. Thus, the number of bonding electrons supplied by the manganese must be less than 5, with the likely values being 2 or 4, corresponding to Mn⁵⁺ and Mn³⁺, respectively. On the basis of the EXAFS and IR data, the manganese complex in the oxidized sample was a manganese tricarbonyl, and this result was used in the following electron counting; the key complication is that the EXAFS data do not distinguish the Mn–O_s coordination numbers—the data are consistent with values of nearly 1, 2, and 3.

To proceed with the electron counting, the contradictory XANES data of Figure 5.10 were used to estimate the candidate oxidation state of the manganese. The XANES data of Campos et al. (2010) were ruled out because they indicate that the manganese in the oxidized sample was nearly Mn²⁺ (Figure 5.10), contradicting the EPR data.

If, instead, the data of López et al. (2004) were considered to be correct, then the comparison of XANES result in this work with their data would indicate that the

manganese had been oxidized to Mn^{5+} . Mn^{5+} complexes are d^2 complexes, and if the tricarbonyl of Mn^{5+} were six-coordinate (the Mn–O_s coordination number would be 3, which is consistent with the EXAFS data; each oxygen of the support is regarded as a two-electron donor), then the supported manganese complex would be a 14-electron complex. Because these are rare, this possibility was discounted. If the manganese tricarbonyl of Mn^{5+} were five-coordinate, it would be a 12-electron complex, which is even more unlikely and rejected.

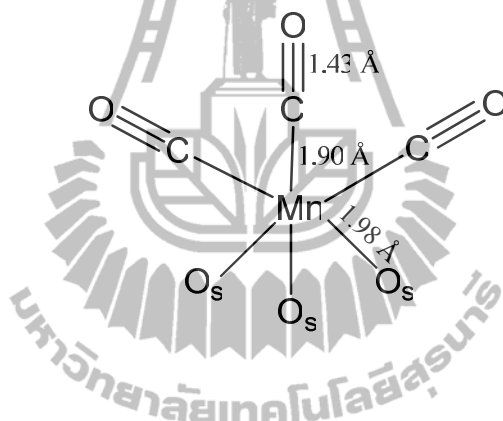
The remaining possibility is that the more reliable XANES standard data are those of Stueben et al. (2004). According to this possibility, the manganese in the oxidized sample would be nearly Mn^{3+} (Figure 5.10). Mn^{3+} complexes are common; these are d^4 complexes. If the tricarbonyl of Mn^{3+} were six-coordinate (the Mn–O_s coordination number would be 3, which is consistent with the EXAFS data; again, each oxygen of the support is regarded as a two-electron donor), then the supported manganese complex would be a 16-electron complex. Because these complex are common, this model is considered to be a highly likely possibility. Examples of six-coordinate d^4 complexes of manganese include the following (Cotton and Wilkinson, 1980): $\text{Mn}(\text{acac})_3$ (acac = acetylacetonato) and $[\text{Mn}(\text{C}_2\text{O}_4)_3]^{3-}$.

If the manganese tricarbonyl of Mn^{3+} were five-coordinate, it would be a 14-electron complex, which is highly unlikely and rejected.

Thus, it can be inferred that the supported manganese complex in the oxidized sample is a d^4 complex with three carbonyl ligands and bonded to MgO as a tridentate ligand. The structure is inferred to be closely comparable to one incorporating an oxometallate ligand that can be regarded as a model of an oxide surface; the corresponding compounds are $(n\text{-Bu}_4\text{N})_2[\text{Mn}(\text{CO})_3(\text{H}_2\text{O})\{\text{Mo}_5\text{O}_{13}(\text{OCH}_3)_4(\text{NO})\}]$

and $(n\text{-Bu}_4\text{N})_3[\text{Na}\{\text{Mo}_5\text{O}_{13}(\text{OMe})_4(\text{NO})\}_2\{\text{Mn}(\text{CO})_3\}_2]\cdot\text{MeOH}$ (Villanneau et al., 2003), which are formed by oxidation and decarbonylation of $\text{MnBr}(\text{CO})_5$ in solution by a route that is roughly similar to this work.

Correspondingly, it can be inferred that the most likely Mn–O_s coordination number is 3 and the probable structure of our supported manganese complex is as shown in Scheme 5.1, where the distances are those corresponding to the preferred EXAFS model 3.



Scheme 5.1 Proposed structure of surface manganese tricarbonyl species prepared from $\text{Mn}_2(\text{CO})_{10}$ on MgO (1.0 wt% Mn) after O_2 treatment; the distances are in Å, as determined by EXAFS spectroscopy for the preferred model 3.

The CO stretching frequencies of the sample that is inferred to be a manganese tricarbonyl appear at lower wavenumbers than those of $\text{Mn}_2(\text{CO})_{10}$. Although the oxidation state of manganese in the manganese tricarbonyl species (Mn^{3+}) is higher than that in $\text{Mn}_2(\text{CO})_{10}$ (Mn^0), the presence of the three surface oxygen atoms as ligands affects the stretching frequency of CO, which consequently shifts the CO bands to lower frequencies than those of $\text{Mn}_2(\text{CO})_{10}$. Correspondingly,

there are several examples of manganese tricarbonyl complexes with oxygen-containing ligands for which the ν_{CO} bands are at lower wavenumbers than those of $\text{Mn}_2(\text{CO})_{10}$ (Table 5.1). Examples in Table 5.1 include complexes with strong and weak back-bonding tendencies. An example is $\text{Mn}(\text{CO})_3(\text{C}_5\text{H}_5)\text{Co}\{\text{P}(\text{O})\text{R}_2\}_3$ (Kläui et al., 1985), which is characterized by ν_{CO} bands at 2033 and 1920 cm^{-1} . Moreover, this behavior is also observed in the rhenium tricarbonyl complexes (Kirlin et al., 1986; Purnell et al., 1994).

5.5 Conclusions

A sample prepared by vapor deposition of $\text{Mn}_2(\text{CO})_{10}$ on MgO was treated in flowing O_2 at room temperature to form a species shown by IR and EXAFS spectroscopies to be a manganese tricarbonyl and shown by EPR spectroscopy to incorporate manganese an oxidation state greater than +2. The EXAFS data and electron counting lead to the inference that the species is a d^4 complex bonded to three oxygen atoms of the MgO support as shown in Scheme 5.1.

5.6 References

Beckett, M. A., Brassington, D. S., Coles, S. J., Gelbrich, T., Light, M. E., and Hursthouse, M. B. (2003). A crystallographic and spectroscopic investigation of the stereochemistry of $[\text{MBr}(\text{CO})_3\text{L}_2]$ (M= Mn, Re) complexes: crystal and molecular structures of $[\text{MBr}(\text{CO})_3\text{L}_2]$ {M=Mn, L= $\text{P}(\text{C}_6\text{H}_4\text{Cl-4})_3$, 1/2dppe, 1/2dppf; M= Re, L= $\text{P}(\text{C}_6\text{H}_4\text{OMe-4})_3$, 1/2dppf}. **J. Organomet. Chem.** 688: 174-180.

- Biasia, R. S. and Grillo, M. L. N. (2004). ESR investigation of Cr^{3+} diffusion in MgO powders. **Solid State Commun.** 132: 107-108.
- Bulter, I. S., Gilson, D. F. R., and Lafleur, D. (1992). Infrared photoacoustic spectra of gaseous pentacarbonyl(methyl)manganese(I) and pentacarbonyl(methyl)rhenium(I). **Appl. Spectrosc.** 46: 1605-1607.
- Burch, R., Cruise, N., Gleeson, D., and Tsang, S. C. (1996). Surface-grafted manganese-oxo species on the walls of MCM-41 channels-a novel oxidation catalyst. **Chem. Commun.** 951-952.
- Campos, A., Lohitharn, N., Roy, A., Lotero, E., Goodwin, J. G., and Spivey, J. J. (2010). An activity and XANES study of Mn-promoted, Fe-based Fischer-Tropsch catalysts. **Appl. Catal. A-Gen.** 375: 12-16.
- Cotton, F. A. and Wilkinson, G. (1980). **Advanced Inorganic Chemistry: a Comprehensive Text.** New York: Wiley-Interscience.
- Dahl, L. F. and Rundle, R. E. (1963). The crystal structure of dimanganese decacarbonyl $\text{Mn}_2(\text{CO})_{10}$. **Acta Crystallogr.** 16: 419-426.
- Diwald, O., Sterrer, M., and Knözinger, E. (2002). Site selective hydroxylation of the MgO surface. **Phys. Chem. Chem. Phys.** 4: 2811-2817.
- Dossi, C., Fusi, A., Molteni, G., Recchia, S. and Psaro, R. (1997). Coupling diffuse reflectance fourier transform infrared spectrometry with gas chromatography (DRIFT-GC): a High-performance coupled technique for catalyst characterization. **Analyst.** 122: 279-282.
- Giebeler, L., Kießling, D., and Wendt, G. (2007). LaMnO_3 perovskite supported noble metal catalysts for the total oxidation of methane. **Chem. Eng. Technol.** 30: 889-894.

- Hadjiivanov, K. and Vayssilov, G. (2000). Characterization of oxide surfaces and zeolites by carbon monoxide as an IR probe molecule. **Adv. Catal.** 47: 307-511.
- Hartl, F. (1998). Nucleophilic attack at the five-coordinate anion $[\text{Mn}(\text{CO})_3(3,5\text{-di-tert-butylcatecholate})]^-$ controlled by electronic and steric effects. **Inorg. Chim. Acta.** 268: 1-11.
- International XAFS Society. (2010). **Error Reporting Recommendations: A report of the standard and criteria committee** [on-line]. Available: http://ixs.iit.edu/subcommittee_reports/sc/err-rep.pdf.
- Ishihara, A., Nomura, M., and Kabe, T. (1994). Hydrodesulfurization of dibenzothiophene catalyzed by alumina-supported ruthenium carbonyl complexes in a pressurized flow system. **J. Catal.** 150: 212-216.
- Jentoft, R. E., Deutsch, S. E., and Gates, B. C. (1996). Low-cost, heated, and/or cooled flow-through cell for transmission X-ray absorption spectroscopy. **Rev. Sci. Instrum.** 67: 2111-2112.
- Keyes, M. P., Gron, L. U., and Watters, K. L. (1989). Interactions of nickel and manganese carbonyls with oxide surfaces: formation of reduced, oxidized, and zerovalent metal species. **Inorg. Chem.** 28: 1236-1242.
- Kirlin, P. S., DeThomas, F. A., Bailey, J. W., Gold, H. S., Dybowski C., and Gates, B. C. (1986). Molecular oxide-supported rhenium carbonyl complexes: synthesis and characterization by vibrational spectroscopy. **J. Phys. Chem.** 90: 4882-4887.

- Kirilin, P. S., Knözinger, H., and Gates, B. C. (1990). Mononuclear, trinuclear, and metallic rhenium catalysts supported on magnesia: effects of structure on catalyst performance. **J. Phys. Chem.** 94: 8451-8456.
- Kläui, W., Okuda, J., Scotti, M., and Valderrama, M. (1985). Synthesis and characterization of manganese and rhenium tricarbonyl complexes with (*O,O,O*)-donor ligands. **J. Organomet. Chem.** 280: C26-C30.
- Koningsberger, D. C., Mojet, B. L., van Dorssen, G. E., and Ramaker, D. E. (2000). XAFS spectroscopy; fundamental principles and data analysis. **Top. Catal.** 10: 143-155.
- Lange, J. (1975). Strongly coupled impurities in MgO: Acoustic paramagnetic resonance of Fe²⁺ and Cr²⁺. **Phys. Rev. B: Condens. Matter Mater. Phys.** 12: 226-237.
- Lee, C. M., Lin, G. Y., Hsieh, C. H., Hu, C. H., Lee, G. H., Peng, S. M., and Liaw, W. F. (1999). A five-coordinate, sixteen-electron manganese(I) complex [Mn(CO)₃(S,S-C₆H₄)]⁻ stabilized by S,S π-donation from chelating [S,S-C₆H₄]²⁻. **J. Chem. Soc. Dalton Trans.** 2393-2398.
- Liddle, B. J., Wanniarachchi, S., Lindeman, S. V., and Gardinier, J. R. (2010). Tricarbonylrhenium(I) and manganese(I) complexes of 2-(pyrazolyl)-4-toluidine. **J. Organomet. Chem.** 695: 53-61.
- López, J. M. R., Lede, E. J., Requejo, F. G., Rodriguez, J. A., Kim, J. Y., Salas, R. R., and Domínguez, J. M. (2004). XANES Characterization of extremely nanosized metal-carbonyl subspecies (Me = Cr, Mn, Fe, and Co) confined into the mesopores of MCM-41 materials. **J. Phys. Chem. B** 108: 20005-20010.

- Mariscal, R., Soria, J., Pena, M. A., and Fierro, J. L. G. (1994). Features of Li-Mn-MgO catalysts and their relevance in the oxidative coupling of methane. **J. Catal.** 147: 535-543.
- Meguro, K. and Ikeya, M. (1993). Stabilization of superoxide and CO_3^- radicals through crystallization of CaCO_3 . **Jpn. J. Appl. Phys.** 32: 3540-3543.
- Niaei, A., Salari, D., Aghazadeh, F., Caylak, N., and Sepehrianazar, A. (2010). Catalytic oxidation of 2-propanol over (Cr,Mn,Fe)-Pt/ γ - Al_2O_3 bimetallic catalysts and modeling of experimental results by artificial neural networks. **J. Environ. Sci. Health, Part A: Toxic/Hazard. Subst. Environ. Eng.** 45: 454-463.
- Paganini, M. C., Murphy, D. M., Ferrari, A. M., Pacchioni, G., and Giamello, E. (1997). A combined EPR and quantum chemical approach to the structure of surface $\text{F}_s^+(\text{H})$ centers on MgO. **J. Phys. Chem. B** 101: 971-982.
- Papile, C. J., Knözinger, H., and Gates, B. C. (2000). $[\text{Re}_2(\text{CO})_9]^{2-}$ on hydroxylated MgO: Formation from $[\text{Re}_2(\text{CO})_{10}]$ and evidence of ion pairing at the surface. **Langmuir.** 16: 5661-5664.
- Pearson, W. B., Calvert, L. D., and Villars, P. (1985). **Pearson's Handbook of Crystallographic Data for Intermetallic Phases**; American Society for metals: Metals Parks. OH.
- Prinz, U., Koelle, U., Ulrich, S., Merbach, A. E., Maas, O., and Hegetschweiler, K. (2004). The organometallic *fac*- $[(\text{CO})_3\text{Mn}(\text{H}_2\text{O})_3]^+$ aquaion: base-hydrolysis and kinetics of H_2O -substitution. **Inorg. Chem.** 43: 2387-2391.
- Purnell, S. K., Xu, X., Goodman, D. W., and Gates, B. C. (1994). Adsorption and reaction of $[\text{Re}_2(\text{CO})_{10}]$ on ultrathin MgO films grown on a Mo(110) surface:

characterization by infrared reflection-absorption spectroscopy and temperature-programmed desorption. **J. Phys. Chem.** 98: 4076-4082.

Rainer, D. R. and Goodman, D. W. (1998). Metal clusters on ultrathin oxide films: model catalysts for surface science studies. **J. Mol. Catal. A: Chem.** 131: 259-283.

Ravel., B. and Newville, M. (2005). ATHENA, ARTEMIS, HEPHAESTUS: data analysis for X-ray absorption spectroscopy using IFEFFIT. **J. Synchrotron Radiat.** 12: 537-541.

Rehr, J. J. and Albers, R. C. (2000). Theoretical approaches to X-ray absorption fine structure. **Rev. Mod. Phys.** 72: 621-654.

Sayers, D. E., Stern, E. A., and Lytle, F. W. (1971). New technique for investigating nanocrystalline structures: fourier analysis of the extended X-ray absorption fine structure. **Phys. Rev. Lett.** 27: 1204-1207.

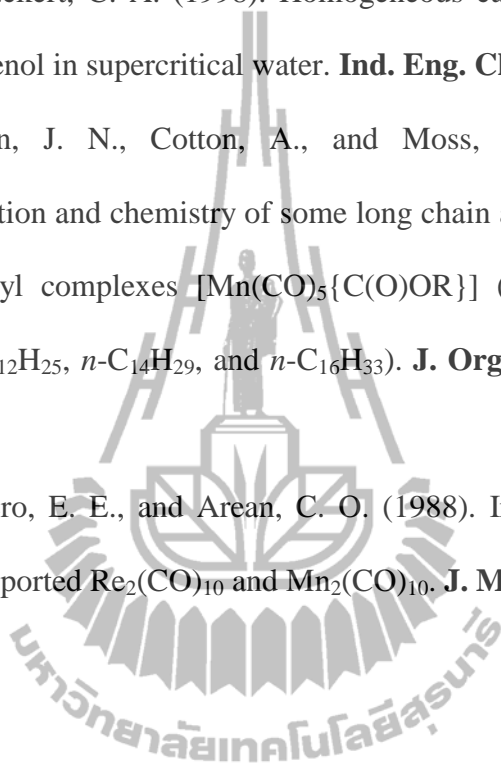
Scott, J. P., Budge, J. R., Rheingold, A. L., and Gates, B. C. (1981). Molecular chemistry of bimetallic clusters on the basic γ -Al₂O₃ surface: synthesis, reactivity, and catalytic activity of [H₃RuOs₃(CO)₁₂]⁻ {Al} and related structures. **J. Am. Chem. Soc.** 109: 7736-7744.

Shpak, A. P., Kalinichenko, E. A., Lytovchenko, A. S., Kalinichenko, I. A., Legkova, G. V., and Bagmut, N. N. (2003). The effect of γ -irradiation on the structure and subsequent thermal decomposition of brucite. **Phys. Chem. Miner.** 30: 59-68.

Shriver, D. F., Atkins, P. W., and Langford, C. H. (1990). **Inorganic Chemistry.** Oxford: Oxford University Press.

- Stiegman, A. E. and Tyler, D. R. (1984). Mechanism of the photochemical disproportionation reaction of $\text{Mn}_2(\text{CO})_{10}$ nitrogen donor ligands. **Inorg. Chem.** 23: 527-529.
- Stiegman, A. E., Goldman, A. S., Philbin, C. E., and Tyler, D. R. (1986). Photochemical disproportionation of $\text{Mn}_2(\text{CO})_{10}$ nineteen-electron intermediates and ligand and intensity dependence. **Inorg. Chem.** 25: 2976-2979.
- Stueben, B. L., Cantrelle, B., Sneddon, J., and Beck, J. N. (2004). Manganese K-edge XANES studies of Mn speciation in Lac des Allemands as a function of depth. **Microchem. J.** 76: 113-120.
- Vaarkamp, M., Linders, J. C., and Koningsberger, D. C. (1995). A new method for parameterization of phase shift and backscattering amplitude. **Physica B.** 209: 159-160.
- van't Blik, H. F. J., van Zon, J. B. A. D., Huizinga, T., Vis, J. C., Koningsberger, D. C., and Prins, R. (1985). Structure of rhodium in an ultradispersed $\text{Rh}/\text{Al}_2\text{O}_3$ catalyst as studied by EXAFS and other techniques. **J. Am. Chem. Soc.** 107: 3139-3147.
- Vartzouma, C., Evaggellou, E., Sanakis, Y., Hadjiliadis, N., and Louludi, M. J. (2007). Alkene epoxidation by homogeneous and heterogenised manganese(II) catalysts with hydrogen peroxide. **J. Mol. Catal. A: Chem.** 263: 77-85.
- Villanneau, R., Proust, A., Robert, F., and Gouzerh, P. (1982). Coordination chemistry of the soluble metal oxide analogue $[\text{Mo}_5\text{O}_{13}(\text{OCH}_3)_4(\text{NO})]^{3-}$ with manganese carbonyl species. **Chem.-Eur. J.** 9: 1982-1990.

- Yang, F., Chen, M. S., and Goodman, D. W. (2009). Sintering of Au particles supported on TiO₂(110) during CO oxidation. **J. Phys. Chem. C** 113: 254-260.
- Yang, H. H. and Eckert, C. A. (1998). Homogeneous catalysis in the oxidation of *p*-Chlorophenol in supercritical water. **Ind. Eng. Chem. Res.** 27: 2009-2014.
- Yin, X., Andersen, J. N., Cotton, A., and Moss, J. R. (1998). Synthesis, characterization and chemistry of some long chain alkoxy carbonyl manganese pentacarbonyl complexes [Mn(CO)₅{C(O)OR}] (where R= *n*-C₇H₁₅ to *n*-C₁₀H₂₁, *n*-C₁₂H₂₅, *n*-C₁₄H₂₉, and *n*-C₁₆H₃₃). **J. Organomet. Chem.** 564: 267-276.
- Zecchina, A., Platero, E. E., and Arean, C. O. (1988). Infrared characterization of alumina-supported Re₂(CO)₁₀ and Mn₂(CO)₁₀. **J. Mol. Catal.** 45(3): 373-379.



CHAPTER VI

ADSORPTION OF MANGANESE CARBONYLS

$\text{Mn}(\text{CO})_5\text{H}$ AND $\text{Mn}(\text{CO})_5\text{CH}_3$ ON PARTIALLY DEHYDROXYLATED MgO

Abstract

This chapter is a report of the preparation and characterization of manganese carbonyl complexes supported on MgO . A family of MgO -supported manganese carbonyl complexes was prepared by chemical vapor deposition of mononuclear manganese carbonyls, $\text{Mn}(\text{CO})_5\text{H}$ and $\text{Mn}(\text{CO})_5\text{CH}_3$, on partially dehydroxylated, high-area MgO powder. The resultant supported samples were treated in flowing O_2 to produce highly uniform surface species. Characterization of the samples by infrared, electron paramagnetic resonance, and X-ray absorption spectroscopies showed that the adsorption of $\text{Mn}(\text{CO})_5\text{H}$ on MgO produced a mixture of manganese pentacarbonyl and manganese tricarbonyl species with manganese in a cationic form. Treatment of this sample in flowing O_2 resulted in the disappearance of manganese pentacarbonyl species, allowing the formation of manganese tricarbonyl in high yield. In contrast, the adsorption of $\text{Mn}(\text{CO})_5\text{CH}_3$ on MgO led to a surface-bound manganese tetracarbonyl, with manganese in a cationic form; this sample was stable in O_2 .

6.1 Introduction

Supported transition metal complexes, a well-investigated and widely applied class of catalyst, consist of metal complexes dispersed on high-area porous supports that are usually metal oxides (Hlatky, 2000; Yoneda et al., 2001). The catalytic activity of a supported metal complex is affected by the metal, the ligands bonded to it, the support (which may also be a ligand) (Tai et al., 2009), and the oxidation state of the metal. Determinations of the properties of supported metal complexes are usually based on spectroscopic characterizations, but interpretation of the spectra is often challenging because of the nonuniformity of the support surface and the species bonded to it (Schneider et al., 1984). Combinations of complementary spectroscopic methods are usually required for a good structure determination, and interpretation of the spectra is facilitated when the synthesis of the surface species is precise and the surface species are as uniform as possible.

To goal of synthesizing supported metal complexes that are nearly uniform motivates the choice of the precursor. It is helpful to use precursors with well-defined structures and reactive ligands—thus, organometallic complexes (Chotisuwan et al., 2006; Psaro and Recchia, 1998). Metal complexes with carbonyl ligands are especially useful because the CO ligands allow tracking of the surface chemistry by infrared (IR) and complementary spectroscopies. For example, the adsorption of $\text{Fe}(\text{CO})_5$ on dehydroxylated MgO led to a mononuclear surface species represented as $[(\text{CO})_4\text{Fe}(\text{CO}_2)]^{2-}\{\text{Mg}^{2+}\}$ (where the brace represents groups on the support surface) (Guglielminotti and Zecchina, 1984). The chemisorption of $\text{H}_2\text{Os}(\text{CO})_4$ on MgO produced species represented as $\{\text{O}^{2-}\}\cdots\text{H}(\text{CO})_3\text{OsHCO}\cdots\{\text{Mg}^{2+}\}$ (Lamb and Gates,

1986). The reaction between $\text{Re}(\text{CO})_5\text{H}$ and MgO resulted in surface species represented as $[\text{Re}(\text{CO})_5]^- \cdots \text{H}^+ \{\text{MgO}\}$ (Kirlin et al., 1990).

Beyond its value as a probe of structure of metal complexes, CO offers numerous other advantages in investigations of supported catalysts: (a) CO is a good electron-donor ligand that can stabilize metal centers while being small enough to allow coordinative saturation of the complexes, (b) CO is a reactive ligand that is an intermediate in a number of catalytic reactions and, (c) decarbonylation of supported metal complexes is often possible under mild conditions, so that metal carbonyls on supports may be precursors of metal complexes with a wide variety of ligands (Fierro-Gonzalez et al., 2006; Liang et al., 2009).

The chemistry of reactions of metal carbonyl complexes with metal oxide surfaces includes chemisorptions that involve partial decarbonylation of the precursor (Hugues et al., 1982), cleavage of metal–metal bonds (Purnell et al., 1994), adduct formation via a bridging CO ligand (Youngs et al., 1983), and replacement of carbonyl ligands with other ligands (Kirlin et al., 1990; Kirlin et al., 1986; Lobo-Lapidus and Gates, 2010) such as oxygen of the support surface. Furthermore, metal cluster formation (Kulkarni et al., 2009), and/or fragmentation of metal carbonyls (Bhirud et al., 2005) are also observed on metal oxide surfaces.

The supported metal carbonyl complexes that have been investigated most widely are those of Group-8 transition metals. Relatively little has been reported with complexes of transition metals in Group 7, most of that with rhenium (Kirlin et al., 1986; Papile et al., 2000; Kirlin et al., 1990). There are various routes to prepare metal carbonyl on metal oxide. Papile et al. (2000) found that reaction of $\text{Re}_2(\text{CO})_{10}$ and partially dehydroxylated MgO produced $[\text{Re}_2(\text{CO})_9]^{2-}$ as surface species.

Treatment of these species either in vacuum, He, or air led to the formation of rhenium subcarbonyl containing; $[\text{Re}(\text{CO})_3\{\text{OMg}\}_x\{\text{HOMg}\}_{3-x}]$ (Papile and Gates, 1992). On the other hand, the adsorption of $\text{H}_3\text{Re}_3(\text{CO})_{10}$ and $\text{Re}(\text{CO})_5\text{H}$ on MgO produced $[\text{H}_2\text{Re}_3(\text{CO})_{12}][\text{MgO}]$ and $\{\text{MgO}\}\text{H}^+\cdots[\text{Re}(\text{CO})_5]^-$, respectively. Treatment of both surface species under H_2 or He produced $\text{Re}(\text{CO})_3(\text{O-Mg})(\text{HOMg})_2$ (Kirlin et al., 1990).

Manganese has been relatively neglected, with only a few reports of supported complexes (Keyes et al., 1989; Khabuanchalad et al., 2010), although there are several attractive manganese carbonyl precursors available, including $\text{Mn}_2(\text{CO})_{10}$ (Ramallo-López et al., 2004; Dahl and Rundle, 1963), $\text{Mn}(\text{CO})_5\text{H}$ (Edgell et al., 1969), and $\text{Mn}(\text{CO})_5\text{Br}$ (Huang et al., 2000). In contrast to surface chemistry of $\text{Re}_2(\text{CO})_{10}$, the adsorption of $\text{Mn}_2(\text{CO})_{10}$ on MgO produced more than one surface species, which are physisorbed $\text{Mn}_2(\text{CO})_{10}$, manganese pentacarbonyl and manganese tricarbonyl. Treatment of these surface species in O_2 resulted in only one surface species, which is manganese tricarbonyl (Khabuanchalad et al., 2010). Furthermore, a solution of manganese complexes is also used as catalyst, for example, in the oxidation reactions (Ishii et al., 1999; Tagliatesta et al., 2006).

In our previous work, we found that binuclear complex, $\text{Mn}_2(\text{CO})_{10}$, oxidatively reacts on MgO to give mononuclear manganese carbonyl species, so we extend the investigation of supported manganese complexes prepared from mononuclear manganese carbonyls, $\text{Mn}(\text{CO})_5\text{CH}_3$ and $\text{Mn}(\text{CO})_5\text{H}$, to allow comparisons with the earlier work (Khabuanchalad et al., 2010). High-area MgO powder was chosen as the support because we expect the oxidation of $\text{Mn}(\text{CO})_5\text{CH}_3$ and $\text{Mn}(\text{CO})_5\text{H}$ on MgO surface as observed in the reaction of $\text{Mn}_2(\text{CO})_{10}$ and MgO.

The $\text{Mn}(\text{CO})_5\text{CH}_3$ and $\text{Mn}(\text{CO})_5\text{H}$ are highly volatile compounds that provide the opportunity to prepare supported samples by chemical vapor deposition (CVD)- thus, in the absence of any solvent and the complications resulting from solvent-support interactions.

Our goal was to identify the surface species formed from these precursors on MgO and to investigate the stability of the supported species in O_2 by using a set of complementary physical methods, including infrared (IR), electron paramagnetic resonance (EPR), and X-ray absorption spectroscopies (XAS).

6.2 Experimental

6.2.1 Synthesis of $\text{Mn}(\text{CO})_5\text{H}$

$\text{Mn}(\text{CO})_5\text{H}$ was synthesized by a method essentially matching that reported for the synthesis of $\text{Re}(\text{CO})_5\text{H}$ (Urbancic and Shapley, 1989). The starting material was $\text{Mn}(\text{CO})_5\text{Br}$ (Strem, 98%) (instead of $\text{Re}(\text{CO})_5\text{Br}$). Tetraglyme (Sigma-Aldrich, 99%), phosphoric acid (EMD Science, 85%), zinc dust (Fisher Scientific, 99%), and phosphorus pentoxide (Sigma-Aldrich, 98%) were used as received. All handling during the syntheses was carried out in an N_2 -filled glovebox (AMO-2032, Vacuum Atmospheres, with O_2 and moisture contents each <1.0 ppm). Standard Schlenk techniques were used to minimize exposure of the samples to air. The liquid $\text{Mn}(\text{CO})_5\text{H}$ (clear solution) formed in the synthesis was stored in a refrigerated air-tight flask with paraffin-sealed joints until it was used for the synthesis of the supported samples by CVD.

$\text{Mn}(\text{CO})_5\text{D}$ was also prepared as described above, except that all the glassware was treated with D_2O (Cambridge Isotope Laboratory, 99.9%) before use, and D_3PO_4 (Acros Organics, 85%) was used instead of H_3PO_4 .

The products $\text{Mn}(\text{CO})_5\text{H}$ and $\text{Mn}(\text{CO})_5\text{D}$ were authenticated by IR spectroscopy of the gas-phase compounds [$\nu_{\text{CO}} = 2033(\text{sh}), 2028(\text{s}), 2023(\text{sh})$ and $2018(\text{sh}) \text{ cm}^{-1}$ for $\text{Mn}(\text{CO})_5\text{H}$ and $\nu_{\text{CO}} = 2035(\text{sh}), 2029(\text{s}), 2024(\text{sh})$ and $2020(\text{sh}) \text{ cm}^{-1}$ for $\text{Mn}(\text{CO})_5\text{D}$], matching literature values (Edgell et al., 1969).

6.2.2 Synthesis of $\text{Mn}(\text{CO})_5\text{CH}_3$

$\text{Mn}(\text{CO})_5\text{CH}_3$ was synthesized by a route analogous to that reported for $\text{Re}(\text{CO})_5\text{CH}_3$ (Zybill, 1997). The starting material was $\text{Mn}_2(\text{CO})_{10}$ (Strem, 98.0%) (instead of $\text{Re}_2(\text{CO})_{10}$). Mercury (Quicksilver Products Inc.), sodium (Aldrich, 99%), anhydrous tetrahydrofuran (Aldrich, 99.9%), and methyl iodide (Acros Organics, 99%) were used without further purification. The synthesis and handling were performed with exclusion of air and moisture on a double-manifold Schlenk line. The C–H bonds and carbonyl groups of $\text{Mn}(\text{CO})_5\text{CH}_3$ (white solid) was confirmed by ^1H NMR (CD_2Cl_2) ($\delta = -0.09 \text{ ppm}$) (Zybill, 1997) and IR spectroscopy ($\nu_{\text{CO}} = 2111(\text{w}), 2009(\text{vs})$ and $1986(\text{w}) \text{ cm}^{-1}$) (Mahmooda et al., 2006), respectively.

6.2.3 Synthesis of MgO-supported sample from $\text{Mn}(\text{CO})_5\text{H}$

MgO powder (EMD Science, 98.0%, BET surface area approximately $70 \text{ m}^2/\text{g}$) was calcined by using the method described in Chapter V. In the glovebox, a flask containing the highly volatile, air-sensitive clear liquid $\text{Mn}(\text{CO})_5\text{H}$ was quickly connected to another flask containing calcined MgO powder via a glass tube equipped with a high vacuum valve and ground-glass joints. The section containing MgO was separated from the assembly containing $\text{Mn}(\text{CO})_5\text{H}$ by a high vacuum

valve. The apparatus was removed from the glovebox and connected to the Schlenk line. The flask containing the $\text{Mn}(\text{CO})_5\text{H}$ was placed in a dry-ice/acetone bath ($T \approx -55^\circ\text{C}$). When the $\text{Mn}(\text{CO})_5\text{H}$ was frozen, the system was evacuated for 15 min to remove N_2 , and then the high vacuum valve that was used to separate the MgO section from the $\text{Mn}(\text{CO})_5\text{H}$ section was opened for 30 min to allow the $\text{Mn}(\text{CO})_5\text{H}$ to sublime and deposit onto the MgO powder, which was being stirred in the adjoining flask. As the vaporized $\text{Mn}(\text{CO})_5\text{H}$ was deposited, the color of the powder changed from white to yellow (any exposure of this sample to air caused it to turn brown). The sample was evacuated overnight to remove physisorbed $\text{Mn}(\text{CO})_5\text{H}$ and stored in the glovebox. The amount of $\text{Mn}(\text{CO})_5\text{H}$ deposited on MgO can not be controlled because the $\text{Mn}(\text{CO})_5\text{H}$ precursor is highly volatile.

The MgO-supported $\text{Mn}(\text{CO})_5\text{D}$ sample was prepared in the same way as MgO-supported $\text{Mn}(\text{CO})_5\text{H}$ sample.

6.2.4 Synthesis of MgO-supported sample prepared from $\text{Mn}(\text{CO})_5\text{CH}_3$

Because $\text{Mn}(\text{CO})_5\text{CH}_3$, a white solid, is also highly volatile, it was deposited onto MgO by a procedure similar to that used for the deposition of $\text{Mn}(\text{CO})_5\text{H}$. After the apparatus had been assembled in the glovebox, it was taken out and connected to the Schlenk line; in this synthesis, the cold bath was dry-ice/isopropanol ($T \approx -25^\circ\text{C}$). Then the system was evacuated for 15 min and warmed to room temperature to allow sublimation of the $\text{Mn}(\text{CO})_5\text{CH}_3$. The masses of $\text{Mn}(\text{CO})_5\text{CH}_3$ and MgO were chosen to give a supported sample containing 1.0 wt% Mn. The sample was evacuated overnight and stored in the glovebox.

6.2.5 Treatments of supported samples

It was reported in Chapter V that treatment in flowing O_2 of MgO-supported samples prepared from $Mn_2(CO)_{10}$ resulted in nearly uniform surface manganese complexes. Hence, the MgO-supported samples prepared from $Mn(CO)_5H$ and from $Mn(CO)_5CH_3$ were treated in O_2 in a once-through quartz tubular flow reactor. Each powder sample (1.0 g) was loaded into the reactor in the glovebox; the sample was held by a frit mounted near the center of the tube, which was sealed on both ends by O-ring compression fittings. The reactor was removed from the glovebox, and then both ends of the reactor were connected to the flow system—without exposure of the sample to air. At room temperature, O_2 (0.1 bar) (Airgas, 10% by volume in helium) was fed to the reactor at a rate of 60 mL(NTP)/min for 6 h, and then the sample was flushed with flowing helium, and the reactor was sealed and returned to the glovebox. The effluent was analyzed with an online mass spectrometer.

6.2.6 Spectroscopic characterization of samples

6.2.6.1 IR spectroscopy

The partially dehydroxylated MgO and the samples prepared from $Mn(CO)_5H$ and $Mn(CO)_5CH_3$ supported on MgO (before and after O_2 treatment) were characterized with a Bruker IFS 66v IR spectrometer equipped with DTGS and HgCdTe detectors. In the glovebox, each sample was pressed between two KBr windows and placed in a gas-tight cell (International Crystal Laboratories, Garfield, NJ). The cell was then loaded into an airtight container. The container was removed from the glovebox and mounted in the spectrometer. Then the spectrometer sample chamber was evacuated immediately (pressure \approx 1 mbar), and the vacuum was maintained as the spectra were recorded at room temperature, in transmission mode,

with a resolution of 4 cm^{-1} . Each reported spectrum is the average of at least 128 scans.

6.2.6.2 EPR spectroscopy

The calcined MgO and the supported samples before and after O_2 treatment were characterized by EPR spectroscopy. Each sample in the N_2 -filled glovebox was loaded into a 4-mm O.D. quartz EPR tube and sealed with an Ultra-torr[®] fitting. The EPR tube was removed from the glovebox and evacuated (pressure $\approx 1 \times 10^{-3}$ mbar) for 30 min and then flame sealed. EPR data were collected at the CalEPR Center at the University of California, Davis, CA. Each sample was scanned at -223°C on a Bruker ECS 106 X-band (≈ 9.5 GHz) spectrometer equipped with a Bruker ER4102ST cavity operating in the TE_{102} mode. Measurements were performed with a microwave power of 10 mW, a field modulation of 0.2 mT at 100 kHz, and a sweep rate of 0.1 mT/s. Ten scans were accumulated for each reported spectrum.

6.2.6.3 X-Ray absorption spectroscopy

The supported samples before and after O_2 treatment were characterized by XAS. Data collection was performed at beamline 9-BM of the Advanced Photon Source (APS) at Argonne National Laboratory, Argonne, IL, and at beamline X-18B at the National Synchrotron Light Source (NSLS), Upton, NY. Each of the beamlines was equipped with a Si(111) double-crystal monochromator which was detuned by approximately 25-30% at the Mn K edge to minimize the effects of higher harmonics in the X-ray beam. The intensity of the X-rays entering and exiting the sample was measured with two gas-filled ion chambers, and a third ion chamber

was used to collect the spectrum of a manganese foil used as a reference for energy calibration.

The samples were loaded into a stainless-steel Eppenlost tube sealed with O-rings and transferred to the synchrotron, where it was handled in an N₂-filled glovebox. The O₂ and moisture contents of the glovebox at APS were 0.10 and 1.3 ppm, respectively, and the O₂ and moisture contents of the glovebox at NSLS were less than 1.0 ppm. The mass of each sample was calculated to provide an absorbance of about 2.5 to give a nearly optimized signal-to-noise ratio in the data.

The sample prepared from Mn(CO)₅H on MgO and treated in O₂ was weighed and pressed into a self-supporting wafer before it was loaded into the cell (Jentoft et al., 1996), which allowed scanning of the sample without exposure to air. The other samples were weighed, mixed with inert boron nitride powder (Aldrich, 98.0%, particle size \cong 1 μ m), packed into a stainless-steel plate, and then sealed with Kapton[®] tape. All the sample preparation steps were carried out in the glovebox to minimize the air exposure. The sample cell was transferred to the beam line and mounted between the first two ion chambers. Each sample was scanned at room temperature in transmission mode at the Mn K edge (6539 eV). Each reported spectrum is the average of at least four spectra.

6.2.7 Data analysis

6.2.7.1 EXAFS data analysis

EXAFS data analysis was conducted with a “difference file” technique (Koningsberger et al., 2000) by use of the software XDAP (Vaarkamp et al., 1995). The functions used to construct the structural models and minimize the error are shown elsewhere (Koningsberger et al., 2000). In the first step of the data analysis, all

scans of a given sample were aligned and averaged. Reference backscattering amplitudes were calculated by using the FEFF7.0 software (Rehr and Albers, 2000) from crystallographic data characterizing $\text{Mn}(\text{CO})_5\text{H}$ (Laplica et al., 1964) for representation of Mn–C and Mn–O* contributions (O* is carbonyl oxygen). The Mn–C–O moiety is characterized by collinear multiple scattering. $\text{Mn}_2(\text{CO})_{10}$ (Dahl and Rundle, 1963) was used as a reference for Mn–Mn contributions, and Mn_2O_3 (Pearson et al., 1985) and MnMg alloy (Pearson et al., 1985) were used as references for Mn–O_s (Mn–O_s refers to a relatively short Mn–O distance in supported samples incorporating oxygen of the support surface) and Mn–Mg contributions, respectively.

The data fitting was done in *R*-space (distance space) by using three *k*-weightings (k^0 , k^1 , and k^2). For a candidate model to be considered appropriate, it was required to fit satisfactorily with all the *k*-weightings. In the fitting with a candidate model, the parameters characterizing each contribution, the coordination number *N*, the $\Delta\sigma^2$ value (disorder term), the interatomic distance *R*, and the inner potential correction ΔE_0 were varied until an optimized fit was obtained for all *k*-weightings. The number of parameters used in the fitting did not exceed the statistically justified number calculated with the Nyquist theorem (Sayers et al., 1971). The multiple scattering in $\text{Mn}_2(\text{CO})_{10}$ calculated with FEFF7.0 was used to identify and fit the collinear Mn–C–O contributions.

Two criteria (International XAFS Society, www, 2010) were used to determine whether an EXAFS fit was satisfactory: first, analysis was done to determine whether the addition of each shell to the model improved the fit by decreasing the value of $(\Delta\chi)^2$, and, second, the parameters for each shell were

checked to determine whether they were physically appropriate. Specifically, the value of ΔE_0 was constrained to be in the range -10 to 10 eV, and the value of $\Delta\sigma^2$ was not to exceed $1.5 \times 10^{-2} \text{ \AA}^{-2}$.

6.2.7.2 XANES data analysis

Data in the X-ray absorption near edge structure (XANES) region were analyzed with the software package Athena (Ravel and Newville, 2005). The edge position of the manganese in each sample was taken as the inflection point in the measured X-ray absorption spectrum. The energy scale of the XAFS spectrum was calibrated by setting the edge position of the manganese foil to the reported value.

6.3 Results

6.3.1 Adsorption of $\text{Mn}(\text{CO})_5\text{H}$ and of $\text{Mn}(\text{CO})_5\text{CH}_3$ on MgO

6.3.1.1 Observations during synthesis

When either $\text{Mn}(\text{CO})_5\text{H}$, a clear liquid, or $\text{Mn}(\text{CO})_5\text{CH}_3$, a white solid, was deposited on MgO powder by CVD, the color of the powder changed from white to pale yellow, indicating that each of these complexes interacted with the MgO surface.

6.3.2 Characterization of initially prepared samples

6.3.2.1 IR spectroscopy

Spectra in ν_{OH} region

IR spectroscopy was used to characterize the OH groups on MgO. The spectrum of the MgO before deposition of a manganese complex (Figure 6.1a, spectrum A) includes an intense band at 3765 cm^{-1} , attributed to singly coordinated OH groups (with the oxygen atom bonded to only one surface cation) (Diwald et al.,

2002), as expected and consistent with the lack of complete dehydroxylation of the support. When $\text{Mn}(\text{CO})_5\text{H}$ was deposited on the support, the intensity of this band decreased substantially, showing that the OH groups reacted with the precursor.

To track the reactivity of the hydride ligands on $\text{Mn}(\text{CO})_5\text{H}$, a supported sample was prepared from the labeled compound $\text{Mn}(\text{CO})_5\text{D}$, and again, IR spectroscopy was used to characterize the resultant sample. The spectrum in the OH region includes a very weak band at 2774 cm^{-1} (Figure 6.1b), which is assigned to surface OD groups (Datka et al., 2003). These results demonstrate that the adsorption of $\text{Mn}(\text{CO})_5\text{D}$ on MgO involved not just its reaction with OH groups but also donation of a deuteron to surface oxygen atoms of the MgO, or replacement of OH groups by OD groups.

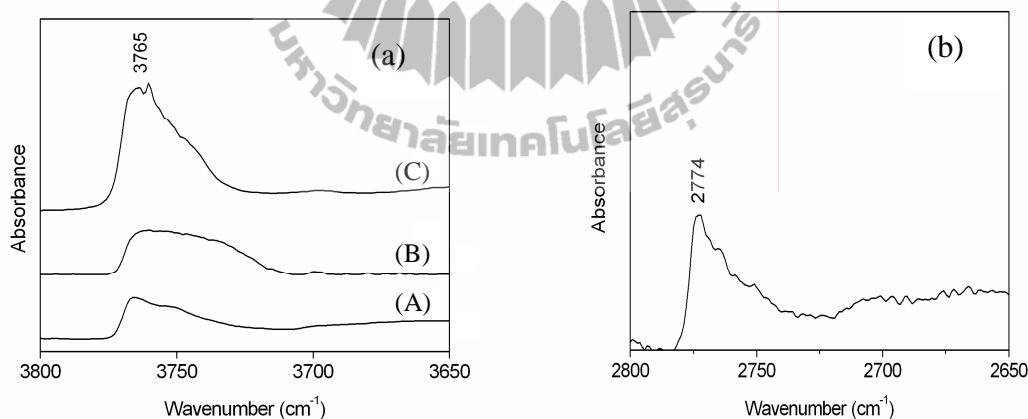


Figure 6.1 (a) IR spectra in the ν_{OH} region characterizing MgO (A); the sample prepared by CVD of the precursor $\text{Mn}(\text{CO})_5\text{H}$ on MgO (B); the sample prepared by treating the sample represented by spectrum B in O_2 at 25°C and $P_{\text{O}_2} = 0.1\text{ bar}$ (C); and (b) spectrum in the ν_{OD} region of characterizing the sample prepared from $\text{Mn}(\text{CO})_5\text{D}$ and MgO.

The IR spectrum of the sample prepared from $\text{Mn}(\text{CO})_5\text{CH}_3$ and MgO (Figure 6.2) shows a decrease in intensity of the band assigned to 1-coordinated OH groups on MgO, indicating a reaction of the precursor with these groups. The C–H stretching band observed for the precursor at 2984(w) and 2905(w) cm^{-1} (Mahmooda et al., 2006) was not observed in the spectrum of the supported species, suggesting that the CH_3 had been removed as a result of chemisorption.

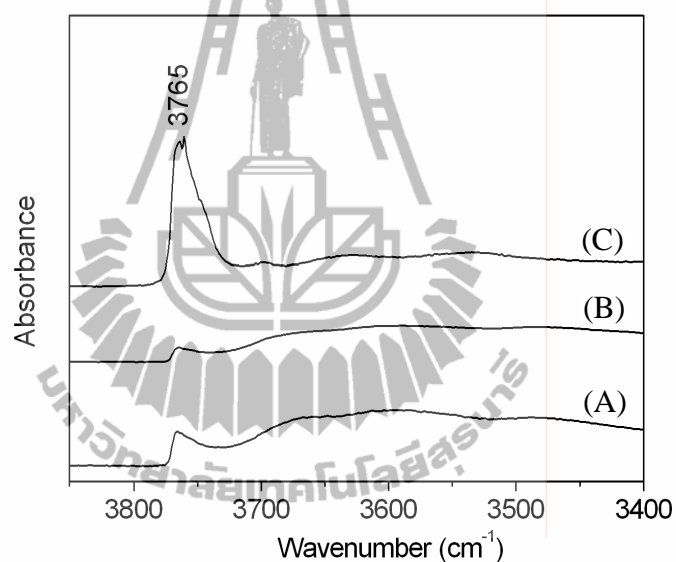


Figure 6.2 IR spectra in the ν_{OH} region of characterizing MgO (A), the sample prepared by CVD of $\text{Mn}(\text{CO})_5\text{CH}_3$ on MgO (1.0 wt% Mn) (B), and the sample prepared by treatment of the sample represented by spectrum (B) in O_2 at 25°C and $P_{\text{O}_2} = 0.1$ bar (C).

Spectra in ν_{CO} region

The ν_{CO} IR spectrum characterizing the sample prepared from $\text{Mn}(\text{CO})_5\text{H}$ and MgO includes bands at 2039(s), 2020(m), 1939(s), 1910(m), and 1870(w,sh) cm^{-1} . These frequencies are different from those of the precursor $\text{Mn}(\text{CO})_5\text{H}$ in the gas phase [2033(sh), 2028(s), 2023(sh), and 2018(sh) cm^{-1}] (Edgell et al., 1969), indicating that the precursor reacted with MgO and formed manganese carbonyl species that were not simply physisorbed precursors.

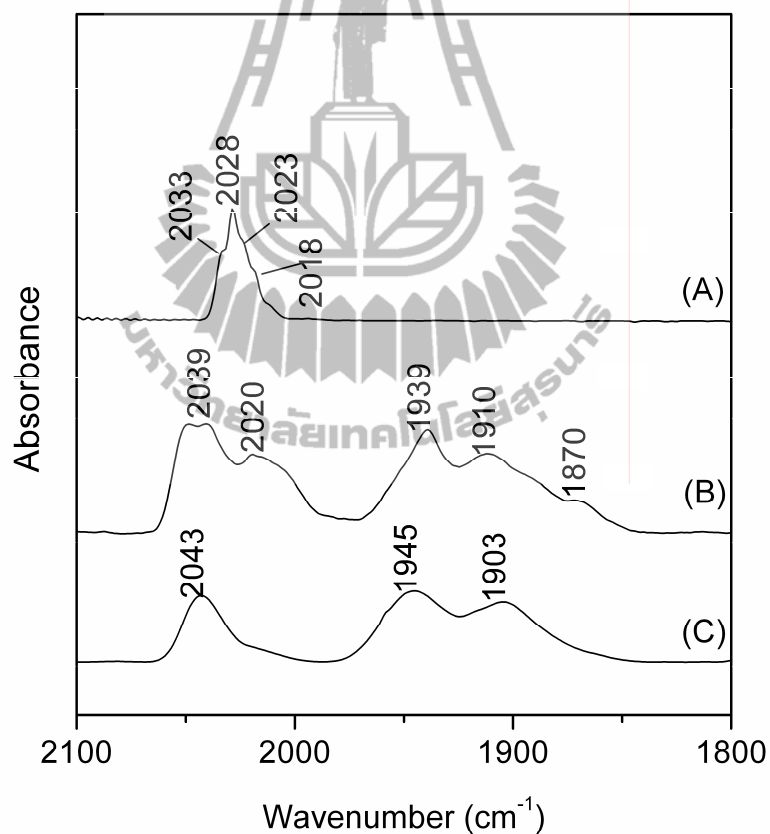


Figure 6.3 IR spectra in the ν_{CO} region characterizing $\text{Mn}(\text{CO})_5\text{H}$ in the gas phase (A); sample prepared by chemisorption of $\text{Mn}(\text{CO})_5\text{H}$ on MgO (B); and spectrum of sample represented by spectrum (B) after O_2 treatment at 25°C and $P_{\text{O}_2} = 0.1$ bar (C).

The literature provides a basis for assigning the ν_{CO} bands of the supported manganese carbonyl species. The bands characterizing the supported sample made from $\text{Mn}(\text{CO})_5\text{H}$ and MgO at 2039(m), 1939(s), and 1910(m) cm^{-1} are in the range of bands observed for the manganese tricarbonyls (a) *mer,trans*- $[\text{MnBr}(\text{CO})_3\{\text{P}(\text{C}_6\text{H}_4\text{Cl}_4)_3\}]_2$, observed at 2033(w), 1951(vs), and 1901 cm^{-1} , (Beckett et al., 2003) (b) *fac,cis*- $[\text{MnBr}(\text{CO})_3(\text{dppb})]$, at 2028(s), 1962(s), and 1910(s), (Beckett et al., 2003) and (c) *fac*- $\text{MnBr}(\text{CO})_3[\text{H}(\text{pzAn}^{\text{Me}})]$, at 2029, 1923, and 1902 cm^{-1} (Liddle et al., 2010).

The bands at 2020(m) and 1870(sh) cm^{-1} almost match the most intense band of $\text{Mn}(\text{CO})_5\text{H}$ in THF [(2118(vw), 2016(vs), and 2007(s) cm^{-1}] (Muetterties and Dekker, 1971) and $\text{Mn}(\text{CO})_5^-$ on MgO [1863, 1891 cm^{-1}] (which is inferred to interact weakly with the surface) (Keyes et al., 1989), respectively. Thus, it can be inferred that there were at least two manganese carbonyl species in this sample.

The IR spectrum of the sample prepared from $\text{Mn}(\text{CO})_5\text{CH}_3$ and MgO is characterized by ν_{CO} bands in positions different from those of $\text{Mn}(\text{CO})_5\text{CH}_3$ in CH_2Cl_2 solution (Figure 6.4, spectrum A) [$\nu_{\text{CO}} = 2012(\text{vs})$ and 1987(m) cm^{-1}], indicating that the $\text{Mn}(\text{CO})_5\text{CH}_3$ reacted with MgO and was converted to other manganese carbonyl species.

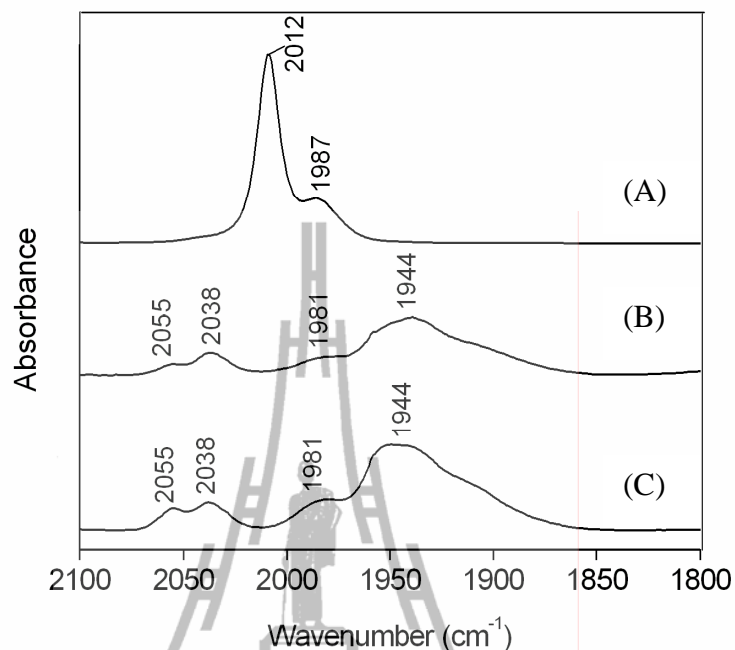


Figure 6.4 IR spectra of $\text{Mn}(\text{CO})_5\text{CH}_3$ in CH_2Cl_2 solution (A); of sample prepared by deposition of $\text{Mn}(\text{CO})_5\text{CH}_3$ on MgO (1.0 wt% Mn) (B); and of sample represented by spectrum B after O_2 treatment at 25°C and $P_{\text{O}_2} = 0.1$ bar (C).

The spectrum of the sample prepared from $\text{Mn}(\text{CO})_5\text{CH}_3$ and MgO (Figure 6.4, spectrum B) includes bands at 2055(w), 2038(w), 1981(w), and 1944(s) cm^{-1} , which are in the same range as the bands characterizing the following manganese tetracarbonyl complexes: (a) $[\text{Mn}(\text{CO})_4(\text{S}_2\text{PMe}_2)]$, at 2015(vs), 1978(s), and 1936(s) cm^{-1} (Almond et al., 1995); (b) $[\text{Mn}(\text{CO})_4\text{Br}]_2$, at 2056, 2023, 1982, and 1954 cm^{-1} (Abel and Butler, 1964); (c) $[\text{Mn}(\text{CO})_4\text{I}]_2$, at 2048, 2022, and 1983 cm^{-1} (Abel and Butler, 1964); and (d) $\text{Hg}[\text{Mn}(\text{CO})_4\text{P}(\text{OPh}_3)]_2$, at 2055.0, 2021.3, 1977.0, 1964.7, and 1954.2 cm^{-1} (Parker, 1969). Because the IR bands at 2948(w) and 2908(w) cm^{-1} (Mahmooda et al., 2006), corresponding to CH_3 group were not

observed in the spectrum of the supported sample, we infer that the CH_3 group was removed as a consequence of the adsorption.

6.3.2.2 XANES spectroscopy

Because the IR spectra show that the sample prepared from $\text{Mn}(\text{CO})_5\text{H}$ and MgO consisted of a mixture of supported manganese carbonyl species, this sample was not characterized by XANES spectroscopy (as the data quality would not allow a satisfactory resolution of the components of the mixture). However, the XANES spectrum characterizing the sample prepared from $\text{Mn}(\text{CO})_5\text{CH}_3$ and MgO shows the edge energy at 6549 eV which is 10 eV higher than that of manganese foil, indicating that the manganese in this supported sample was predominantly present as cationic species.

6.3.2.3 EPR spectroscopy

The EPR spectrum of the sample formed by adsorption of $\text{Mn}(\text{CO})_5\text{H}$ on MgO (Figure 6.5, spectrum B) indicates a signal of sextet hyperfine splitting with a coupling constant of 82.11G, indicative of Mn^{2+} (Mariscal et al., 1994). However, this signal is very weak, and we recognize that it might have resulted from impurities in the MgO rather than Mn^{2+} from the precursor. Thus, we also measured the EPR spectrum of the pretreated MgO, as shown in Figure 6.5, spectrum A. The spectrum includes a weak signal characterized by sextet hyperfine splitting which confirms that there was some Mn^{2+} impurity initially present in the MgO. Thus, we conclude that the oxidation state of essentially all of the manganese in the supported sample prepared from $\text{Mn}(\text{CO})_5\text{H}$ was not +2 and must have been either +1 (as in precursor the $\text{Mn}(\text{CO})_5\text{H}$) or greater than +1—as these species are EPR silent.

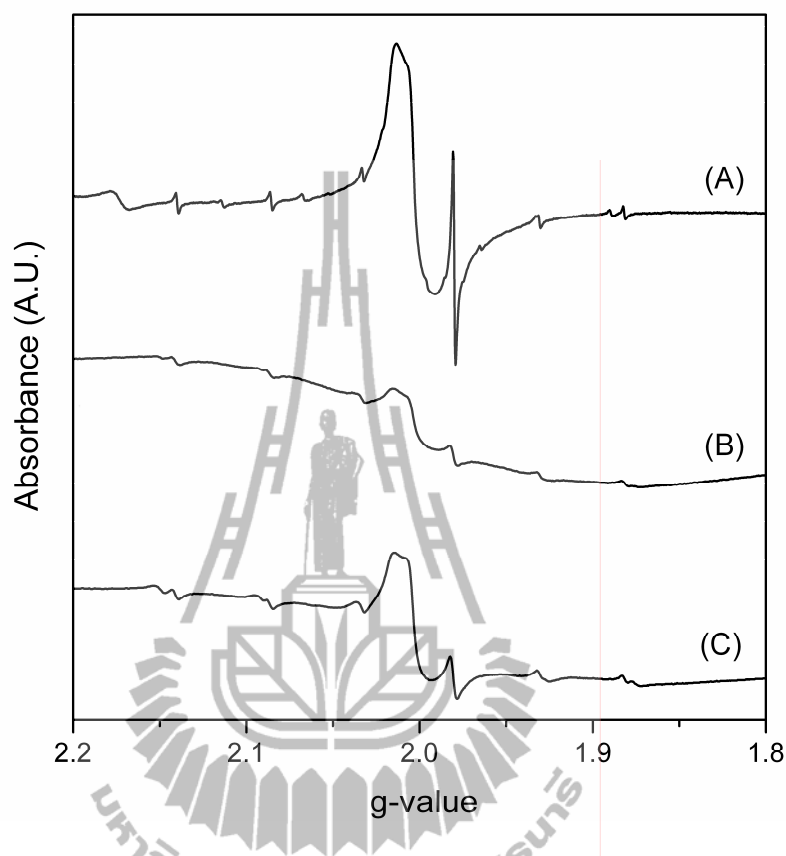


Figure 6.5 EPR spectra of pretreated MgO (A); sample prepared by chemisorption of $\text{Mn}(\text{CO})_5\text{H}$ on MgO (B), and sample prepared by chemisorption of $\text{Mn}(\text{CO})_5\text{H}$ on MgO after treatment in O_2 (C).

The EPR spectrum of the sample prepared from $\text{Mn}(\text{CO})_5\text{CH}_3$ and MgO includes a very weak signal characteristic of Mn^{2+} (spectrum not shown). The spectrum is again similar to that of MgO, showing that this sample contained a very small amount of Mn^{2+} , which again we identify as an impurity. Therefore, we conclude that the oxidation state of manganese in the supported species in this sample was not +2.

6.3.2.4 EXAFS spectroscopy

Because the IR results indicated that the supported species in sample prepared from $\text{Mn}(\text{CO})_5\text{CH}_3$ and MgO were nearly uniform, we used EXAFS spectroscopy to characterize it. The EXAFS parameters representing this sample (Table 6.1) include Mn–C and Mn–O* contributions (O* is oxygen of carbonyl groups), each with a coordination number of approximately 4, showing that there were four carbonyl ligands per Mn atom, on average.

The EXAFS data also indicate another Mn–O_s contribution (O_s refers to an oxygen atom of MgO) and a Mn–Mg contribution, with coordination numbers of approximately 2 and 1, respectively. The presence of these two contributions indicates that the manganese carbonyl precursor reacted with the MgO support. Consistent with this inference, the Mn–O_s distance of 2.12 Å is characteristic of bonding between manganese cations and oxygen in ligands. For example, the distance between Mn²⁺ and O²⁻ in Mn/Co/TiO₂ system characterized by EXAFS spectroscopy was reported to be 2.223 Å (Morales et al., 2006) which matches the Mn–O distance of MnO determined crystallographically (Kim and Park, 2003). The Mn–O_s coordination number indicates that the MgO support was a bidentate ligand, as in presumably analogous samples such as that prepared from Ir₄(CO)₁₂ supported on MgO after decarbonylation in He followed by H₂ at 300°C (Kawi et al., 1994) or MgO-supported gold complex synthesized by reaction of Au(CH₃)₂(acac) with highly dehydroxylated MgO (Uzun et al., 2009). The Mn–Mg contribution shows that the manganese complexes were bonded to the MgO surface near Mg cations, and the lack of Mn–Mn contributions confirms that the surface species remained mononuclear.

Table 6.1 The EXAFS parameters characterizing sample prepared from $\text{Mn}(\text{CO})_5\text{CH}_3$ on MgO^a .

Absorber–backscatterer pair	N	$\Delta\sigma^2$ (\AA^{-2})	R (\AA)	E_0 (eV)
Mn–C	3.7	0.01031	1.87	1.82
Mn–O*	3.8	0.00710	2.96	1.82
Mn–O _s	2.2	0.00937	2.12	8.34
Mn–Mg	1.2	0.00205	3.48	9.71

^aNotation: N , coordination number; R , distance between absorber and backscatterer atoms; $\Delta\sigma^2$, sigma-squared value (disorder term); ΔE_0 , inner potential correction; O*, oxygen of carbonyl group; O_s, oxygen atom of MgO. In the fitting, the ΔE_0 values for Mn–C and Mn–O contributions were constrained to be equal because the multiple scattering identified C and O atoms as present in linear Mn–C–O combinations (terminal manganese carbonyls). Typical errors: N , $\pm 20\%$; R , ± 0.04 \AA ; $\Delta\sigma^2$, $\pm 20\%$; ΔE_0 , $\pm 20\%$.

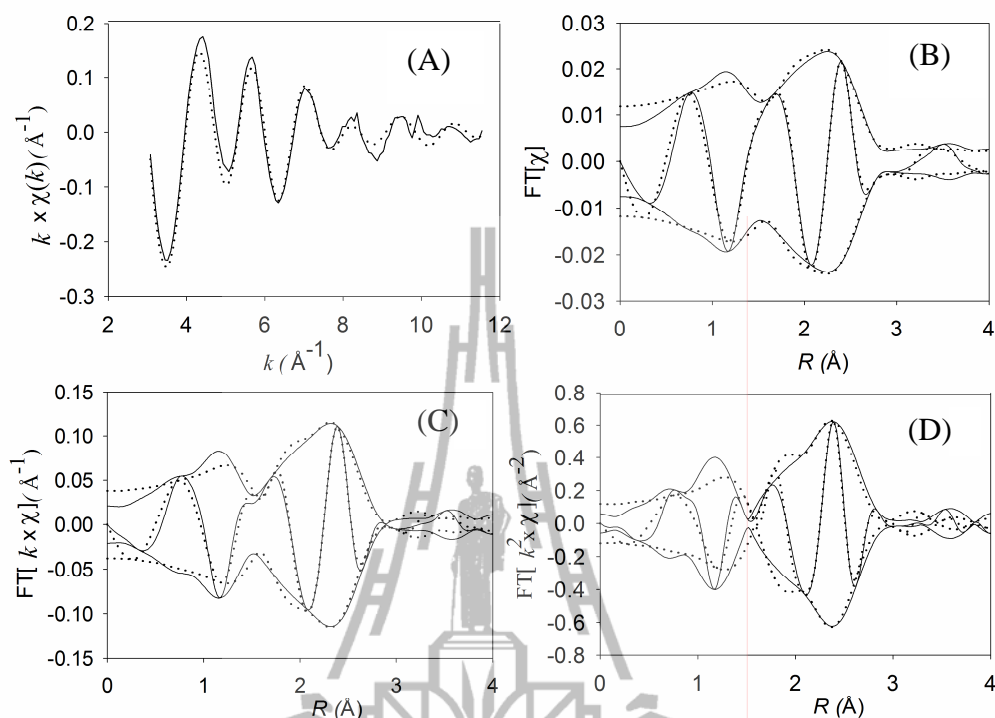


Figure 6.6 EXAFS data characterizing sample prepared from $\text{Mn}(\text{CO})_5\text{CH}_3$ on MgO (1.0 wt% Mn) after O_2 treatment (— ; data, ; best-fit): k -weighted EXAFS function in k -space (A); imaginary part and magnitude of EXAFS function in R -space with FT k^0 -weighting (B), FT k^1 -weighting (C), and FT k^2 - weighting (D). ($\Delta k = 3.08$ - 11.54\AA^{-1}).

6.3.3 Characterization of samples after O_2 treatment

6.3.3.1 IR spectroscopy

The IR spectra in the OH region of the samples prepared from $\text{Mn}(\text{CO})_5\text{H}$ and from $\text{Mn}(\text{CO})_5\text{CH}_3$ on MgO remained essentially unchanged after the samples were treated in O_2 at room temperature. These results show that there was no change in the OH group on MgO as a result of the exposure to O_2 .

The ν_{CO} IR spectra of the sample prepared from $\text{Mn}(\text{CO})_5\text{H}$ on MgO after treatment in O_2 (Figure 6.3, spectrum C) includes three bands, at 2043(s), 1945(s), and 1903(s) cm^{-1} , essentially matching those of the supported manganese tricarbonyl, as assigned for the sample prepared from $\text{Mn}(\text{CO})_5\text{H}$ and MgO . However, the band at 2020(w) and a shoulder at 1870 cm^{-1} that were evident in the spectrum of the untreated sample and assigned to manganese pentacarbonyls were no longer observed.

In contrast, the IR spectrum of sample prepared from $\text{Mn}(\text{CO})_5\text{CH}_3$ and MgO did not show an significant change resulting from the O_2 treatment.

6.3.3.2 Mass spectra of effluent gas

The mass spectrum characterizing the effluent gases during the O_2 treatment of the sample prepared from $\text{Mn}(\text{CO})_5\text{H}$ and MgO (Figure 6.7) indicates the presence of CO signal, suggesting that carbonyl ligands were removed from the sample. The CO ligands that were removed during the O_2 treatment were most likely the ligand from manganese pentacarbonyl species, as demonstrating by the absence of these species in the IR spectrum of the O_2 treated sample (Figure 6.3, spectrum C).

The mass spectrum characterizing the effluent gases formed during the O_2 treatment of the sample prepared from $\text{Mn}(\text{CO})_5\text{CH}_3$ and MgO does not show any evidence of CO removal, indicating that the CO ligands were not removed during the treatment.

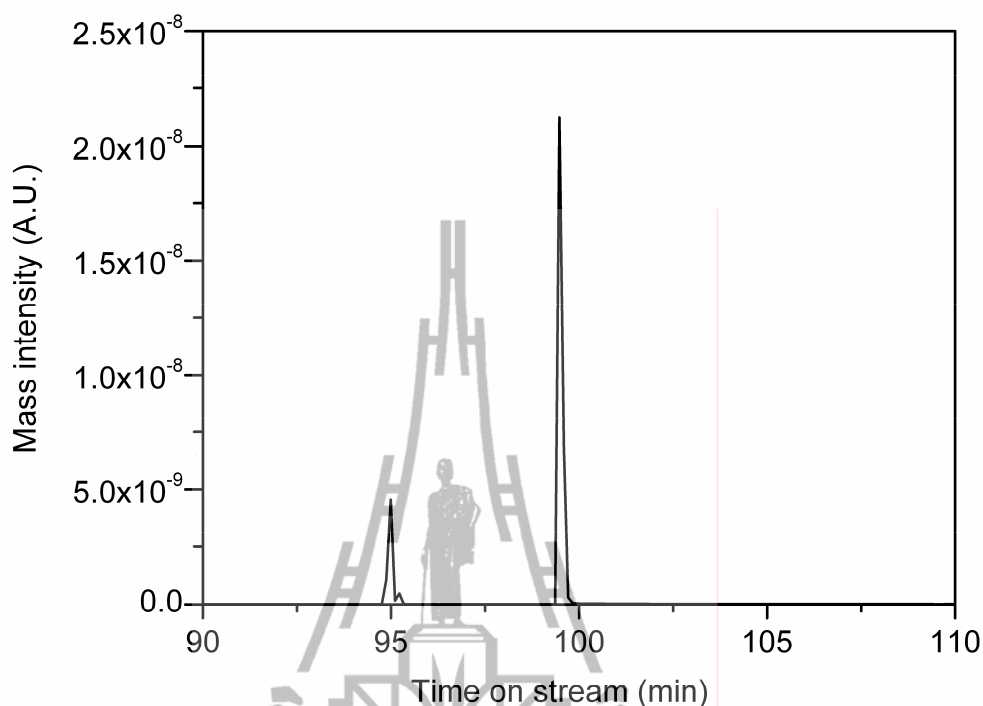


Figure 6.7 Mass spectrometry data: the CO^+ signal characterizing the effluent gas formed by treatment of the sample prepared from $\text{Mn}(\text{CO})_5\text{H}$ on MgO in flowing O_2 ($P_{\text{O}_2} = 0.1$ bar) at room temperature.

6.3.3.3 XANES spectroscopy

The edge energy of the sample prepared from $\text{Mn}(\text{CO})_5\text{H}$ and MgO shifted as a result of the O_2 treatment from a value of 6539 eV to to a value of 6549 eV, which is 10 eV higher than that of manganese foil. This energy is sufficiently greater than the edge energy of manganese foil, to clearly show that manganese was cationic.

The lack of any change in the edge energy of sample prepared from $\text{Mn}(\text{CO})_5\text{CH}_3$ and MgO after O_2 treatment indicates the lack of change in electronic properties of the manganese in this sample during the O_2 treatment.

6.3.3.4 EPR spectroscopy

The EPR spectra of the samples prepared from $\text{Mn}(\text{CO})_5\text{H}$ and from $\text{Mn}(\text{CO})_5\text{CH}_3$ on MgO also remained essentially unchanged after the O_2 treatment. These results are consistent with the XANES result indicating essentially no changes in the electronic properties of the manganese as a result of exposure to O_2 ; thus, it can be inferred that there were negligible changes in the oxidation states of manganese.

6.3.3.5 EXAFS spectroscopy

The IR spectra show that the sample prepared from $\text{Mn}(\text{CO})_5\text{H}$ on MgO consisted of the mixture of manganese tricarbonyl and manganese pentacarbonyl. This sample was not characterized by EXAFS spectroscopy because of its complexity. However, treatment of this sample in O_2 led to a more uniform structure that was characterized by EXAFS spectroscopy. The EXAFS parameters characterizing this sample after the O_2 treatment include Mn–C, Mn–O*, Mn–O_s, and Mn–Mg contributions (Table 6.2). The absence of Mn–Mn contributions confirms that the surface species remained mononuclear. The Mn–C and Mn–O* contributions with coordination numbers of approximately 3 point to manganese tricarbonyls, in agreement with the IR spectra. The Mn–O_s contribution demonstrates that the manganese was bonded to the MgO support. The Mn–O_s coordination number of 1, within error, indicates that each Mn atom was bonded to only one O atom of MgO . Because the Mn–O_s interaction in sample prepared from $\text{Mn}(\text{CO})_5\text{H}$ and MgO was not characterized by IR spectroscopy, the metal–support interactions in the as-

prepared and O₂-treated samples cannot be compared. However, the IR and EXAFS results characterizing the carbonyl ligands in the two samples suggest that the manganese pentacarbonyl species was either removed or converted during the O₂ treatment.

Table 6.2 The EXAFS parameters characterizing sample prepared from Mn(CO)₅H on MgO after O₂ treatment ^a.

Model No.	Absorber–backscatterer pair		N	$\Delta\sigma^2(\text{Å}^{-2})$	$R(\text{Å})$	$E_0(\text{eV})$
1	Mn–C		2.81	0.01132	1.98	7.02
	Mn–O*		2.72	0.01464	3.30	7.02
	Mn–O _s		0.73	0.01207	2.23	-9.69
	Mn–Mg		0.36	0.00012	3.60	-9.97
2	Mn–C		2.90	0.01107	1.98	6.92
	Mn–O*		2.84	0.01450	3.30	6.92
	Mn–O _s		0.62	0.00767	2.24	-10.42
	Mn–Mg		0.36	0.00025	3.59	-8.88
3	Mn–C		2.41	0.01211	1.981	7.05
	Mn–O*		2.30	0.01472	3.294	7.05
	Mn–O _s		0.75	0.01401	2.216	-9.54

^aNotation: N , coordination number; R , distance between absorber and backscatterer atoms; $\Delta\sigma^2$, sigma-squared value (disorder term); ΔE_0 , inner potential correction; O*,

oxygen of carbonyl group; O_s, oxygen atom of MgO. In the fitting, the ΔE_0 values for Mn–C and Mn–O* were constrained to be equal (see Table 6.2). Typical errors: N , $\pm 20\%$; R , ± 0.04 Å; $\Delta\sigma^2$, $\pm 20\%$; ΔE_0 , $\pm 20\%$.

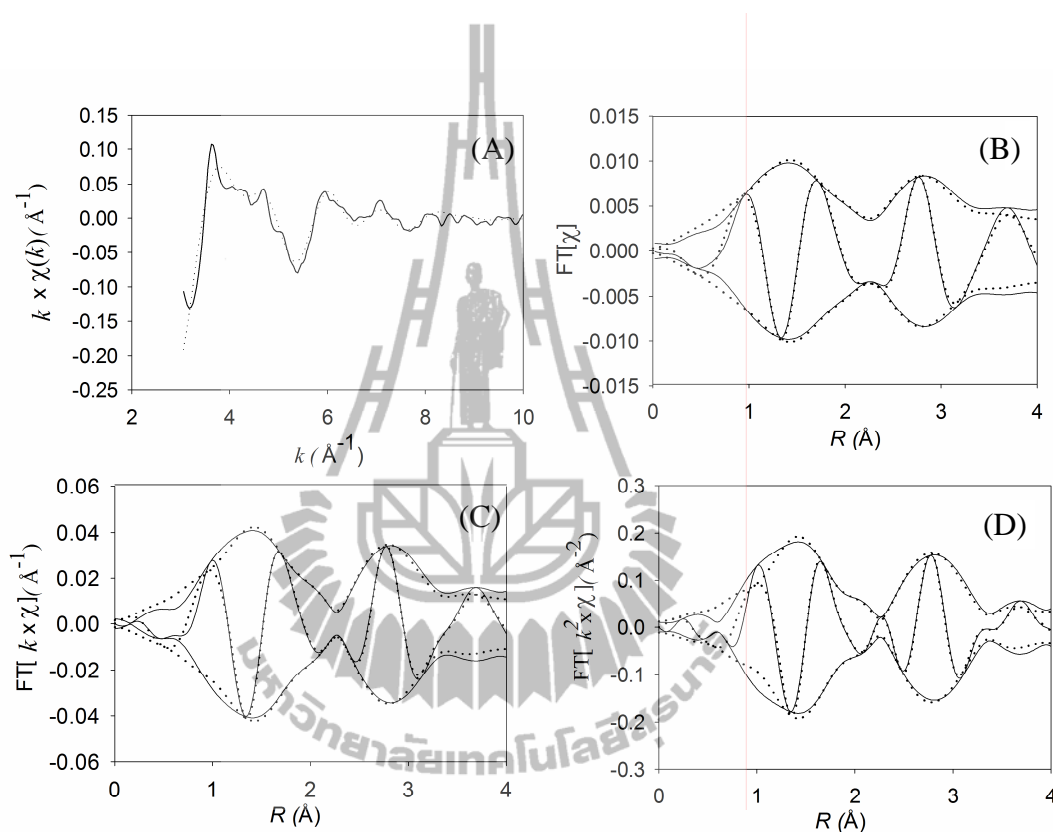


Figure 6.8 EXAFS data characterizing sample prepared from $\text{Mn}(\text{CO})_5\text{H}$ on MgO (1.0 wt% Mn) after O_2 treatment (— ; data,; best-fit): k -weighted EXAFS function in k -space (A); imaginary part and magnitude of EXAFS function in R -space with $FT k^0$ -weighting (B), $FT k^1$ -weighting (C), and $FT k^2$ -weighting (D) ($\Delta k = 3.06$ – 10.30 \AA^{-1}).

6.4 Discussion

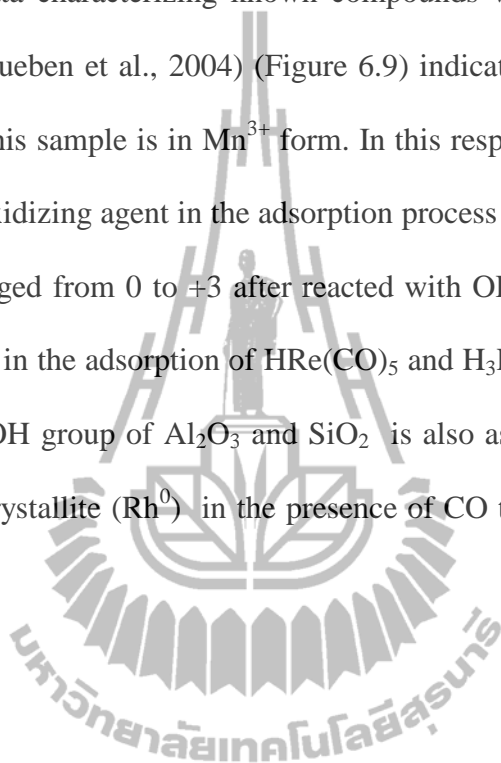
6.4.1 Adsorption of $\text{Mn}(\text{CO})_5\text{H}$ on MgO

The complementary spectroscopic techniques clearly demonstrate that each of the two precursors reacted with the OH groups on the surface of MgO , leading to chemisorption of the manganese carbonyls. The IR spectra characterizing the sample prepared from $\text{Mn}(\text{CO})_5\text{H}$ and MgO show the non-uniformity of the surface species—more than one supported manganese carbonyl formed. The deprotonation was observed in the adsorption of $\text{Mn}(\text{CO})_5\text{H}$ on MgO and this reaction was also observed in the reaction of $\text{Re}(\text{CO})_5\text{H}$ and MgO as reported by Kirilin et al. (1990). The supported samples prepared from $\text{Re}(\text{CO})_5\text{H}$ were synthesized in the presence of hexane solvent; the IR spectrum characterizing the supported rhenium complex demonstrated the partial deprotonation of $\text{Re}(\text{CO})_5\text{H}$ upon adsorption, resulting in only one surface species postulated to be $\text{MgOH}^+\cdots[\text{Re}(\text{CO})_5]^-$. In contrast to the supported rhenium complex, the supported species formed from $\text{Mn}(\text{CO})_5\text{H}$ in this work consisted of a mixture of supported manganese carbonyls (manganese tricarbonyl and manganese pentacarbonyl). Some of the differences between Kirilin's rhenium chemistry and manganese chemistry in this work may have to do with different coverages of the MgO surfaces—neither Kirilin nor we could determine the exact surface coverage.

O_2 -treatment of the mixture of manganese carbonyls on MgO led to the removal of manganese pentacarbonyl species from MgO surface and resulted in more uniform surface species, inferred to be essentially manganese tricarbonyl.

To further elucidate the chemistry of the decarbonylation of the manganese pentacarbonyl on MgO , we turned to EPR and XANES experiments; the EPR data

demonstrate that the oxidation state of manganese in this sample was not +2, but they do not rule out manganese in the other oxidation states. The XANES spectra offer the prospect of providing insight into the manganese oxidation states in the samples; a plot of XANES data characterizing known compounds with manganese in various oxidation states (Stueben et al., 2004) (Figure 6.9) indicates—by interpolation—that the manganese in this sample is in Mn^{3+} form. In this respect, the OH group of MgO is found to be an oxidizing agent in the adsorption process because the oxidation state of manganese changed from 0 to +3 after reacted with OH group. Such role of OH group was reported in the adsorption of $\text{HRe}(\text{CO})_5$ and $\text{H}_3\text{Re}_3(\text{CO})_{12}$ on MgO, (Kirlin et al., 1990). The OH group of Al_2O_3 and SiO_2 is also as an oxidizing agent in the adsorption of Rh crystallite (Rh^0) in the presence of CO to produce $\text{Rh}^{\text{I}}(\text{CO})_2$ (Basu et al., 1987).



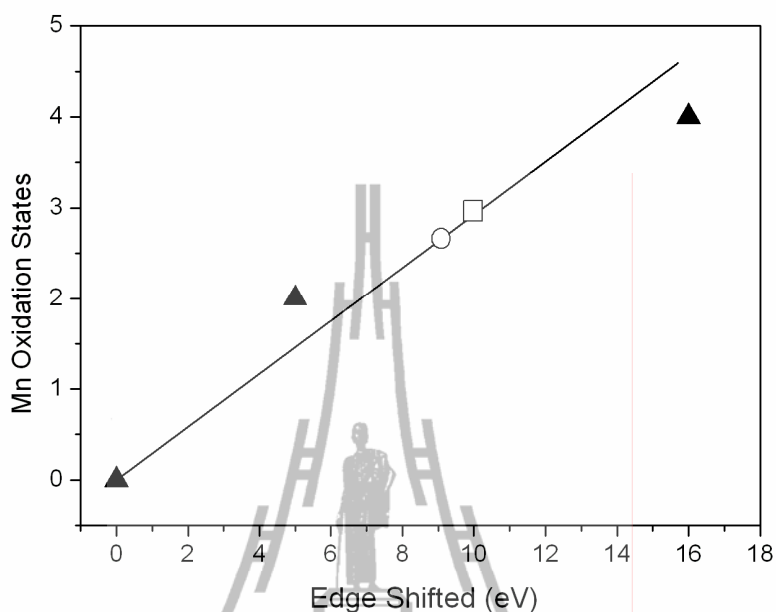


Figure 6.9 XANES calibration data and comparison with edge shift of sample prepared from $\text{Mn}(\text{CO})_5\text{H}$ and MgO after O_2 treatment; ○; and sample prepared from $\text{Mn}(\text{CO})_5\text{CH}_3$ and MgO , □; Literature data characterizing standard samples including manganese foil and manganese oxides, ▲ (Stueben et al., 2004).

The EXAFS fitting that were found to be most appropriate included Mn-C, Mn-O*, and Mn-O_s contributions (Table 6.2). For model No. 1 and No.2, the results indicate Mn-C and Mn-O* contributions with coordination numbers of approximately 3, indicating manganese tricarbonyls, consistent with the IR spectra. Whereas model No 3 shows the coordination number of Mn-C and Mn-O* which are not close to three and thus contrast to the IR results. Consequently, this model was neglected.

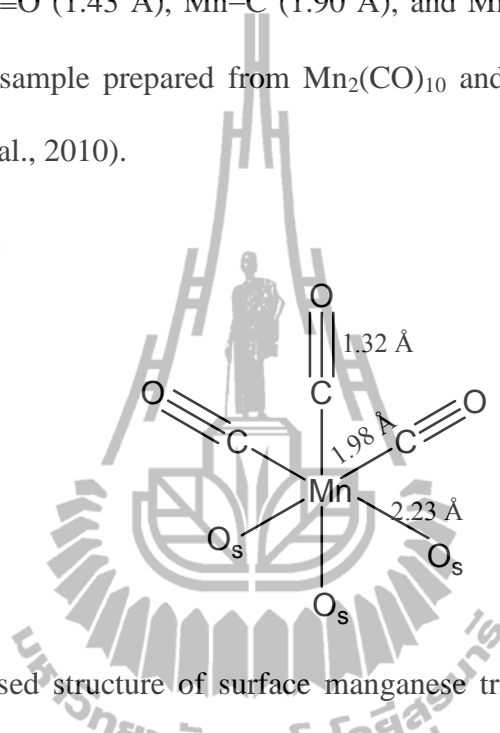
A Mn-O_s contribution was observed for all models with coordination number about 1. However, Model No.2 was also neglected because the E_0 of Mn-O_s contribution is exceed the limit (10 to -10 eV). Thus the fitting result from model

No. 1 was chosen to represent surface species of this sample. If each carbonyl and surface oxygen ligand is a 2-electron donor, the Mn(III) tricarbonyl complex would be a 12-electron complex, which is highly unlikely because the most common (stable) complexes of manganese are 18-electron and 16-electron complexes (Shriver et al., 1990).

Because, the only experimental information about Mn-O_s coordination is the EXAFS data and the quality of several scans is not sufficient to determine it accurately, the number of Mn-O_s contribution could alternatively be estimated by performing electron counting for the Mn(III) tricarbonyl complex. If the Mn³⁺ were five-coordinated with two Mn-O_s contributions, it would be a 14-electron complex, which is uncommon. On the other hand, if Mn³⁺ were six-coordinated, three Mn-O_s contribution, it would be a 16-electron complex, which is the most common complex of manganese. Other common manganese complexes are 18-electron complexes. However, the 18-electron complex of Mn³⁺ would be 7-coordinated, which is uncommon. Thus it can be inferred that the supported manganese complex after treatment in O₂ stream is most likely Mn³⁺ bonded to 3 carbonyl ligands and 3 oxygen atoms of the MgO. This model representing the surface species of the sample prepared from Mn(CO)₅H and MgO after O₂ treatment is illustrated in Scheme 6.1.

The model of surface species of the sample prepared from Mn(CO)₅H and MgO in O₂ stream is consistent with the surface species formed in the sample prepared from Mn₂(CO)₁₀ on MgO in O₂ as described in Chapter V. The Mn₂(CO)₁₀ was deposited onto MgO by CVD and treated in O₂. The IR, EPR, and XANES results characterizing this sample demonstrate that the Mn–Mn bond in Mn₂(CO)₁₀ was cleaved during the oxidative adsorption on MgO surface, resulting in the

mononuclear manganese species. In the present work, the surface species remained mononuclear as in the precursor, which is $\text{Mn}(\text{CO})_5\text{H}$. Proposed surface species is shown in scheme 6.1. Bond distance of $\text{C}\equiv\text{O}$, $\text{Mn}-\text{C}$, and $\text{Mn}-\text{O}_s$ are close to the bond distance of $\text{C}\equiv\text{O}$ (1.43 Å), $\text{Mn}-\text{C}$ (1.90 Å), and $\text{Mn}-\text{O}_s$ (1.98 Å) reported for surface species of sample prepared from $\text{Mn}_2(\text{CO})_{10}$ and MgO after O_2 treatment (Khabuanchalad et al., 2010).



Scheme 6.1 Proposed structure of surface manganese tricarbonyl species prepared from $\text{Mn}(\text{CO})_5\text{H}$ on MgO after O_2 treatment.

6.4.2 Adsorption of $\text{Mn}(\text{CO})_5\text{CH}_3$ on MgO

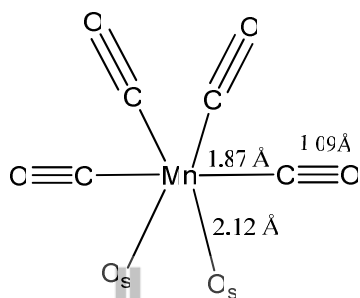
The spectra characterizing the samples prepared from $\text{Mn}(\text{CO})_5\text{CH}_3$ and partially dehydroxylated MgO show that the chemisorption involved the reaction of the precursor with surface OH groups and the removal of CO and CH_3 ligands from precursor. In the adsorption of $\text{Mn}(\text{CO})_5\text{CH}_3$ on MgO , the reaction might be expected to form CH_4 , as suggested by the work of Becker et al., 1980. They investigated the amounts of gases liberated as helium flowed through samples made from $\text{Mn}(\text{CO})_5\text{CH}_3$ and dehydroxylated alumina (DA) and partially dehydroxylated alumina (PDA). Their results suggested that the CO removal from the sample

prepared with PDA was significantly faster than when the support was DA. Moreover, the liberation of CH_4 was observed in the sample made with PDA but not in the sample made with DA. This result is attributed to the low OH content in DA sample. The effect of OH group mentioned above illustrates that the protonolysis of the CH_3 ligand occurred during the adsorption of the precursor, subsequently resulting in CH_4 removal.

In this work, $\text{Mn}(\text{CO})_5\text{CH}_3$ was chosen as a precursor because of the expectation that it might provide evidence of the reaction involving CH_3 groups and support OH groups. Indeed, in adsorption of this precursor, the removal of OH group from MgO and CH_3 groups from the precursor were both observed. The CH_3 group might have reacted with OH group to form CH_4 as in Becker's work. However, it was not determined whether CH_4 was formed.

To determine the oxidation state of manganese in the sample prepared from $\text{Mn}(\text{CO})_5\text{CH}_3$ and MgO, XANES data were compared with those characterizing known compounds with manganese in various oxidation states (Figure 6.9). Similar to the characterization of sample prepared from $\text{Mn}(\text{CO})_5\text{H}$ and MgO after O_2 treatment, the plot indicates that manganese in this sample is in +3 oxidation state. The electron counting, considering carbonyl and surface oxygen to be two-electron donor ligands, demonstrates that the surface species were 16-electron complexes.

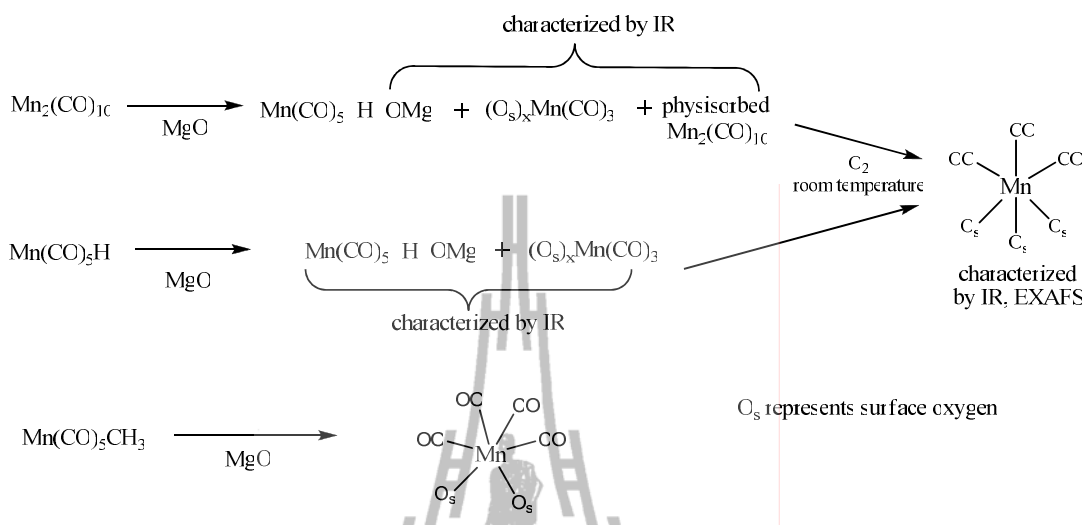
A model representing the surface species of this sample is presented in Scheme 6.2. The Mn–C and C–O* bond distances in this model are in agreement with the crystallographic data characterizing $[\text{Mn}(\text{CO})_4(\text{S}_2\text{PMe}_2)]$ (Almond et al., 1995), which show Mn–C and Mn–O* at 1.81 and 1.14 Å, respectively.



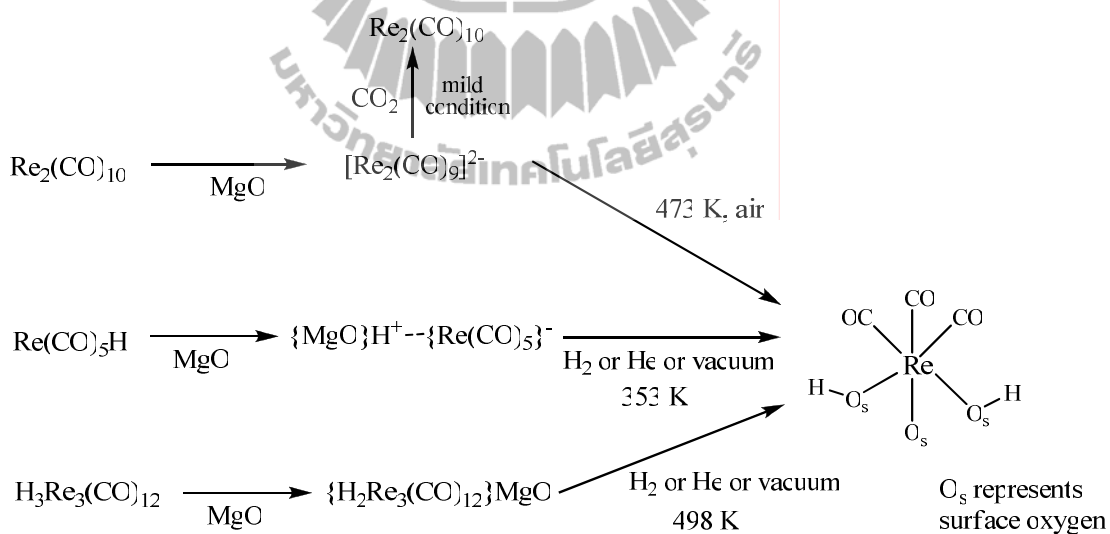
Scheme 6.2 Proposed structure of surface manganese tetracarbonyl species prepared from $\text{Mn}(\text{CO})_5\text{CH}_3$ and MgO (1.0 wt% Mn).

6.4.3 Comparison of the chemistry of manganese carbonyls and rhenium carbonyls on the surface of MgO

The interaction of $\text{Mn}(\text{CO})_5\text{H}$ and $\text{Mn}_2(\text{CO})_{10}$ with the surface of partially dehydroxylated MgO produced more surface species than that of rhenium carbonyls [$\text{Re}_2(\text{CO})_{10}$, $\text{H}_3\text{Re}(\text{CO})_{12}$ and $\text{HRe}(\text{CO})_5$]. This effect suggested that manganese complexes are more reactive than rhenium complexes. In contrast to $\text{Mn}_2(\text{CO})_{10}$ and $\text{Mn}(\text{CO})_5\text{H}$, the reaction of $\text{Mn}(\text{CO})_5\text{CH}_3$ and MgO produced only one surface species. In both rhenium and manganese carbonyl complexes, oxidative fragmentation of dinuclear to produce mononuclear tricarbonyl surface species was observed, but the reaction of manganese complexes (in O_2 at room temperature) happened at lower temperature than the reaction of rhenium complexes (in air at 200°C). The proposed surface chemistry of manganese carbonyl and rhenium carbonyl with MgO were shown in scheme 6.3 and 6.4, respectively.



Scheme 6.3 Proposed chemistry of manganese carbonyls on the surface of MgO.



Scheme 6.4 Proposed chemistry of rhenium carbonyls on the surface of MgO derived from Kirilin et al., 1990; Papile and Gates, 1992; Kirilin et al., 1990.

6.5 Conclusions

The adsorption of $\text{Mn}(\text{CO})_5\text{H}$ on partially dehydroxylated MgO produced a surface species inferred to be a mixture of manganese pentacarbonyls and manganese tricarbonyls, as shown by IR spectroscopy. After treatment of this sample in flowing O_2 at 298K, the only manganese species on the support was manganese tricarbonyl. XANES and EPR data show that the manganese in the originally prepared sample was cationic and that the manganese oxidation state did not change as a result of the O_2 treatment. In contrast, the reaction between $\text{Mn}(\text{CO})_5\text{CH}_3$ and MgO led to the formation of supported manganese tetracarbonyl, and again the manganese was cationic. O_2 treatment of the sample prepared from $\text{Mn}(\text{CO})_5\text{CH}_3$ on MgO did not change either the manganese oxidation state or the number of carbonyl ligand on the manganese in this sample.

6.6 References

- Abel, E. W. and Butler, I. S. (1964). Halogenocarbonylmanganese anions. **J. Chem. Soc.** 434-437.
- Almond, M. J., Drew, M. G. B., Sarikahya, F., and Senturk, O. S. (1995). Photochemical synthesis and crystal structure of dimethylphosphino dithiatomanganese(I) tetracarbonyl, $[\text{Mn}(\text{CO})_4(\text{S}_2\text{PMe}_2)]$. **Polyhedron**. 14 (11): 1433-1437.
- Basu, P., Panayotov, D., and Yates, T. J. (1987) Spectroscopic evidence for the involvement of OH groups in the formation of $\text{Rh}^{\text{I}}(\text{CO})_2$ on metal oxide supports. **J. Phys. Chem.** 91: 3133-3136.

- Becker, J., Wentrup, C., Katz, E., and Zeller, K. P. (1980). Surface-induced alkyl migration reactions in metal carbonyls. **J. Am. Chem. Soc.** 102: 5112-5114.
- Beckett, M. A., Brassington, D. S., Coles, S. J., Gelbrich, T., Light, M. E., and Hursthouse, M. B. (2003). A crystallographic and spectroscopic investigation of the stereochemistry of $[\text{MBr}(\text{CO})_3\text{L}_2]$ ($\text{M}=\text{Mn}, \text{Re}$) complexes: crystal and molecular structures of $[\text{MBr}(\text{CO})_3\text{L}_2]$ $\{\text{M}=\text{Mn}, \text{L}=\text{P}(\text{C}_6\text{H}_4\text{Cl}-4)_3, 1/2\text{dppe}, 1/2\text{dppf}; \text{M}=\text{Re}, \text{L}=\text{P}(\text{C}_6\text{H}_4\text{OMe}-4)_3, 1/2\text{dppf}\}$. **J. Organomet. Chem.** 688: 174-180.
- Bhirud, V. A., Iddir, H., Browning, N. D., and Gates, B. C. (2005). Intact and fragmented triosmium clusters on MgO: characterization by X-ray absorption spectroscopy and high-resolution transmission electron microscopy. **J. Phys. Chem. B** 109: 12738-12741.
- Chotisuwan, S., Wittayakun, J., and Gates, B. C. (2006). Pt_3Ru_6 clusters supported on $\gamma\text{-Al}_2\text{O}_3$: Synthesis from $\text{Pt}_3\text{Ru}_6(\text{CO})_{21}(\mu_3\text{-H})(\mu_3\text{-H})_3$, structural characterization, and catalysis of ethylene hydrogenation and *n*-butane hydrogenolysis. **J. Phys. Chem. B** 110: 12459-12469.
- Dahl, L. F. and Rundle, R. E. (1963). The crystal structure of dimanganese decacarbonyl $\text{Mn}_2(\text{CO})_{10}$. **Acta Crystallographica.** 16: 419-426.
- Datka, J., Gil, B., and Baran P. (2003). IR study of heterogeneity of OH groups in zeolite HY-splitting of OH and OD bands. **J. Mol. Struct.** 645: 45-49.
- Diwald, O., Sterrer, M., and Knözinger, E. (2002). Site selective hydroxylation of the MgO surface. **Phys. Chem. Chem. Phys.** 4: 2811-2817.

- Edgell, W. F., Fisher, J. W., Asato, G., and Risek, W. M. (1969). The infrared spectrum and vibrational assignments for pentacarbonylmanganese hydride. **Inorg. Chem.** 8: 1103-1108.
- Fierro-Gonzalez, J. C., Kuba, S., Hao, Y., and Gates, B. C. (2006). Oxide- and zeolite-supported molecular metal complexes and clusters: physical characterization and determination of structure, bonding, and metal oxidation state. **J. Phys. Chem. B.** 110: 13326-13351.
- Guglielminotti, E. and Zecchina A. (1984). Spectroscopic study of the adsorption and vacuum decarbonylation of $\text{Fe}(\text{CO})_5$ on MgO. **J. Mol. Catal.** 24: 331-344.
- Hlatky, G. G. (2000). Heterogeneous single-site catalysts for olefin polymerization. **Chem. Rev.** 100: 1347-1376.
- Huang, Y., Poissant, R. R., and Qiu, P. (2000). Study of the reactivity of $\text{Mn}(\text{CO})_5\text{Br}$ on the surface of zeolites by fourier transform raman and infrared spectroscopy. **Langmuir.** 16: 889-893.
- Hugues, F., Basset, J. M., Ben Taarit, Y., Choplin, A., Primet, M., Rojas, D., and Smith, A. K. (1982). Surface organometallic chemistry: formation of $\text{HFe}_3(\text{CO})_{11}^-$ from $\text{Fe}_3(\text{CO})_{12}$ and $\text{Fe}(\text{CO})_5$ on silica, alumina, magnesia, and zinc oxide. **J. Am. Chem. Soc.** 104: 7020-7024.
- International XAFS Society. (2010). **Error Reporting Recommendations: A Report of the Standard and Criteria Committee** [on-line]. Available: http://ixs.iit.edu/subcommittee_reports/sc/err-rep.pdf.

- Ishii, H., Ueda, M., Takeuchi, K., and Asai, M. (1999). Oxidative carbonylation of phenol to diphenyl carbonate catalyzed by Pd₂-Sn heterotrinnuclear complex along with Mn redox catalyst without any addition of ammonium halide. **J. Mol. Catal. A-Chem.** 144: 369-372.
- Jentoft, R. E., Deutsch, S. E., and Gates, B. C. (1996). Low-cost, heated, and/or cooled flow-through cell for transmission x-ray absorption spectroscopy. **Rev. Sci. Instrum.** 67: 2111-2112.
- Kawi, S., Chang, J. R., and Gates, B. C. (1994). Cluster catalysis: propane hydrogenolysis catalyzed by MgO-supported tetrairidium. **J. Phys. Chem.** 98: 12978-12988.
- Keyes, M. P., Gron, L. U., and Watters, K. L. (1989). Interactions of nickel and manganese carbonyls with oxide surfaces: formation of reduced, oxidized, and zerovalent metal species. **Inorg. Chem.** 28: 1236-1242.
- Khabuanchalad, S., Wittayakun, J., Lobo-Lapidus, R. J., Stoll, S., Britt, R. D., and Gates, B. C. (2010). Formation of a manganese tricarbonyl on the MgO surface from Mn₂(CO)₁₀: characterization by infrared, electron paramagnetic resonance, and X-ray absorption spectroscopies. **J. Phys. Chem. C** 114: 17212-17221.
- Kim, K. J. and Park, Y. R. (2003). Optical investigation of charge-transfer transitions in spinel Co₃O₄. **Solid. State. Commun.** 127: 25-28.
- Kirlin, P. S., DeThomas, F. A., Bailey, J. W., Gold, H. S., Dybowski C., and Gates, B. C. (1986). Molecular oxide-supported rhenium carbonyl complexes: synthesis and characterization by vibrational spectroscopy. **J. Phys. Chem.** 90: 4882-4887.

- Kirlin, P. S., DeThomas, F. A., Bailey, J. W., Moller, K., Gold, H. S., Dybowski, C., and Gates, B. C. (1986). Oxide-supported metals with molecular structures: Evidence of the metal-oxygen bond from Raman and inelastic electron tunneling spectra of $[\text{Re}(\text{CO})_3\{\text{O-Mg}\}\{\text{HO-Mg}\}_2]$ and $[\text{Re}(\text{CO})_3\{\text{O-Al}\}\{\text{HO-Al}\}_2]$. **Surf. Sci.** 175: L707-L713.
- Kirlin, P. S., Knözinger, H., and Gates, B. C. (1990). Mononuclear, trinuclear, and metallic rhenium catalysts supported on magnesia: effects of structure on catalyst performance. **J. Phys. Chem.** 94: 8451-8456.
- Kirlin, P. S., van Zon, F. M. B., Koningsberger, D. C., and Gates, B. C. (1990). Surface catalytic sites prepared from $[\text{HRe}(\text{CO})_5]$ and $[\text{H}_3\text{Re}_3(\text{CO})_{12}]$: Mononuclear, trinuclear, and metallic rhenium catalysts supported on MgO. **J. Phys. Chem.** 94: 8439-8450.
- Koningsberger, D. C., Mojet, B. L., van Dorssen, G. E., and Ramaker, D. E. (2000). XAFS spectroscopy; fundamental principles and data analysis. **Top. Catal.** 10: 143-155.
- Kulkarni, A., Mehraeen, S., Reed, B. W., Okamoto, N. L., Browning, N. D., and Gates, B. C. (2009). Nearly uniform decaosmium clusters supported on MgO: characterization by X-ray absorption spectroscopy and scanning transmission electron microscopy. **J. Phys. Chem. C** 113: 13377-13385.
- Lamb, H. H. and Gates, B. C. (1986). Molecular organoosmium chemistry and catalysis on the basic magnesium oxide surface. **J. Am. Chem. Soc.** 108: 81-89.
- Laplaca, S. J., Hamilton, W. C., and Ibers, J. A. (1964). Crystal and molecular structure of manganese pentacarbonyl hydride. **Inorg. Chem.** 3: 1491-1495.

- Liang, A. J., Craciun, R., Chen, M., Kelly, T. G., Kletnieks, P. W., Haw, J. F., Dixon, D. A., and Gates, B. C. (2009). Zeolite-supported organorhodium fragments: essentially molecular surface chemistry elucidated with spectroscopy and theory. **J. Am. Chem. Soc.** 131: 8460-8473.
- Liddle, B. J., Wanniarachchi, S., Lindeman, S. V., and Gardinier, J. R. (2010). Tricarbonylrhenium (I) and manganese (I) complexes of 2-(pyrazolyl)-4-toluidine. **J. Organomet. Chem.** 695: 53-61.
- Lobo-Lapidus, R. J. and Gates, B. C. (2010). Supported rhenium complexes: almost uniform rhenium tricarbonyls synthesized from $\text{CH}_3\text{Re}(\text{CO})_5$ and HY zeolite. **Langmuir.** 26: 16368-16374.
- Mahmooda, Z., Azama, M., Mushtaq, A., Kausar, R., Kausar, S., and Gilani, SR. (2006). Comparative vapour phase FTIR spectra and vibrational assignment of manganese pentacarbonyls derivatives of the type $\text{XMn}(\text{CO})_5$: (where $\text{X}=\text{Br}, \text{Cl}, \text{I}, \text{H}, \text{D}, \text{CH}_3, \text{CD}_3, \text{CF}_3$). **Spectrochim. Acta. A-M.** 65: 445-452.
- Mariscal, R., Soria, J., Pena, M. A., and Fierro, J. L. G. (1994). Features of Li-Mn-MgO catalysts and their relevance in the oxidative coupling of methane. **J. Catal.** 147: 535-543.
- Morales, F., Grandjean, D., Mens, A., de Groot, F. M. F., and Weckhuysen, B. M. (2006). X-ray absorption spectroscopy of Mn/Co/TiO₂ Fischer-Tropsch catalysts: relationships between preparation method, molecular structure, and catalyst performance. **J. Phys. Chem. B** 110: 8626-8639.
- Muetterties, E. L. (1971). **Transition Metal Hydrides**. New York: M. Dekker.

- Papile, C. J. and Gates, B. C. (1992) Rhenium subcarbonyls on magnesium oxide: identification of the surface oxo and hydroxo ligands by infrared spectroscopy. **Langmuir** 8: 74-79.
- Papile, C. J., Knözinger, H., and Gates, B. C. (2000). $[\text{Re}_2(\text{CO})_9]_2^-$ on hydroxylated MgO: formation from $[\text{Re}_2(\text{CO})_{10}]$ and evidence of ion pairing at the surface. **Langmuir**. 16: 5661-5664.
- Parker, D. J. (1969). Infrared spectra of bis[tetracarbonyl(triphenoxyphosphine)-manganese]mercury and bis[tetracarbonyl(tributylphosphine)manganese]mercury. **J. Chem. Soc. A** 246-248.
- Pearson, W. B., Calvert, L. D., and Villars, P. (1985). **Pearson's Handbook of Crystallographic Data for Intermetallic Phases**. Metals Parks. Ohio: American Society for metals.
- Psaro, R. and Recchia, S. (1998). Supported metals derived from organometallics. **Catal. Today**. 41: 139-147.
- Purnell, S. K., Xu, X., Goodman, D. W., and Gates, B. C. (1994). Adsorption and reaction of $[\text{Re}_2(\text{CO})_{10}]$ on ultrathin MgO films grown on a Mo(110) surface: characterization by infrared reflection-absorption spectroscopy and temperature-programmed desorption. **J. Phys. Chem.** 98: 4076-4082.
- Ramallo-López, J. M., Ledesma, E. J., Requejo, F. G., Rodríguez, J. A., Kim, J. Y., Rosas-Salas, R., and Domínguez, J. M. (2004). XANES characterization of extremely nanosized metal-carbonyl subspecies (Me = Cr, Mn, Fe, and Co) confined into the mesopores of MCM-41 materials. **J. Phys. Chem. B** 108: 20005-20010.

- Ravel., B. and Newville, M. (2005). ATHENA, ARTEMIS, HEPHAESTUS: data analysis for X-ray absorption spectroscopy using IFEFFIT. **J. Synchrotron Radiat.** 12: 537-541.
- Rehr, J. J. and Albers, R. C. (2000). Theoretical approaches to X-ray absorption fine structure. **Rev. Mod. Phys.** 72: 621-654.
- Sayers, D. E., Stern, E. A., and Lytle, F. W. (1971). New technique for investigating nanocrystalline structures: fourier analysis of the extended X-ray absorption fine structure. **Phys. Rev. Lett.** 27: 1204-1207.
- Schneider, R. L., Howe, R. F., and Watters, K. L. (1984). Interactions of cobalt carbonyls with oxide surfaces. 3. Dicobalt octacarbonyl and tetracobalt dodecacarbonyl in zeolites. **Inorg. Chem.** 23(26): 4600-4607.
- Shriver, D. F., Atkins, P. W., and Langford, C. H. (1990). **Inorganic Chemistry.** Oxford: Oxford University Press.
- Stueben, B. L., Cantrelle, B., Sneddon, J., and Beck, J. N. (2004). Manganese K-edge XANES studies of Mn speciation in Lac des Allemands as a function of depth. **Microchem. J.** 76: 113-120.
- Tagliatesta, P., Giovannetti, D., Leoni, A., Neves, M. G. P. M. S., and Cavaleiro, J. A. S. (2006). Manganese(III) porphyrins as catalysts for the oxidation of aromatic substrates: An insight into the reaction mechanism and the role of the cocatalyst. **J. Mol. Catal. A-Chem.** 252: 96-102.
- Tai, Y., Yamaguchi, W., Tajiri, K., and Kageyama, H. (2009). Structures and CO oxidation activities of size-selected Au nanoparticles in mesoporous titania-coated silica aerogels. **Appl. Catal. A-Gen** 364: 143-149.

- Urbancic, M. A. and Shapley, J. R. (1989). Pentacarbonylhydridorhenium. **Inorg. Synth.** 26: 77-80.
- Uzun, A., Ortalan, V., Hao, Y., Browning, N. D., and Gates, B. C. (2009). Imaging gold atoms in site-isolated MgO-supported mononuclear gold complexes **J. Phys. Chem. C** 113(39): 16847-16849.
- Vaarkamp, M., Linders, J. C., and Koningsberger, D. C. (1995). A new method for parameterization of phase shift and backscattering amplitude. **Physica. B.** 209: 159-160.
- Yoneda, N., Kusano, S., Yasui, M., Pujado, P., and Wilcher, S. (2001). Recent advances in processes and catalysts for the production of acetic acid. **Appl. Catal. A-Gen** 221: 253-265.
- Youngs, C. T., Correa, F., Ploch, D., Burwell, R. L., and Shriver, Jr. D. F. (1983). Chemistry of the interaction of some metal carbonyl clusters with metal oxide surfaces. $[\text{CpFe}(\text{CO})]_4$, $\text{Cp}_3\text{Ni}_3(\text{CO})_2$, and $[\text{CpNi}(\text{CO})]_2$ on alumina. **Organometallics.** 2(7): 898-903.
- Zybill, C. E. (1997). **Synthetic methods of organometallic and inorganic chemistry.** New York: Georg Thieme Verlag.

CHAPTER VII

CONCLUSIONS

Dispersion of active metal on high surface area materials is an effective method to improve the performance of heterogeneous catalysts. In this thesis, zeolite NaY was synthesized and its transformation to NaP was investigated by variation of the synthesis conditions including aging and crystallization time. When the crystallization time was fixed at 1 day, the aging time of 1 day was suitable to produce the pure phase of zeolite NaY whereas 2 and 3 days aging times produced a small amount of NaP. The crystallization time showed a more significant effect on the transformation. The phase of NaY was not observed after crystallization for 4 days and NaP was the major product after 5 days crystallization,.

The zeolite NaY was used as a support for bimetallic catalysts containing palladium and cobalt (1Pd7Co/NaY) in *n*-butane hydrogenolysis. Its activity was compared to that of bimetallic catalysts supported on zeolite ZSM-5 (1Pd7Co/ZSM-5). Reducibility of cobalt species supported on zeolite ZSM-5 after reduction, determined by XANES spectroscopy was higher than that supported on zeolite NaY. The results from catalytic testing on *n*-butane hydrogenolysis showed that activity over 7Co1Pd/ZSM-5 was higher than that over 1Pd7Co/NaY. Thus, the activity of cobalt catalysts with ZSM-5 as a support was further investigated. In monometallic cobalt catalysts (1, 4, and 7Co/ZSM-5), except 10Co/ZSM-5, the reducibility of cobalt and the conversion of *n*-butane hydrogenolysis increased with cobalt content.

The activity of 10Co/ZSM-5 was lower than 7Co ZSM-5 despite the higher degree of reduction because of the difference in surface active sites on both catalysts, namely, the 10Co/ZSM-5 had a poorer cobalt dispersion. Methane was the only product observed over the monometallic cobalt catalysts because cobalt favored multiple hydrogenolysis reaction.

Addition of 1 wt%Pd to cobalt catalysts promoted the reducibility only in 1Co/ZSM-5 whereas enhancement in the reducibility or catalytic activity were not significant on the catalysts with the higher cobalt loading. Besides methane, trace amount of ethane and propane was observed in the reaction over bimetallic catalysts suggesting that Pd inhibited the multiple hydrogenolysis.

A highly uniform manganese supported on high area MgO was prepared by chemical vapor deposition of manganese carbonyl complexes including $\text{Mn}_2(\text{CO})_{10}$, $\text{Mn}(\text{CO})_5\text{H}$ and $\text{Mn}(\text{CO})_5\text{CH}_3$. The reaction of $\text{Mn}_2(\text{CO})_{10}$ and MgO took place at -OH groups of MgO. IR spectroscopy characterizing the supported samples indicated that the sample with 3.0 wt% Mn contained physisorbed $\text{Mn}_2(\text{CO})_{10}$ as a dominant surface species whereas surface species of sample with 1.0 wt% Mn consisted of a mixture of physisorbed $\text{Mn}_2(\text{CO})_{10}$, manganese pentacarbonyl and manganese tricarbonyl. Treatment of sample prepared from 1.0 wt% Mn on MgO in O_2 at room temperature resulted in a more uniform surface. EXAFS characterizing this sample showed that Mn-Mn bond in $\text{Mn}_2(\text{CO})_{10}$ was cleaved and each manganese atom bonded to three oxygen atoms of MgO and three carbonyl ligands. EPR and XANES spectroscopy indicated that the oxidation state of manganese in the O_2 treated sample was greater than +2.

The adsorption of $\text{Mn}(\text{CO})_5\text{H}$ occurred on $-\text{OH}$ groups of MgO . The IR spectroscopy characterizing sample prepared from $\text{Mn}(\text{CO})_5\text{D}$ and MgO suggested that the adsorption also involved the donation of deuteron to surface oxygen of MgO . Reaction between $\text{Mn}(\text{CO})_5\text{H}$ and MgO produced surface species including manganese tricarbonyl and manganese pentacarbonyl. Treatment of this sample in O_2 at room temperature resulted in a sample with only manganese tricarbonyl as surface species. XAS characterization of this sample indicated that each manganese atom bonded to three oxygen atom of MgO and three carbonyl ligands. EPR and XANES spectroscopy indicated that the oxidation state of manganese in this sample was +3.

The adsorption of $\text{Mn}(\text{CO})_5\text{CH}_3$ on MgO involved reaction of $\text{Mn}(\text{CO})_5\text{CH}_3$ and OH group as well as the removal of CO and CH_3 in precursor. The adsorption led to the formation of only one surface species, manganese tetracarbonyl with manganese in +3 oxidation state. O_2 treatment of the sample prepared from $\text{Mn}(\text{CO})_5\text{CH}_3$ on MgO did not change either the manganese oxidation state or the number of carbonyl ligands on the manganese.

Recommendation for further work

The dispersion of cobalt oxide in mono- and bimetallic catalysts containing cobalt before and after reduction could be determined by using TEM, EXAFS or other techniques. The surface species could be suggested by EXAFS.



APPENDIX A

EXAFS FITTING CHARACTERIZING $\text{Mn}_2(\text{CO})_{10}$

SUPPORTED ON MgO CONTAINING 1.0 wt% Mn

AFTER O_2 TREATMENT

Table A1 EXAFS parameters characterizing sample prepared from $\text{Mn}_2(\text{CO})_{10}$ supported on MgO containing 1.0 wt% Mn after O_2 treatment for model including an Mn–Mg contribution^a.

Absorber–backscatterer pair	N	R (Å)	$\Delta\sigma^2 \times 10^{-3}$ (Å ⁻²)	ΔE_0 (eV)	(χ^2)
Mn–C	2.78	1.93	8.7	7.3	260
Mn–O*	2.48	3.28	12.6	7.3	
Mn–O _s	0.86	2.04	9.4	2.3	
Mn–Mg	0.59	3.56	0.2	-1.6	

^aNotation: N , coordination number; R , distance between absorber and backscatterer atoms; $\Delta\sigma^2$, sigma-squared value (disorder term); ΔE_0 , inner potential correction; O*, oxygen of carbonyl group; O_s, oxygen atom of MgO. Typical errors: N , $\pm 20\%$; R , ± 0.04 Å; $\Delta\sigma^2$, $\pm 20\%$; ΔE_0 , $\pm 20\%$.

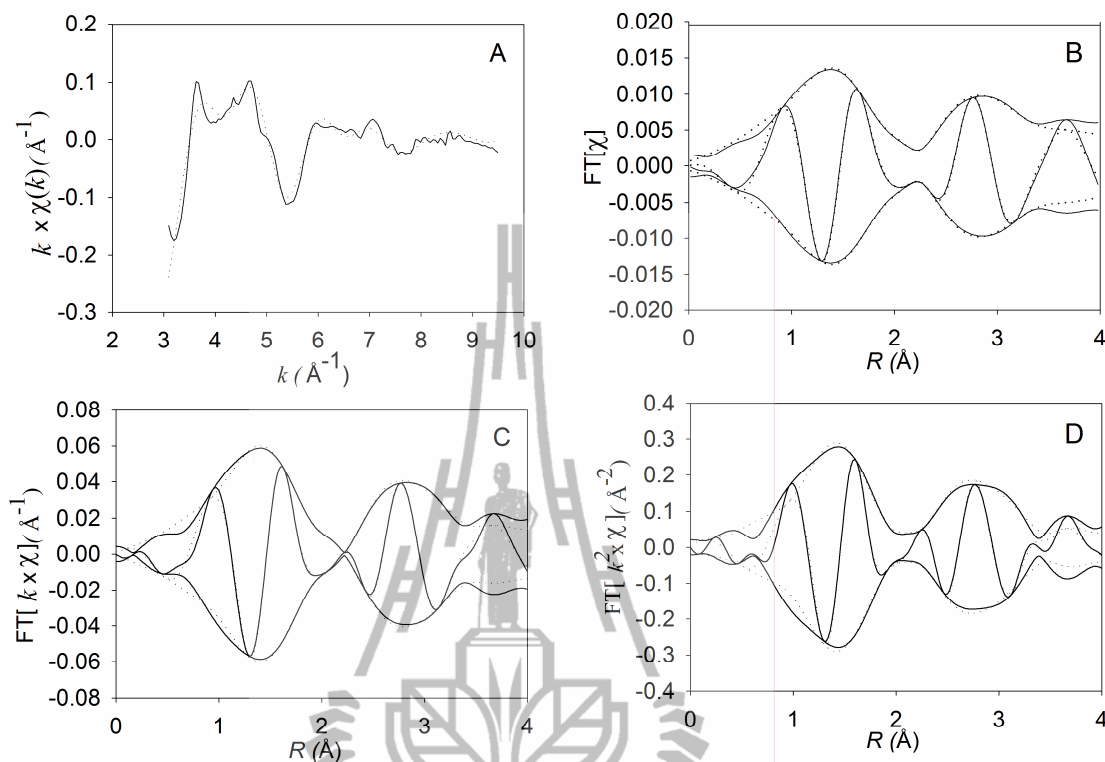


Figure A1 EXAFS data and corresponding FT magnitudes and imaginary parts characterizing the sample prepared from $\text{Mn}_2(\text{CO})_{10}$ supported on MgO containing 1.0 wt% Mn after O_2 treatment for a model including a Mn–Mg contribution : k -weighted EXAFS function in k -space (A); imaginary part and magnitude of EXAFS function in R -space with FT k^0 -weighting (B), FT k^1 -weighting (C), and FT k^2 -weighting (D).

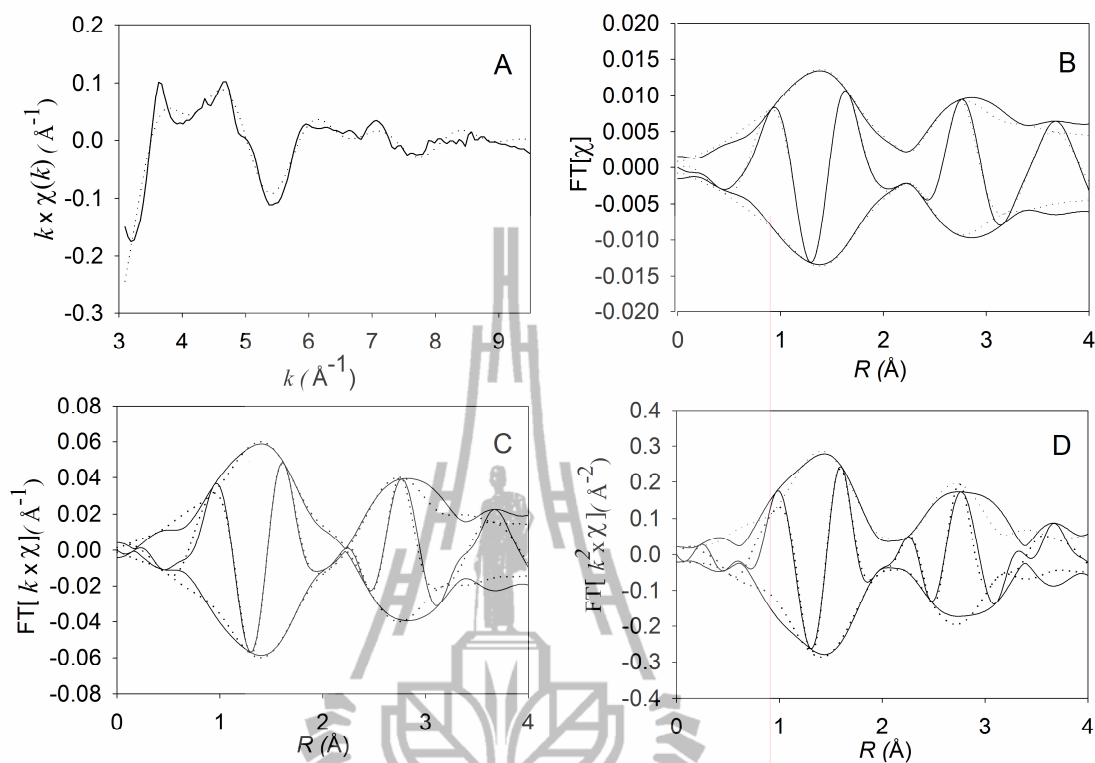


Figure A2 EXAFS data and corresponding FT magnitudes and imaginary parts characterizing the sample prepared from $\text{Mn}_2(\text{CO})_{10}$ supported on MgO containing 1.0 wt% Mn after O_2 treatment for model 1: contribution : k -weighted EXAFS function in k -space (A); imaginary part and magnitude of EXAFS function in R -space with FT k^0 -weighting (B), FT k^1 -weighting (C), and FT k^2 - weighting (D).

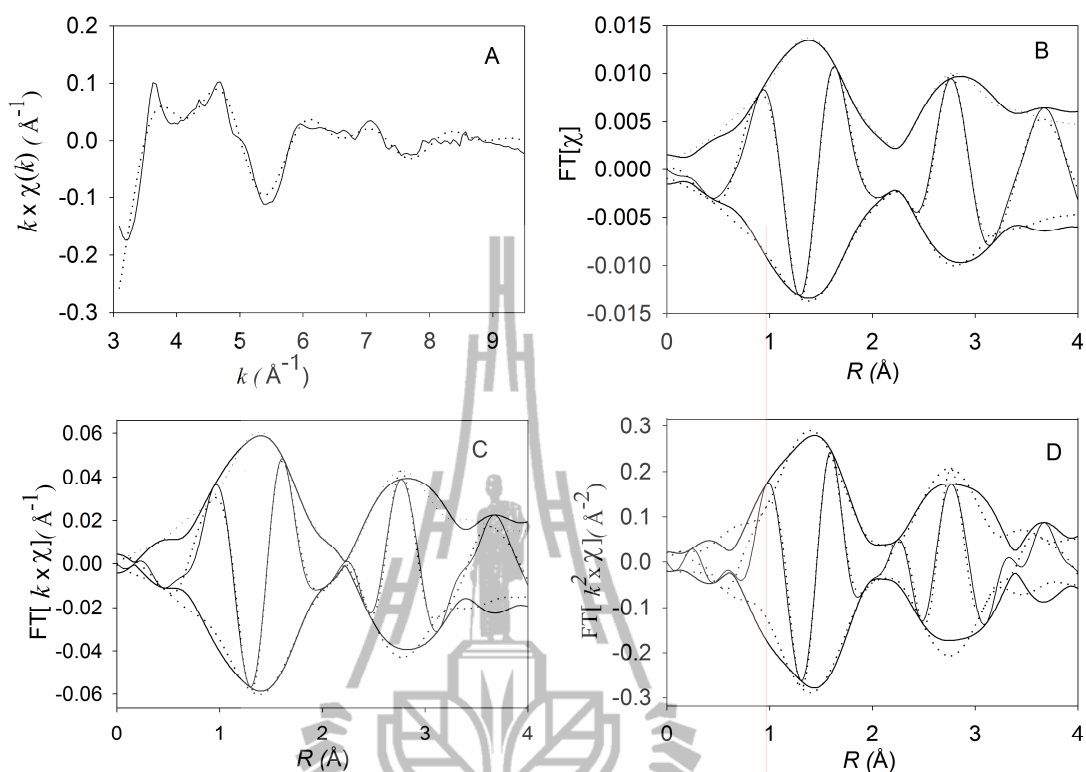


Figure A3 EXAFS data and corresponding FT magnitudes and imaginary parts characterizing the sample prepared from $\text{Mn}_2(\text{CO})_{10}$ supported on MgO containing 1.0 wt% Mn after O_2 treatment for model 2: contribution : k -weighted EXAFS function in k -space (A); imaginary part and magnitude of EXAFS function in R -space with FT k^0 -weighting (B), FT k^1 -weighting (C), and FT k^2 -weighting (D).



APPENDIX B

EXAFS FITTING CHARACTERIZING $\text{Mn}(\text{CO})_5\text{H}$ AND

$\text{Mn}(\text{CO})_5\text{CH}_3$ ON PARTIALLY

DEHYDROXYLATED MgO

Table B1 EXAFS parameters characterizing sample prepared from $\text{Mn}(\text{CO})_5\text{H}$ on MgO after O_2 treatment $\text{Mn}_2(\text{CO})_{10}$ for model No. 2^a.

Absorber–backscatterer pair	N	R (Å)	$\Delta\sigma^2$ (Å ⁻²)	ΔE_0 (eV)
Mn–C	2.90	1.984	0.01107	6.92
Mn–O*	2.84	3.299	0.01450	6.92
Mn–O _s	0.62	2.236	0.00767	-10.42
Mn–Mg	0.36	3.588	0.00025	-8.88

^aNotation: N , coordination number; R , distance between absorber and backscatterer atoms; $\Delta\sigma^2$, sigma-squared value (disorder term); ΔE_0 , inner potential correction; O*, oxygen of carbonyl group; O_s, oxygen atom of MgO. Typical errors: N , $\pm 20\%$; R , ± 0.04 Å; $\Delta\sigma^2$, $\pm 20\%$; ΔE_0 , $\pm 20\%$.

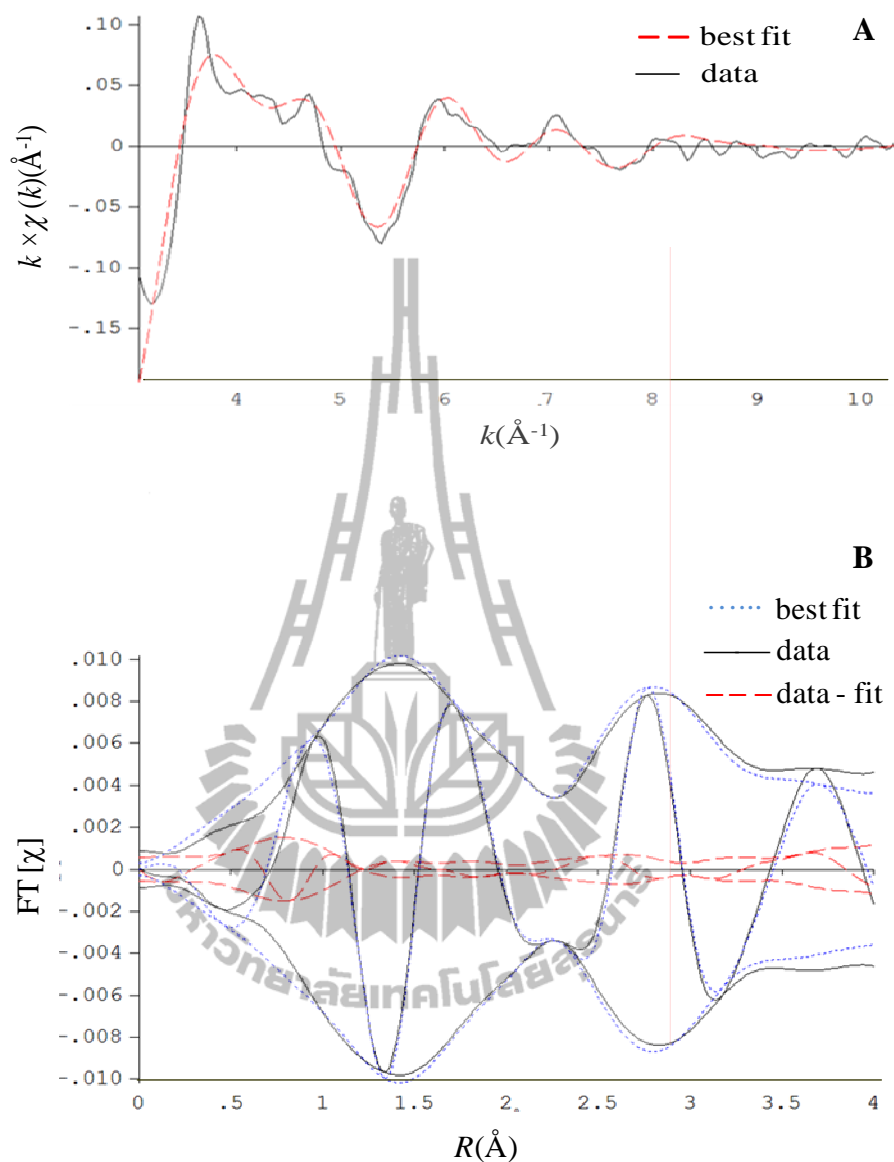


Figure B1 EXAFS data characterizing sample prepared from $\text{Mn}(\text{CO})_5\text{H}$ on MgO after O_2 treatment for model No. 3. (A) k -weighted EXAFS function in k -space, (B) imaginary part and magnitude of EXAFS function in R -space with FT k^0 -weighting.

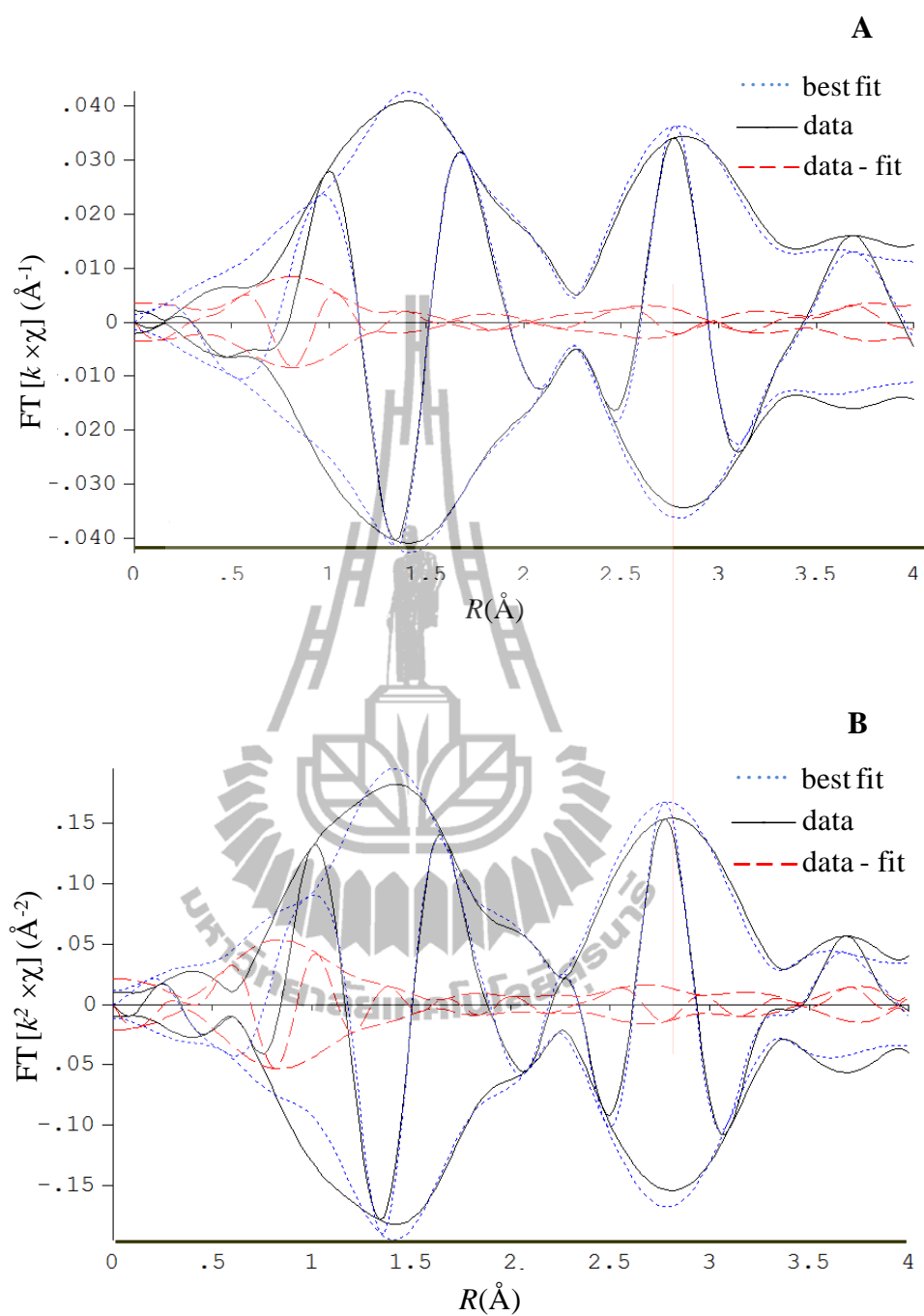


Figure B2 EXAFS data characterizing sample prepared from $\text{Mn}(\text{CO})_5\text{H}$ on MgO after O_2 treatment for model No. 3 in imaginary part and magnitude of EXAFS function in R -space with FT (A) k^1 -weighting and (B) k^2 -weighting.

Table B2 EXAFS parameters characterizing sample prepared from $\text{Mn}(\text{CO})_5\text{H}$ on MgO after O_2 treatment $\text{Mn}_2(\text{CO})_{10}$ for model No. 3^a.

Absorber–backscatterer pair	N	R (Å)	$\Delta\sigma^2$ (Å ⁻²)	ΔE_0 (eV)
Mn–C	2.41	1.981	0.01211	7.05
Mn–O*	2.30	3.294	0.01472	7.05
Mn–O _s	0.75	2.216	0.01401	-9.54

^aNotation: N , coordination number; R , distance between absorber and backscatterer atoms; $\Delta\sigma^2$, sigma-squared value (disorder term); ΔE_0 , inner potential correction; O*, oxygen of carbonyl group; O_s, oxygen atom of MgO. Typical errors: N , $\pm 20\%$; R , ± 0.04 Å; $\Delta\sigma^2$, $\pm 20\%$; ΔE_0 , $\pm 20\%$.

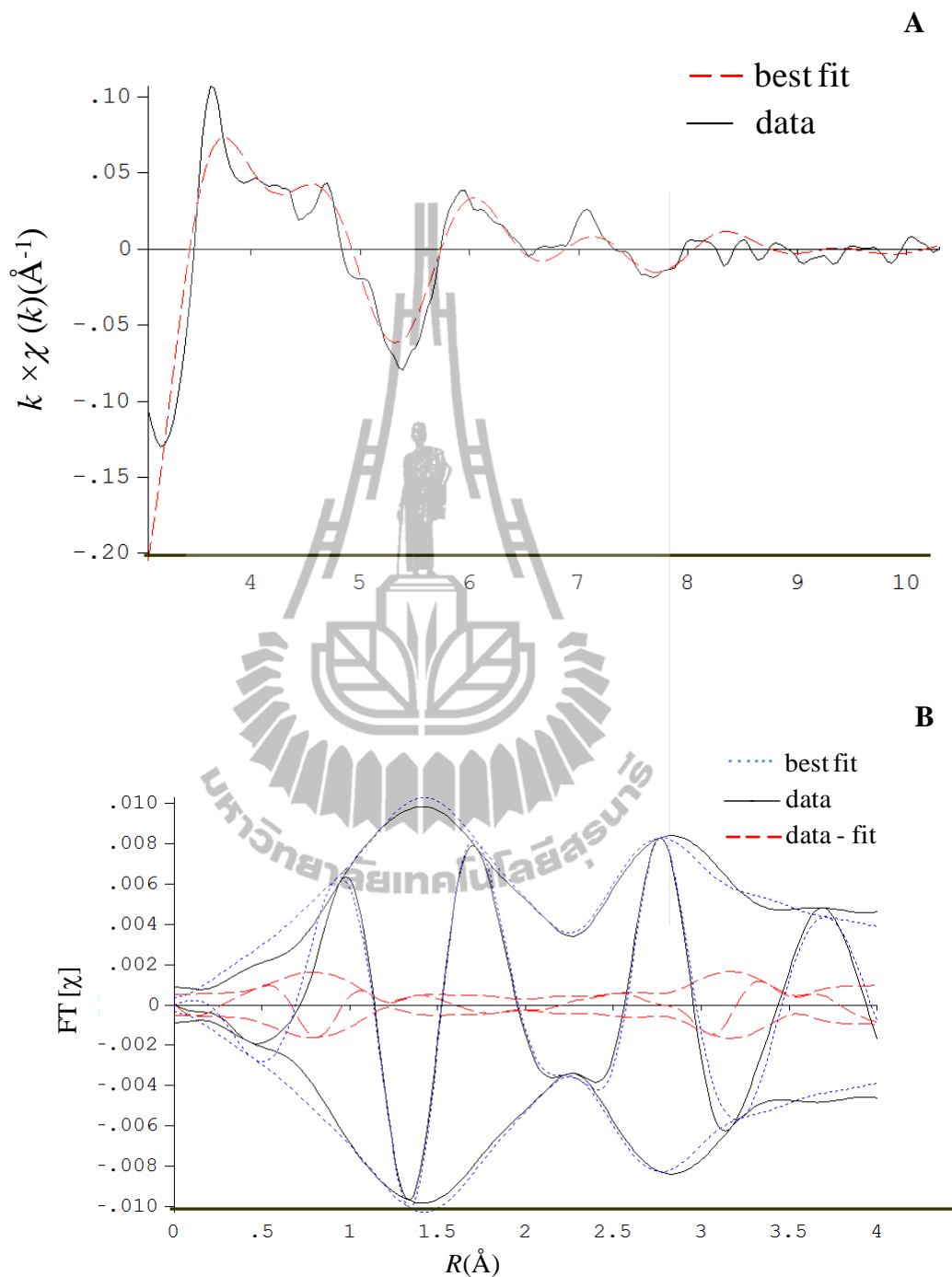


Figure B3 EXAFS data characterizing sample prepared from $\text{Mn}(\text{CO})_5\text{H}$ on MgO after O_2 treatment for model No. 3. (A) k -weighted EXAFS function in k -space, (B) imaginary part and magnitude of EXAFS function in R -space with FT k^0 -weighting.

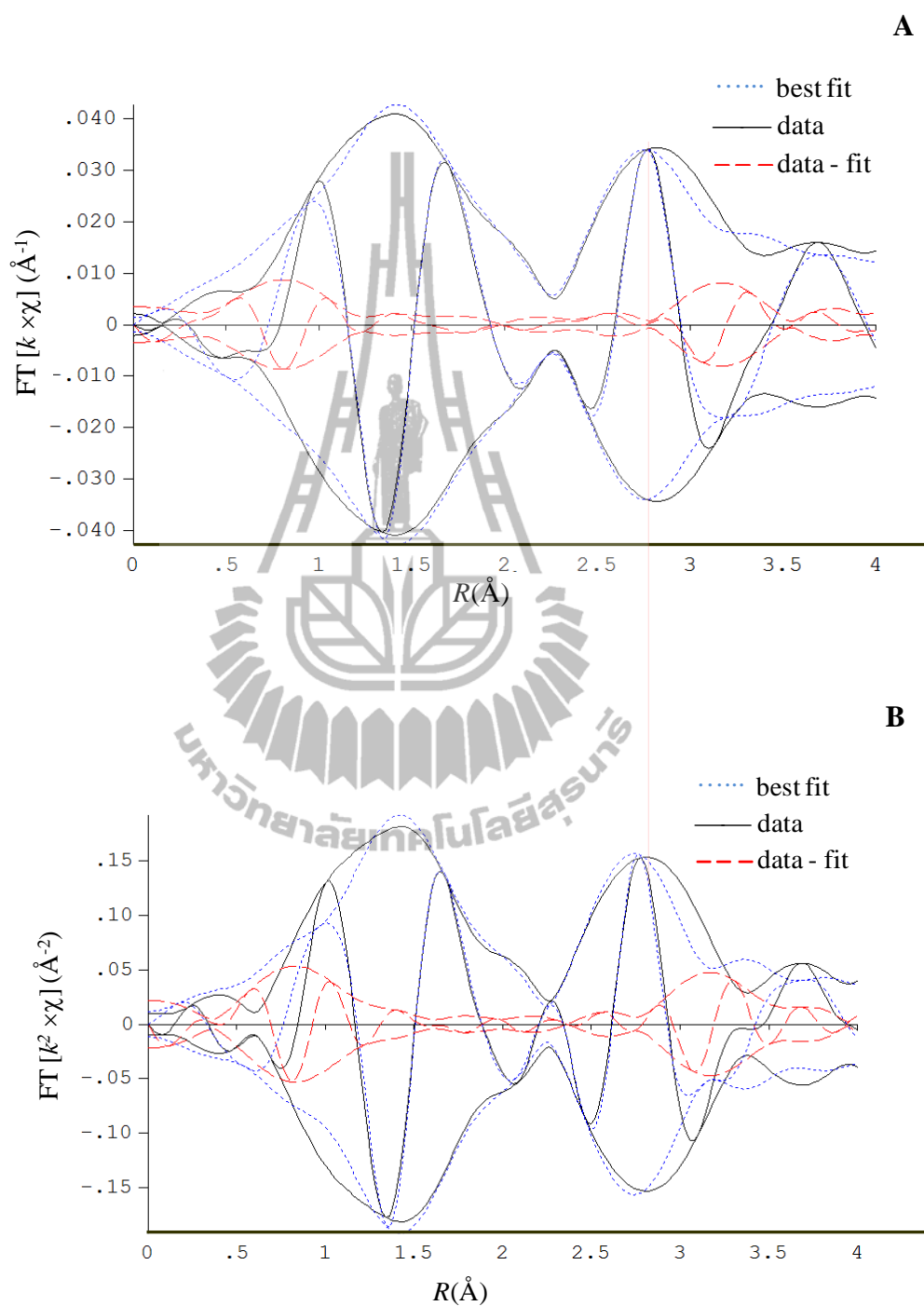
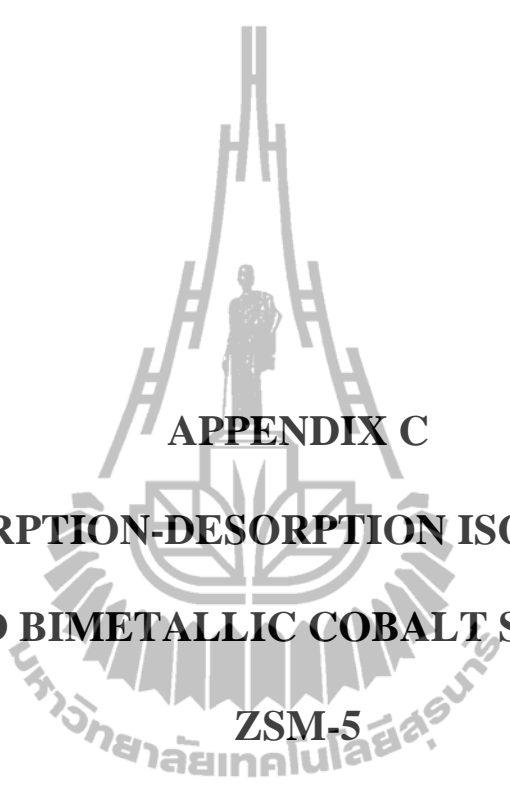


Figure B4 EXAFS data characterizing sample prepared from $\text{Mn}(\text{CO})_5\text{H}$ on MgO after O_2 treatment for model No. 3 in imaginary part and magnitude of EXAFS function in R -space with FT (A) k^1 -weighting and (B) k^2 -weighting.



APPENDIX C

**N₂ ADSORPTION-DESORPTION ISOTHERMS OF
MONO-AND BIMETALLIC COBALT SUPPORTED ON
ZSM-5**

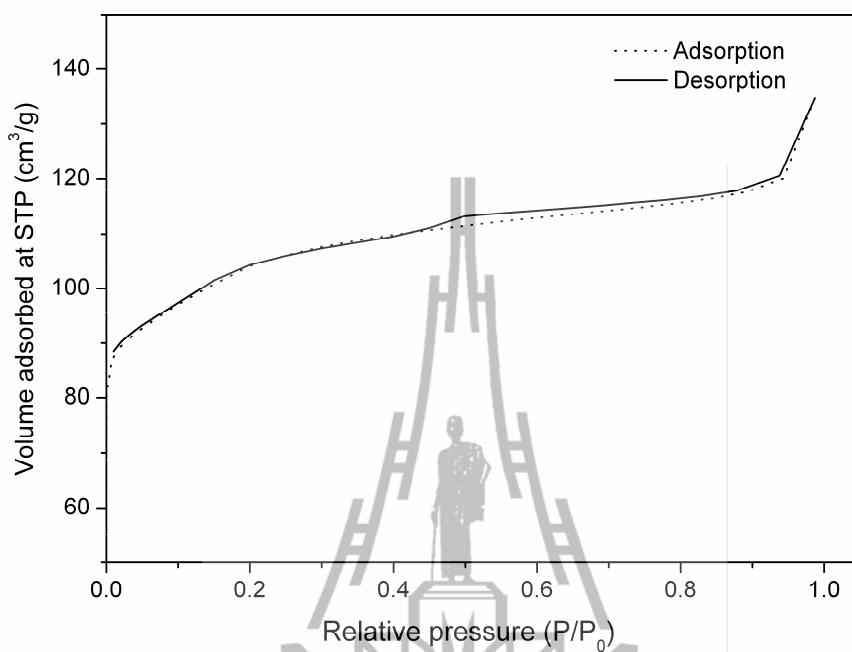


Figure C1 N₂ adsorption-desorption isotherm of 1Co/ZSM-5.

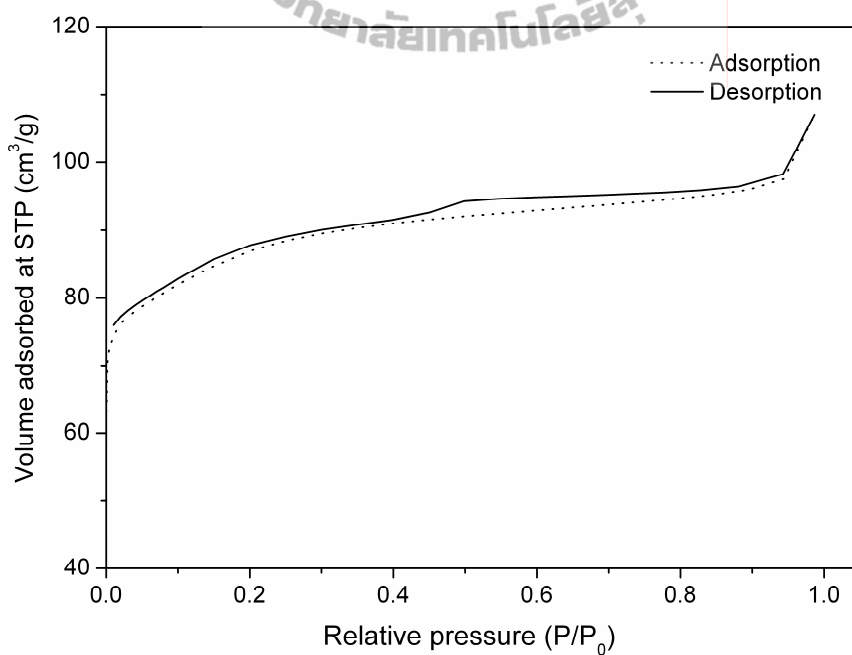


Figure C2 N₂ adsorption-desorption isotherm of 4Co/ZSM-5.

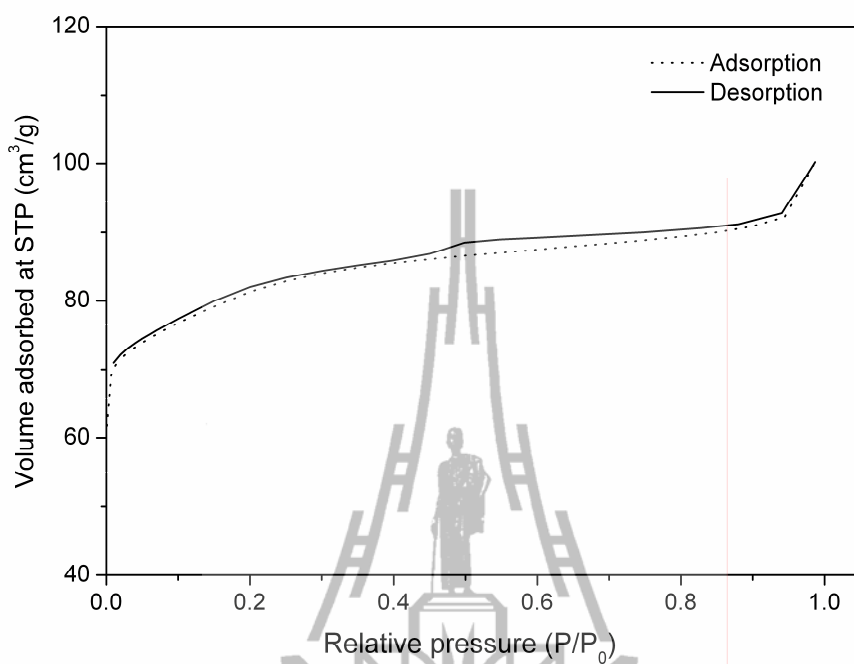


Figure C3 N₂ adsorption-desorption isotherm of 7Co/ZSM-5.

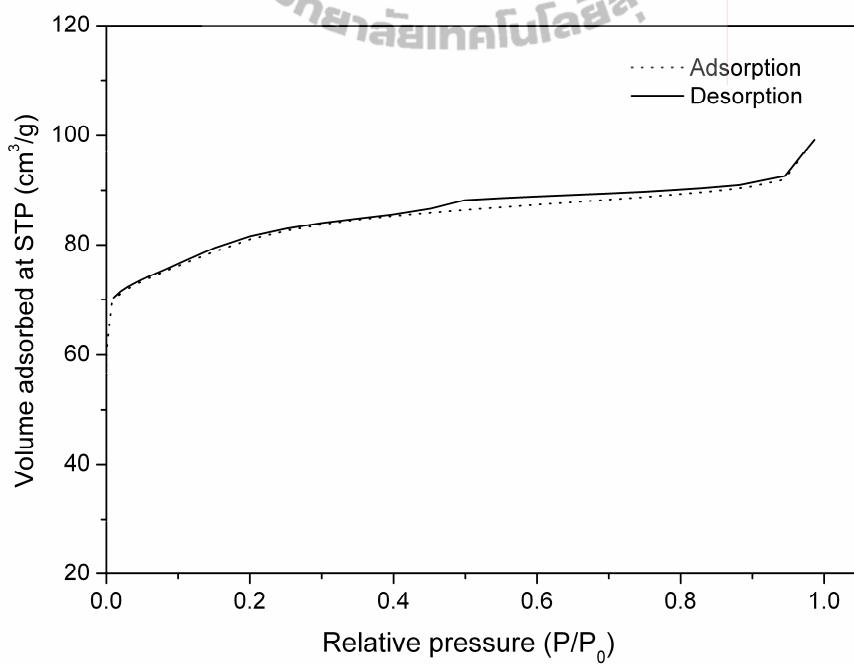


Figure C4 N₂ adsorption-desorption isotherm of 10Co/ZSM-5.

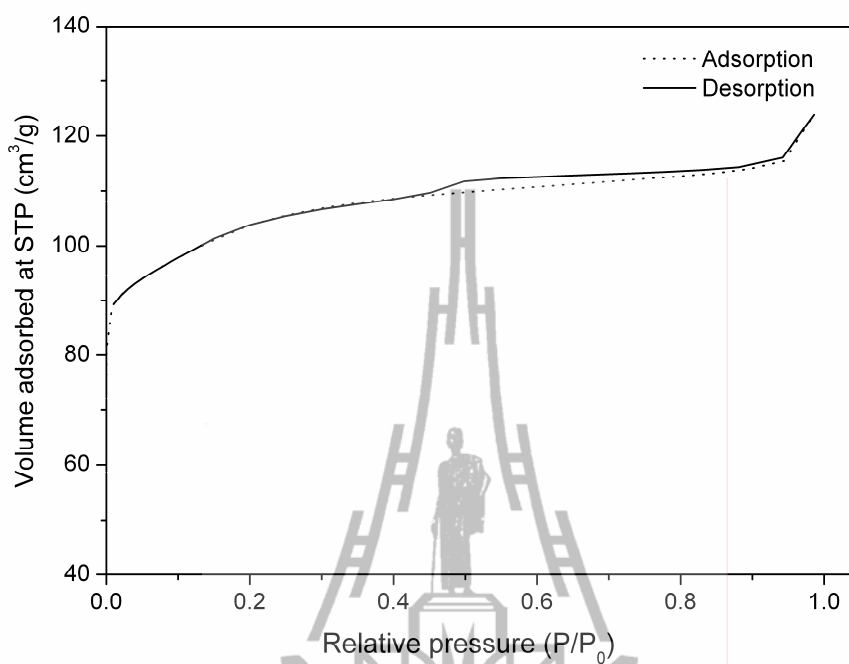


Figure C5 N₂ adsorption-desorption isotherm of 1Co1Pd/ZSM-5.

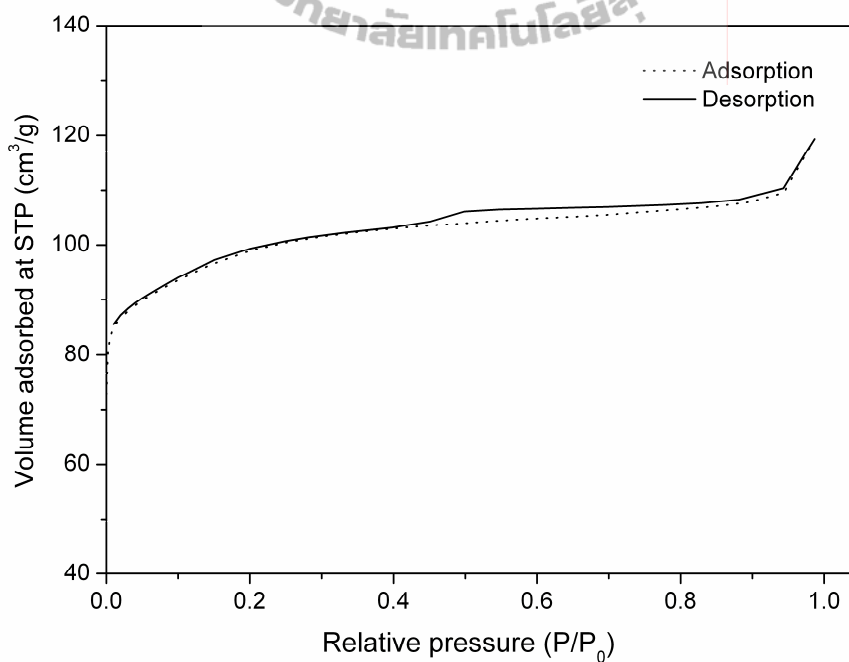


Figure C6 N₂ adsorption-desorption isotherm of 4Co1Pd/ZSM-5.

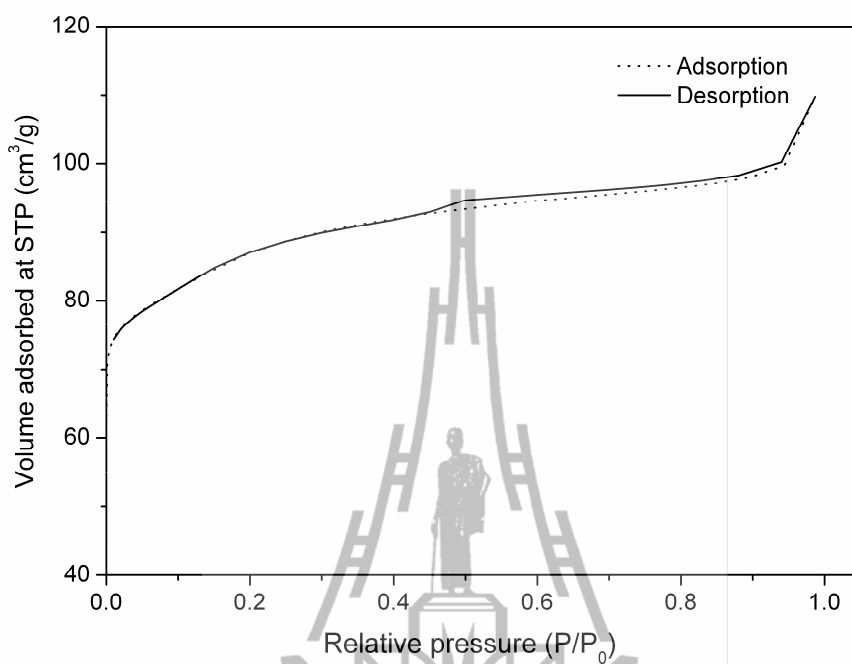


Figure C7 N₂ adsorption-desorption isotherm of 10Co/ZSM-5.

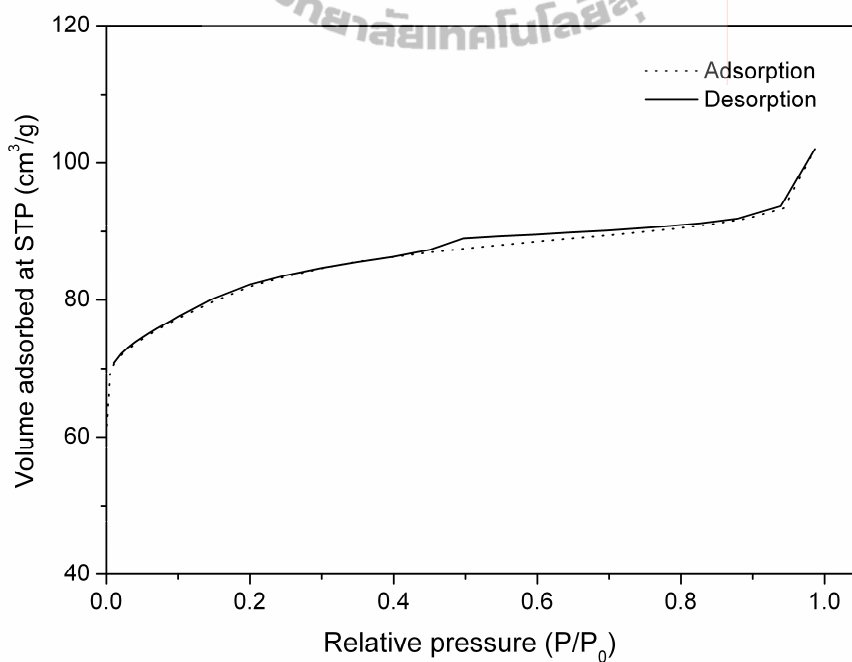


Figure C8 N₂ adsorption-desorption isotherm of 10Co1Pd/ZSM-5.

CURRICULUM VITAE

Name Miss Supattra Khabuanchalad

Education

- 2001-2005 B.Sc. Chemistry (First class honor), Ubon Ratchathani University, Thailand
- 2005-2006 Grad. Dip. (Teaching Profession), Silpakorn University, Thailand
- 2006-2011 Ph.D. (Chemistry) Suranaree University of Technology, Thailand
under a sandwich program with University of California, Davis, USA

Publications and Presentations

- Khabuanchalad, S., Khemthong, P., Prayoonpokarach, S. and Wittayakun, J. (2008). **Suranaree J. Sci. Technol.** 15(3): 225-231.
- Khabuanchalad, S., Wittayakun, J., Lobo-Lapidus, R. J., Stoll, S., Britt, R. D. and Gates, B. C. (2010). **J. Phys. Chem. C** 114: 17212-17221.
- Khabuanchalad, S., Khemthong, P., Prayoonpokarach, S. and Wittayakun, J. (2007). Oral Presentation in the 14th Regional Symposium on Chemical Engineering (RSCE 2007), December 4-5, 2007, Yogyakarta, Indonesia.
- Khabuanchalad, S., Lobo-Lapidus, R. J., Wittayakun, J. and Gates, B. C. (2010). Oral Presentation in 239th ACS National Meeting, March 21-25, 2010, San Francisco, California.
- Wittayakun, J., Khabuanchalad, S., Lobo-Lapidus, R. J., Stoll, S., Britt, R. D. and Gates, B. C. (2011). Oral Presentation (Invited) in 14th Asian Chemical Congress, September 5-8, 2011, Bangkok, Thailand.